Numerical simulation of two-dimensional vortex shedding for marine applications

Thesis Submitted for Doctor of Philosophy

By G., Xu

Department of Mechanical Engineering

University College London

Torrington Place, London WC1E 7JE, UK

To my parents

Declaration

I, Guodong Xu, confirm that the work presented in this thesis is my own. Where information has been derived from other sources, I confirm that this has been indicated in the thesis.

Sign……

Date……...

Acknowledgement

First and foremost I would like to thank my principal supervisor professor G.X. Wu for his contributions in my three years' study. He is positive to share the knowledge, idea and the method to find a solution; therefore make my research productive. He always encourages me to deliver new ideas. In my writing up stage, he made a lot of insightful comments and proposed many challenging questions, which helped me to present logically and accurately. He encourages me to pursue independent research work. Apart from the academic support, his enthusiasm and motivation inspire me in the pursuit of excellence. In the everyday life, Professor Wu helps me to overcome the difficulties in a foreign country. To me, he is a teacher, brother and friend.

I own my gratitude to my secondary supervisor professor Paul Wrobel. In addition to his humour, I have seen a positive and sunny attitude towards life. I would like to thank his encouragement and helpful suggestions throughout my research and writing of the thesis. He has been a supportive supervisor, both academically and financially.

My sincere thanks also go to Dr William Suen for his supportive guidance and helpful suggestions. Other members of staff, including Dr Kevin Drake, Ms Ema Muk-Pavic deserve my sincerest thanks. Their constructive suggestions help me to get a clear map to complete the research.

Special thanks to the sponsor Lloyd's Register EMEA. Their financial support and less demanding requirements make a relaxed circumstance for my research, which are most valuable.

I would also express my appreciation of my colleagues Daniel Fone, Anne Charlotte. We work as a team quite well and have extensive discussions on the project. Daniel provided the experimental data. My gratitude goes to Dr. Peter Johnson and Tim McDonald as well. They shared many references and we had discussed many times on the vortex shedding.

Special thanks go to Professor Mohan Edirisinghe and Dr. C K Tam. The badminton time with you refresh me when I feel tired of programming. Other friends in and out of our department are the sources of laughter, joy. Happy times with Dr. Hang Xu, Miss Jianjian Dong, Dr. Baoyu Ni, Professor Aman Zhang, Professor ZiMin Kou, Ms Yajie Li and Bingyue Song, Mr Peng Wang, Zeeshan Riaz, Weheliye, Al-Omar Omar, P. Boselli, Chongwei Zhang and Qicheng Meng have meant more to me than I could express.

Thanks to my parents, Mr Changfu Xu and Mrs Ruihong Wu for their unconditional support. Their love is my driving force. I hope you will be proud of me.

Abstract

The velocity potential theory has been adopted to describe the inviscid flow around the marine structures. The two-dimensional vortex shedding problems in marine hydrodynamics such as a hydrofoil advancing near the free surface, the flow passing through an orifice of a damaged compartment are studied in the present work.

As the steady motion and small amplitude unsteady motion of a hydrofoil advancing near free surface is considered, a flat vortex sheet is introduced and imposed behind the trailing edge. Free surface Green functions, which satisfy the free surface boundary conditions, are adopted to account for the free surface effects. The effects of wave radiation and diffraction are investigated.

To study the nonlinear effect of vortex wake and body surface boundary condition of a foil with thickness or a plate structure, we introduce a time stepping scheme to simulate the continuous vortex shedding. The functional motion modes of a foil or plate, including propulsion, energy harvesting and flying, have been simulated. The damping effect of vortices on the heave motion of a compartment with bottom opening in unbounded flow is analysed.

The free surface effect on the steady and unsteady motions on a foil is further studied through the time stepping methodology. The force history at different forward speeds and submergences is investigated and discussed. The simulations on the free surface effect on the propulsion, energy harvesting and flying modes are carried out.

Further efforts are made to investigate the forced heave motion of a flooded floating compartment. The non-linear free surface and non-linear vortex wake are tracked in the framework of Lagrangian. The ingress and egress fluid flow together with vortices and their effect on the hydrodynamic force are investigated.

Symbols and nomenclature

Greek characters, lower case

$\alpha(t) = \arctan\dfrac{\dot{h}(t)}{U(t)} - \theta(t) + \beta$ effective attack angle at the rotational centre

$\alpha_0 = \arctan\dfrac{\omega h_0}{U} - \theta_0 = \arctan(\pi St) - \theta_0$ nominal maximum effective attack angle

β mean attack angle

ε phase difference of the rotational motion to vertical motion

ε_w phase difference of the wave to the oscillatory centre ($x = 0, t = 0$)

ϕ perturbed velocity potential

$\bar{\phi}$ velocity potential due to steady motion

$\tilde{\phi}_p$ perturbed velocity potential due to wave radiation and diffraction

ϕ_+, ϕ_- the potential on the upper and lower surface of plate

ϕ_{w+}, ϕ_{w-} the potential on the upper and lower surface of vortex wake

$\varphi_0, \varphi_1, \varphi_3, \varphi_5, \varphi_7$ velocity potential due to incident wave, surge, heave, pitch motions and diffraction waves respectively

γ strength of the vortex wake

$\eta_T = \dfrac{c_T}{c_p^{in}}$ propulsive efficiency

$\eta_E = \dfrac{P}{\rho U^3 h_0}$ power efficiency of energy harvesting mode

$\kappa = g / U^2$ the wave number due to steady motion

λ_w surface wave length

λ_1, λ_2 parameters to set the time step

$\mu = \phi_{w+} - \phi_{w-}$ strength of vortex dipole

$\nu = \omega^2 / g$

π ratio of the circumference

$\theta(t) = \theta_0 \sin(\omega t + \varepsilon)$ rotational displacement of the foil, the positive direction is defined as counter clockwise

ρ density of the fluid

ω circular frequency of vertical and rotational motions

ω_0 circular frequency of the incident wave

$\tau = U\omega / g$

$\varsigma(x,t)$ free surface

Greek characters, upper case

ψ the angle for circular column to $z = 0$

ψ_{start}, ψ_{end} the angles of the starting and ending position to $z = 0$

$\psi_0 = \psi_{end} - \psi_{start}$

Φ total velocity potential

Γ strength of the point vortex

Latin characters, lower case

$a_1, a_2, a_3, a_4, b_0, b_1, b_2, b_3, b_4$ the coefficients of decomposed force of frequencies $n\omega$

$c(x)$, c_a, c_b the parameter of damping zone

$c_p = \frac{2p}{\rho U^2}$ pressure coefficient

$c_R = \frac{2F_{s1}}{\rho U^2 C}$, $c_L = \frac{2F_{s3}}{\rho U^2 C}$, $c_M = \frac{4F_{s5}}{\rho U^2 C^2}$ the resistance coefficient, lifting coefficient, moment coefficient

$c_T = \frac{F_T}{0.5\rho C U^2}$; $c_L = \frac{F_L}{0.5\rho C U^2}$ thrust and lift coefficients

$c_{PL} = \frac{P_L}{0.5\rho C U^3}$; $c_{PM} = \frac{P_M}{0.5\rho C U^3}$; $c_P^{in} = \frac{P}{0.5\rho C U^3}$ power coefficients

$c_{PL}^{in} = -c_{PL}$, $c_{PM}^{in} = -c_{PM}$, $c_P^{in} = -c_{PO}$

$c_D = -c_T$ drag coefficient

d size of the orifice

dt_0 basic time step

dt_w basic time step based on the wake velocity

f frequency of the motion

$f_1 = \frac{2F_1}{\rho C U^2}$, $f_3 = \frac{2F_3}{\rho C U^2}$, $f_5 = \frac{4F_5}{\rho C^2 U^2}$ the non-dimensional force for the time stepping simulation

$f_{element}$ parameter to control the element size on the free surface

$f_{u1j} = \frac{2F_{u1j}}{\rho g C}$, $f_{u3j} = \frac{2F_{u3j}}{\rho g C}$, $f_{u5j} = \frac{4F_{u5j}}{\rho g C^2}$ non-dimensionalized unsteady force amplitude of a foil

g acceleration due to gravity

$h(t) = h_0 \sin \omega t$ vertical displacement of the foil

h_T the submergence from the trailing edge to still water line

h_C the submergence from mean rotational center to still water line

k_0 incident wave number

k_1, k_2, k_3, k_4 wave number due to wave radiation

l half chord length

l_c length of the rotational centre (x_c, z_c) to leading edge

l_0 basic element size

m_1, m_3, m_5 the m_j terms

$\vec{n} = (n_1, n_3, n_5) = (n_x, n_z, -Xn_z + Zn_x)$ normal vector

$p_{re} = p - p_a$ hydrodynamic pressure, p_a is the ambient pressure

q_e non-dimensional flow rate of ingress/egress flow

$\vec{s} = (s_x, s_z)$ tangential vector

$s_{element}$ parameter to control size of element on free surface

t time scale

t_{ck} thickness of the foil

t_i the existing time of the point vortex

t_{start}, t_{end} the time when the damping of point vortex starts and ends respectively.

(x_c, z_c) the rotation centre

$\vec{x}_T(x_T, z_T)$ position of the trailing edge

$\vec{x}_{T'}(x_{T'}, z_{T'})$ position of the end point of first vortex dipole element

$(\hat{x}, \hat{z}) = (x, z)/C$ non-dimensional coordinates system for a foil

Latin characters, upper case

$A = 2h_0$

$\vec{A}_T = (A_1, A_2, A_3)$, $\vec{A}_R = (A_4, A_5, A_6)$ are the translational and rotational displacements

B breadth of the compartment

C chord of the foil and $C = 2l$

$F_1(t), F_3(t), F_5(t)$ transient horizontal, vertical force and moment

$Fn = \dfrac{U}{\sqrt{gC}}$ Froude number

$F_L = \dfrac{1}{T}\int_t^{t+T} F_3(t)dt$ time-averaged lifting force

$F_T = \dfrac{1}{T}\int_t^{t+T} F_1(t)dt$ time-averaged thrust

$F_{u_{ji}}$ amplitude of complex wave radiation force

F_{w_j} amplitude of complex wave force due to incident wave and wave diffraction

$G(p,q)$ $H(p,q)$ Green's function

$P = P_L + P_M$ total power due to vertical and rotational motions

$P_L = \dfrac{1}{T}\int_t^{t+T} F_3(\tau)\dot{h}(\tau)d\tau$ the power due to vertical motion

$P_M = \dfrac{1}{T}\int_t^{t+T} F_5(\tau)\dot{\theta}(\tau)d\tau$ the power due to rotational motion

R_1 radius of inner surface of the circular column

$\tilde{R}_1$ modified radius of inner surface of the circular column

R_2 radius of outer surface of the circular column

$\tilde{R}_2$ radius of outer surface of the circular column

$St = \frac{\omega h_0}{\pi U}$ Strouhal number

S_{wall} length of the vertical side wall of the compartment

$T = 2\pi / \omega$ period of the oscillation

U speed of the body or the incoming flow

$U_{S_T} = (-U + \bar{u}_{\bar{x}_T}, \bar{w}_{\bar{x}_T})$ average velocity at the trailing edge

$U_{S_0} = (U + \dot{\theta}Z, \dot{h} - \dot{\theta}X) \cdot \vec{s}$ tangential velocity of the plate

V_{in} volume of ingress/egress flow

V_e non-dimensional volume of ingress/egress flow

$\vec{W} = U\nabla(\bar{\phi} - x)$

$\vec{X}_0 = (x_0, y_0, z_0)$ coordinate system refers to Earth.

$\vec{X} = (x, y, z)$ coordinate system travels with forward speed U

$\vec{X}' = (x', y', z')$ coordinate system fixed to structure

Abbreviation

BVP boundary value problem

LEV leading edge vortex shedding

MTF multiple transition function

NACA national advisory committee on aeronautics

CPU computer processing unit

CFD computational fluid dynamics

Re Reynolds number

List of figures

List of tables

Contents

Chapter 1 Introduction and background

1.1 Introduction

Lifting bodies have been widely used in marine structures. Those include hydrofoils for supporting hydrofoil boats, screw propellers and sails for propulsion, rudders for the manoeuvring and anti-roll fins etc. Fluid dynamics used for these bodies can help the understanding of their lifting generation mechanism, which can lead to the optimization of the design of these structures. Research on these problems can improve their hydrodynamic performance and structural reliability, and enhance efficiency if applicable. Among the issues, understanding of the hydrodynamic performance of these marine structures is one of the most important aspects in naval architecture. Some other related problems involving separation effects include the damaged ship hydrodynamics and biomimetics. To model these problems is actually an issue related to vortex shedding or flow separation.

Vortex shedding or flow separation usually refers to the breakaway of the body surface streamline or separation of the boundary layer at sides of structures (Bachelor 1967, p326). This can be observed when a flow passes around a wedge shaped structure or a foil as shown in figure 1.1. Figure 1.1(a) shows the separated flow of a rigid wedge; the vortex wake forms and sheds away from the edge tip when the wedge moves towards the left hand side. Figure 1.1(b) presents an image of the flow around a foil with a small attack angle. On the upper surface of the foil, the boundary layer and vorticity are more visible due to thicker boundary layer in an adverse pressure gradient. From figure 1.1, we notice that the boundary layer is thin when compared with the scale of the structure; the viscous effect is mainly confined within the thin boundary

layer; along the body surface, there is no flow separation apart from at the sharp trailing edge; the wake flow leaves the sharp edge more or less tangentially to the body surface. Consequently, as discussed in the classic book entitled "*marine hydrodynamics"* (Newman, 1977), with the assumption that the fluid is incompressible, velocity potential theory can be adopted to describe the irrotational flow outside of the boundary layer.

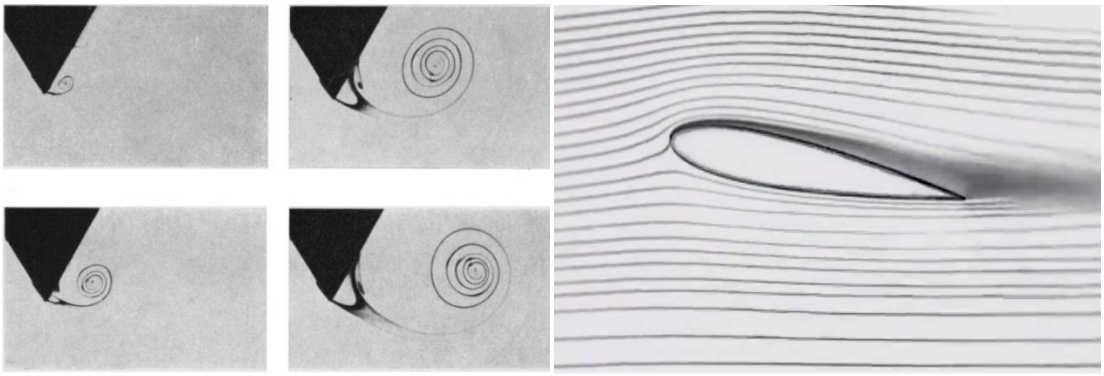

(a) (b)

Figure 1.1 Vortex shedding of (a) a wedge (Pullin & Perry, 1980) and (b) a foil, http://www. youtube.com/watch?v=ki-CxkRuAxY

Since potential flow theory is considered, the Reynolds number has no effect on the outer flow. However, for the theory to be applicable to a real problem, the Reynolds number shall be reasonably high (Newman, 1977). High Reynolds number is usually related to a thin boundary layer. For approximation, it would be appropriate to ignore the thickness of the boundary layer and extend the velocity potential theory into whole fluid domain.

The hydrodynamic problems concerned here are limited to vortex shedding at the sharp edges of structures with a smooth surface. It is assumed that vortices only shed from the tip of the sharp edge. The problem with flow separation along a smooth surface, usually with its separation point unknown, is beyond the scope of the present

study. However, many flow separation problems, including the lifting body problems and damaged compartment with an orifice, can be simulated using velocity potential flow theory with the sharp edge vortex shedding model.

In the framework of velocity potential flow theory, the potential flow around the structure is simulated through the boundary element method plus vorticity or dipole distribution for the vortex sheet. The velocity potential satisfies the Laplace equation in the fluid domain, the non-penetrating body surface condition, the proper Kutta condition, and the kinematic and dynamic free surface conditions when the body is near the water surface. The boundary in the integral equation is discretized and the algebraic equations are established based on Green's third identity. The boundary value problem (BVP) is solved numerically.

The simulation of lifting bodies with a sharp edge still has many challenges. Especially for marine structures when the free surface waves are present, the wave and the vortex shedding will affect the flow and hydrodynamic force significantly. The combined and coupled effects of the free surface and vortex on the marine structure can be highly complex. We shall track the motion of the free vortex and the free surface. Since viscosity has been ignored, the damping or dissipation of the vortices becomes a problem. However, for specific models, artificial treatments can be introduced.

When the motion of a foil near the free surface, which is related to high-speed-vehicle such as a hydrofoil, is considered, the problems of the dynamic stability and the sea-keeping performance of the boat becomes an important issue. In spite of the assumption that the speed is constant, the foil will experience oscillations induced by the waves. The problem is then decomposed into the steady motion problem (with

constant forward speed) and wave radiation and diffraction problems. The study on the steady motion of a thin foil at small attack angle in unbounded flow has been presented by Bachelor (1967), Newman (1977), Katz & Plotkin (1991). Giesing & Smith (1967), Yeung & Bouger (1979), Bal (1999) further studied the linear free surface effect on the steady motion of the foil with thickness. Grue, Mo & Palm (1988) investigated the linear surface wave effects of an oscillatory plate. However, the overall hydrodynamics of a foil with thickness in waves, as described above, seems absent. We attempt to investigate this specific problem with linearized free surface conditions. A flat dipole stretching from the trailing edge has been used to approximate the vortex wake. The body surface condition of wave radiation problem, which contains the well-known second order derivatives m_j terms, is imposed on the mean position. An efficient finite difference method is proposed to calculate the m_j terms. The appropriate free surface Green functions are adopted to solve the problems.

The shed vortex sheet of a foil with larger amplitudes of vertical and/or rotational oscillatory motions would move up and down; the body surface condition can no longer be imposed on its mean position. Therefore the nonlinear continuous vortex shedding shall be tracked through the time stepping scheme. Anderson et al (1998), Mantia & Dabnichki (2011) have investigated the oscillatory foil using inviscid flow theory, the former adopt complex potential theory and the latter used the boundary element method. Their results showed highly efficient combined vertical and rotational motions for propulsion. This was further supported by Ashraf et al (2011) based on Navier-Stokes (N-S) equations at higher Reynolds number. To study the nonlinear vortex shedding of a foil extensively, we develop a numerical scheme. The Kutta condition for the unsteady flow is proposed and the Kelvin theorem is imposed to

determine the strength of the newly shed vortex element. To avoid numerical difficulty due to the bundle of the vortex sheet, the continuous vortex sheet is replaced by point vortex after the vortex leaving the sharp edge. We extended the numerical scheme to simulate the motion of thin structures such as a plate. A similar time stepping scheme is applied to study the vortex shedding of an oscillatory plate and a compartment which consists of two curved plates. The damping effect due to vortex is analysed.

It is known that the free surface has significant effect on the hydrodynamics of a foil when it approaches the water surface. The nonlinear free surface effect has been studied by Faltinsen & Semenov (2008); the solutions were achieved through iteration. There are only a few studies adopting the nonlinear free surface and nonlinear vortex shedding scheme for the transient motion of a foil. Landrini, Lugni, & Bertram (1999) studied the steady motion of a foil near the water surface; however, the adopted Kutta condition would be problematic. In the present study, the developed nonlinear vortex shedding scheme is used. A foil with an impulsive motion of constant speed under the free surface is simulated in the Lagrangian framework. Simulations on the oscillatory vertical and rotational motions under the free surface are carried out.

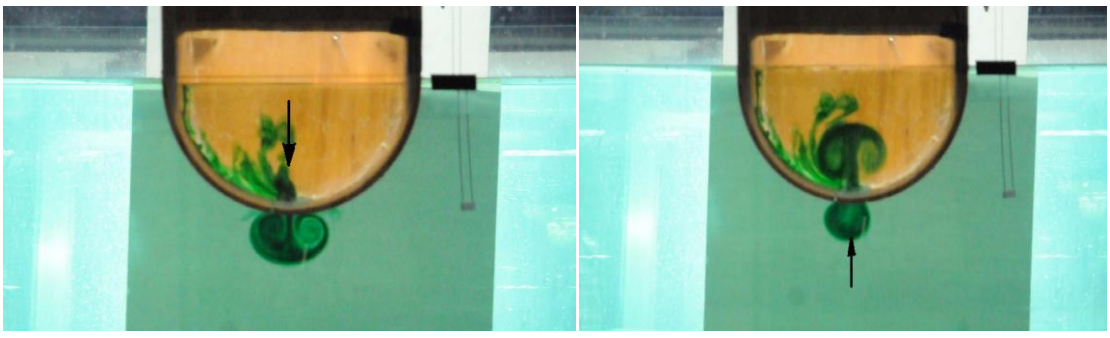

(a) (b)

Figure 1.2 Experiment on the vortex shedding at the orifice of a damaged compartment (Smith 2009), (a) egress (b) ingress

The vortex shedding at the orifice of a floating flooded compartment is similar to that of a foil near free surface. When a flooded compartment with an orifice is considered, the fluid inside and outside of the compartment is linked. Fluid will ingress/egress the compartment when it is in oscillatory motion. The shed vortices will move up and down along with the ingress/egress flow (see figure 1.2). Smith (2009) studied the forced motion of a compartment through a multi-pole expansion method; the vortex shedding has been ignored. Here the time stepping scheme is applied to study the heave motion of a compartment.

Since the viscosity of the fluid is not involved in the simulation, the dissipation of vortices does not exist. It is one of the major challenges in the present numerical study. Artificial dissipation function is introduced to damp the vortices. However, the treatment of the vortex damping is more or less arbitrary. For a foil advancing in the unbounded flow, a damping function based on time can be used as the vortices move far away enough from the body where the vortices have very little effect on the flow around the foil. The artificial damping function based on time is used for a flooded compartment with a symmetric orifice. The treatment of vortex wake is introduced as the artificial damping procedure does not affect the flow and the hydrodynamic force significantly.

1.2 Literature review

There is a large body of work on vortex shedding and the interaction of bodies and waves. Their success and ideas are extremely valuable to the present study. Those typical works are reviewed first below.

As vortex shedding at a sharp edge is considered, theories based on the potential flow can be categorized based on the ways to impose boundary conditions and the

ways to treat the vortex wake. The body surface condition can be satisfied either on its mean plane as an approximation if the body is thin, or on the exact body surface; the free surface boundary conditions can be linear or nonlinear; and the wake can be treated as a fixed plane or a free vortex sheet. The applicability of these theories mainly depends on their compatibility with the physical reality concerned.

The theory with its body surface condition satisfied on the centre plane and a flat vortex dipole imposed on the mean plane behind the trailing edge is the feature of the linear theory for a thin foil at small attack angle. Its solution is well established which can be found in many text books, including those by Batchelor (1967), Newman (1977), Katz & Plotkin(1991) etc. Analytical solution of the steady motion of a plate can be obtained from an integral equation. When the unsteady motion of a thin foil is of small amplitude and with low attack angle, one can also find the analytical solution without much additional effort (Newman, 1977). An integral term regarding the wake is introduced, which reflects the motion history. If the motion is harmonic or sinusoidal in time, the effect of wake is frequency-dependent after a sufficiently long period of time, which can be written in terms of the Hankel function, or the Theodorsen function. Lighthill (1960, 1970a, 1970b, 1971), Wu (1961, 1971a, 1971b) presented their studies on the swimming of a plate based on this method. There are practical limitations on the applications of such a theory: the body should be thin, the mean attack angle should be small and the oscillatory motion should be of small amplitude.

When the free surface exists nearby, free surface boundary conditions have to be imposed. Wu (1972) considered the incoming free surface wave. Its effect was however included only in the boundary condition on the foil surface and the BVP was still solved in the unbounded fluid domain. The frequency domain free surface Green function is

an effective tool to study the free surface effect of steady motion and harmonic oscillatory unsteady motion. The wave effects can be automatically included since the Green function satisfies free surface boundary conditions. Grue, Mo & Palm (1988) considered the full effects of the linear surface wave on an oscillatory plate without thickness through the appropriate Green function, in the context of propulsion of a ship, in the sense that energy can be extracted from waves as the hydrofoil moves forward with heave and pitch motions. Wu (1994a) also solved the unsteady motion of a three dimensional vertical plate piercing the water surface. A panel method over the plate surface was introduced to solve the BVP. We notice that the frequency domain Green function is valid for steady motion with harmonic motion. For general transient motion, the time domain free surface Green function should be adopted. However, the calculation of the integral involving the memory effect could be very time consuming because of the convolution term. Nevertheless, the free surface Green function method is convenient to find good results for linear problems with small attack angle and small amplitude oscillation.

As the ratio of thickness-chord becomes larger, the thickness effect cannot be ignored. The panel method over the real surface of the body, proposed by Smith & Pierce (1958) and Hess & Smith (1964), can be used to simulate the flow passing around a foil with thickness. For a lifting body, source, dipole and vortex wake can be adopted on and behind the foil; the solution can be obtained by solving the boundary integral equations, which are established based on the non-penetrating body surface condition (eg. Bristow, 1980, Katz & Plotkin, 1991) and the Kutta condition. Giesing & Smith (1967) developed a method to calculate the lifting force of a single or multi lifting bodies moving near the water surface. The sources and sinks were distributed

over the body surface together with a vorticity to satisfy the Kutta condition at the trailing edge. The adopted Green function satisfies the linear free surface boundary conditions and the radiation condition. Similar work based on the panel method for a hydrofoil at steady forward speed includes those by Yeung & Bouger(1979), Bal (1999) for two-dimensional foil and Xie & Vasselos (2007) for a three-dimensional foil. Zhu, Liu & Yue (2006) studied the propulsion of an oscillatory three-dimensional foil near the free surface, where linear free surface conditions are satisfied.

The frequency domain and time domain free surface Green functions both satisfy linear free surface boundary conditions. When the body is moving close to the free surface, the non-linearity of the water surface may become important. As a result, nonlinear free surface boundary conditions have to be imposed. Detailed discussions on this can be found in Giesing & Smith (1967). However, there are only a few works, including Faltinsen & Semenov (2008), which adopt fully non-linear free surface boundary conditions for foils. Their solution was obtained through iterations. Landrini, Lugni, & Bertram (1999) adopted the fully nonlinear free surface boundary condition, and the time stepping method was used. However, their implementation of vortex shedding scheme was problematic; the adopted Kutta condition was the same as those that have been criticized by Jones (2003).

Most of the theories discussed above adopted linear wake; the vortex wake dipole, which is the difference of the velocity potential of upper and lower sides at the trailing edge, is imposed on the mean plane stretching from the trailing edge. It is appropriate when the attack angle and the motion amplitude are small. When the attack angle or the amplitude of the oscillatory motion increases, the vortex wake behind the trailing edge would move up and down. The free vortex wake shed from the edges of the

structures can no longer be represented by a flat vortex sheet. In this case, a non-linear wake model should be used and body surface boundary conditions shall be satisfied at its instantaneous position.

Apart from the vortex wake, the well-known Kutta condition has to be imposed properly. Mathematically, the Kutta condition can be expressed in the form of the continuity of pressure or finite velocity. This is achieved through including the effect of flow circulation. When the nonlinear wake is involved, it is usually unsteady. In this sense, the corresponding Kutta condition is named the unsteady Kutta condition. The unsteady Kutta condition is one of the key issues when simulating the vortex shedding problem.

Early works treated the nonlinear wake using lump point vortices. Researchers have developed several methods to determine the strength and position of the newly shed vortex. Different schemes for the Kutta condition have been introduced and imposed either numerically or through conformal mapping. However, as mentioned by Sarpkaya (1989) and Jones (2003), most of the methods for the unsteady flow were achieved numerically, which might not have the full mathematical rigor. As commented by Jones (2003), several unsteady Kutta conditions were introduced and implemented numerically, including those by Maskell (1972), Kuwahara (1973), Clements (1973), Sarpkaya (1975), Katz (1981), and Cortelezzi et al (1997). The strength, position, and velocity of the newly introduced vortex element are chosen principally as a numerical treatment, in some of which, the rate of shed vorticity is given based on the velocity of a point near the sharp edge. The newly shed vortices are introduced either at fixed points or released at a variable position near the sharp edge. However, the results with these unsteady Kutta condition have large discrepancies when compared with the

experimental data of Keulegan& Carpenter (1958) and Pullin & Perry (1980).

To avoid the discontinuity of lump point vortices, a continuous vortex sheet or dipole was adopted to simulate the separated flow through conformal mapping in the work of Pullin & Perry (1980) and Graham (1980); although the averaged point vortex array, which is reduced from the continuous vortex sheet, was used to represent the vortex sheet released from the sharp edge. It seems that continuous vortex shedding at the sharp edge can give more accurate results than those by discrete lump point vortex when compared with experiment data (Nitsche & Krasny 1994).

The discussion of the vortex shedding at a wedge shaped trailing edge has been discussed by Giesing (1968) and Katz & Plotkin (1991, p245). The effect of the direction of vortex wake has significant effect on the lifting force and the drag. Kristiansen & Faltinsen (2008, 2010) adopted dipole segments to simulate the vortex shedding; the dipole was released continuously from the sharp edge. However, the Kutta condition is implemented by introducing extrapolation; two additional equations are established through the extrapolation of the local potential on the two sides of the sharp edge. The strength of the shed vortex dipole and its shed velocity are obtained based on an artificial treatment. Although continuous distribution of vortex dipole is used, the direction of the shed vortex is based on observation. However, their numerical results avoid large discrepancy when compared with the experimental data.

Rigorous imposition of the unsteady Kutta condition has been presented by Jones (2003) and Jones & Shelly (2005). The proposed mathematical procedure satisfied the Kutta condition analytically through asymptotic expansions. To circumvent the velocity singularity, the continual vortex sheet is required to be tangential at the edge of a moving plate. Similar to Jones, Alben (2009) adopted a continuous vortex shedding

model, in which the vortex sheet shed tangentially from the trailing edge. Jones' tangential vortex shedding model did avoid the singularity mathematically, which justified its validity itself. However, his tangential vortex shedding method would be problematic when a body with non-zero angled corner such as a wedge is considered.

In general, it is not possible to let the shed vortex wake be tangential to both sides of a wedge. However, we can seek new schemes for the simulation of vortex shedding at the edge. One possible method is to continue the mathematical procedure by modifying the local shape of the wedge tip, let its two sides be tangential to each other. Another possibility is to adopt a numerical unsteady Kutta condition which can lead to a good approximation to the fluid flow.

Let us go back to the physical essence of the Kutta condition. Observation from experiment shows that the vortex wake is formed in the vicinity of the area at the back side (view from the coming flow) of the edge, as shown in Figure 1.1(a). It is not shed from a single point, but a small region. Strictly speaking, the models to simulate the vortex shedding using vortex sheet or point vortex are an approximation technique for such a case. As the wedge tip vortex shedding is considered, it is difficult to impose the tangential Kutta condition to a body whose two sides are not joined tangentially. However, the Kutta condition is required to circumvent the singularity in the velocity field of the ideal flow. In the framework of potential flow, we shall choose a Kutta condition which can ensure the velocity field to be finite at the trailing edge. Since the sharp edge is considered, the vortex wake released from the tip of the wedge shall be treated as a continuous distribution of dipoles.

Apart from the unsteady Kutta condition and the treatment of the vortex sheet, the interaction of vortices and the free surface or surface waves is the interest of present

study. Simulation of floating bodies near a free surface by pure potential flow cannot include the damping effect due to vortex shedding. It is known that the sea-keeping theory based on the potential theory over-predicts the roll motion of a ship as the damping effect due to viscosity and the vortex shedding at the bilge is ignored in the motion equation. Therefore, a reliable and accurate procedure or method that can estimate the damping of vortex shedding becomes most valuable.

As the floating body with sharp edges, like the bilge keel or the orifice of a damaged ship, is considered, the shed vortices, surface wave and the structure shall be tracked simultaneously. Figure 1.2 shows the vortex shedding at the sharp edge of the orifice of a flooded compartment in oscillation (Smith, 2009). As the flow ingresses or egresses the orifice, vortices are shed up and down. When studying the oscillatory damaged compartment, the sea-keeping theory based on pure velocity potential theory without vorticity cannot capture the phenomena of vortex shedding and its effects. The discrepancy, especially at lower frequency, between the predicted hydrodynamic force and the experimental data has been found (Smith 2009). Work by Downie, Bearman & Graham (1988) included the vortex damping effect from the sharp corner of a floating rectangular barge in waves; the sharp edge was mapped to an infinite wedge, the shed vortex was then matched with the main flow; the predicted response avoided the excessive roll motion. Kristiansen & Faltinsen (2008, 2009) revealed that the discrepancy of the wave response of a rectangular barge predicted by linear potential theory and the experiment data and the simulation results which included the vortex shedding explained the discrepancy quite well. Gaillard, Xu & Wu (2011) simulated the motion of a damaged barge in waves using software WAMIT which is based on pure linear potential flow theory. They introduced an additional damping coefficient which

was obtained from the harmonic motion of a damaged compartment in the unbounded flow. The introduced damping coefficient reduces the discrepancy of the results from pure potential flow and the experimental data. It is still a challenge to model the motion of a damaged barge directly. Different from the sloshing problem, the free surfaces inside and outside of the compartment are linked. The coupled motion, which involves vortex shedding, motion of the floating body and waves, makes the problem extremely complicated.

Since the surface wave is involved, the far field wave radiation condition has to be addressed properly. The far field condition is satisfied automatically when the free surface Green function is applicable in the linear case. In general case, the computation domain is always finite for time stepping simulation. As the wave propagates outward, it has to either pass through the truncated boundary with no reflection or be absorbed using a damping zone. There are several methods that are useful for linear free surface problems, including the Sommerfeld condition (Sommerfeld, 1949), Multiple transition function (MTF) (Liao, et al 1984) and damping zone method. For nonlinear problems, the damping zone is more effective and practical; it can absorb the wave energy without significant reflection (e.g. Tanizawa & Swada 1996, Wang & Wu 2006).

1.3 Context of present study

The purpose of our study is to develop a faster and more accurate tool to study the hydrodynamic characteristics of structures with sharp corners. The integral equation is applied on the boundary which is divided into small elements, and the matrix equations are established based on the boundary conditions. Those existing methods or schemes may have difficulties in treating the problem concerned here. However, the success of those mathematicians and hydrodynamicists gives a great amount of

valuable information and their ideas inspire us to push into new territories.

We first consider the linear wave radiation and diffraction of a foil near the free surface in chapter 3 after the basic theory and equations are presented in chapter 2. The non-penetration body surface condition for the steady motion and diffraction problem is satisfied on the exact foil surface other than its centre plane. The linearized body surface condition is imposed on its mean position. The m_j terms are calculated through finite difference. The effects of submergence, attack angle and frequency together with various reciprocity relationships are investigated.

We introduce a time stepping vortex shedding scheme to approximate the continuous vortex shedding. The nonlinear vortex shedding of a foil with large amplitudes of vertical and rotational motions for the purpose of propulsion, energy harvesting and flying is investigated in chapter 4. Extensive studies on the effects of oscillation amplitudes, frequency, the effective attack angle, and phase differences of vertical and rotational motions are carried out for different motion modes. When the thickness of the foil is reduced to zero, the foil can then be replaced by a plate. The fluid flow is then described using a vortex distribution. The time stepping scheme is again applied to simulate the vortex shedding of a plate with minor modification. Numerical results on small amplitude oscillation and large amplitude motion are investigated. Further application is applied to an opening semi-column compartment with symmetric orifice at the bottom. The damping effect due to the vortices is investigated.

The transient motion of a foil near non-linear free surface is studied in chapter 5. The simulations involve the interaction of foil, free vortices and free surface. A foil with an impulsive motion of constant speed and/or the oscillatory vertical and rotational

motions under the free surface is studied. The transient wave effect at different velocities and submergences is investigated; the performance for the purpose of propulsion, energy harvesting and flying are discussed.

Chapter 6 moves to the simulation of the vortex shedding of a floating flooded compartment in oscillatory motion. An orifice at the bottom represents the damaged structure. The thickness of the compartment is included and the sharp edge of the orifice is modified like the trailing edge of a foil. The numerical scheme for the vortex shedding would then be applied to model the damaged compartment. As the compartment moves up and down, the ingress and egress flow through the orifice of the compartment makes the problem differ from the sloshing problem. There are very strong interactions between the structure, waves and free vortices. Simulations are carried out to investigate the effects of motion amplitude, frequency and damaged orifice size. Apart from the hydrodynamic force, the flow rate through the orifice is examined.

Chapter 2 The mathematic equations for vortex shedding problems

Throughout the studies in the present thesis, there are some important definitions of coordinate systems, governing differential equations and integral equations that shall be outlined here.

2.1 Coordinate systems

First of all, we shall introduce the coordinate systems. We define three different coordinate systems similar to those in the sea-keeping theory (Newman 1977, Wu 1986):

(1) $\vec{X}(x_0,\ y_0,\ z_0)$ is fixed referring to the Earth, in which x_0oy_0 is along the undisturbed water surface and z_0 points upwards if applicable.

(2) $\vec{X}(x,\ y,\ z)$ travels with the structure with the forward speed U in the direction of x axis. xoy is on the mean water surface if applicable; it is originated at the mean position of the rotation centre of the body when it is in the unbounded flow.

(3) $\vec{X}'(x',\ y',\ z')$ is a coordinate system fixed on the structure.

These three coordinate systems can be transformed from one to the other. We have

$$\vec{X}(x,\ y,\ z)=\vec{X}(x_0,\ y_0,\ z_0)-(\int U dt\ ,0,\ 0) \tag{2-1}$$

and for small amplitude oscillatory motion

$$\vec{X}'(x',\ y',\ z')=\vec{X}(x,\ y,\ z)-(\vec{A}_T+\vec{A}_R\times\vec{X}') \tag{2-2}$$

where $\vec{A}_T=(A_1,A_2,A_3)$, $\vec{A}_R=(A_4,A_5,A_6)$ are the translational and rotational displacements of the structure relative to $\vec{X}(x,\ y,\ z)$.

In the case of large amplitude oscillation, Eq.(2-2) should be replaced by

$$\vec{X}'(x',\ y',\ z')=\vec{X}(x,\ y,\ z)-(\vec{A}_T+M\times\vec{X}') \tag{2-3}$$

where

$$M=\begin{bmatrix}\cos\theta_4\cos\theta_6-\cos\theta_5\sin\theta_4\sin\theta_6 & -\cos\theta_5\cos\theta_6\sin\theta_4-\cos\theta_4\sin\theta_6 & \sin\theta_4\sin\theta_5\\ \cos\theta_6\sin\theta_4+\cos\theta_4\cos\theta_5\sin\theta_6 & \cos\theta_4\cos\theta_5\cos\theta_6-\sin\theta_4\sin\theta_6 & -\cos\theta_4\sin\theta_5\\ \sin\theta_5\sin\theta_6 & \cos\theta_6\sin\theta_6 & \cos\theta_5\end{bmatrix}$$

$(\theta_4,\theta_5,\theta_6)$ are the Euler angles

Here we consider the two-dimensional problem and variations in y axis are eliminated. The translational and rotational velocities become $\dot{\bar{A}}_T=(\dot{A}_1,0,\dot{A}_3)$, $\dot{\bar{A}}_R=(0,\dot{A}_5,0)$, and

$$M=\begin{bmatrix}1 & 0 & 0\\ 0 & \cos\theta_5 & -\sin\theta_5\\ 0 & 0 & \cos\theta_5\end{bmatrix}$$

where the over-dot implies the temporal derivative.

2.2 Some basic equations for vortex shedding

Under the assumption that the fluid is ideal and incompressible and its density is constant, the velocity potential ϕ satisfies the Laplace equation

$$\nabla^2\phi=\frac{\partial^2\phi}{\partial x^2}+\frac{\partial^2\phi}{\partial z^2}=0 \tag{2-4}$$

in the fluid domain.

The non-penetrating boundary condition on the body surface gives

$$\frac{\partial\phi}{\partial n}=U\cdot n_x+(\dot{A}_1+\dot{A}_5Z,\ \dot{A}_3-\dot{A}_5X)\cdot\vec{n} \tag{2-5}$$

where $\vec{n}=(n_x,n_z)$ is the inward normal vector of the body surface, $(X,Z)=(x-x_c,z-z_c)$, and (x_c,z_c) is denoted as the rotation centre.

In the Eulerian system, the free surface S_F can be written as

$$z=\varsigma(x,t) \tag{2-6}$$

The dynamic and kinematic free surface boundary conditions on $z = \varsigma(x,t)$ are

$$\frac{\partial \phi}{\partial t} - U\phi_x + \frac{1}{2}\nabla\phi\nabla\phi + gz = 0 \tag{2-7}$$

$$\frac{\partial \varsigma}{\partial t} - U\varsigma_x = \phi_z - \phi_x\varsigma_x \tag{2-8}$$

where g is the acceleration due to gravity.

When the free surface boundary condition is linearized, on $z = 0$ we have

$$\frac{\partial \phi}{\partial t} - U\phi_x + gz = 0 \tag{2-9}$$

$$\frac{\partial \varsigma}{\partial t} - U\varsigma_x = \phi_z \tag{2-10}$$

Combining Eqs.(2-6)(2-9) & (2-10), we have

$$(\frac{\partial}{\partial t} - U\frac{\partial}{\partial x})^2\phi + g\frac{\partial \phi}{\partial z} = 0 \tag{2-11}$$

While in the Lagrangian framework, the nonlinear free surface boundary conditions can be written as

$$\frac{d\phi}{dt} = \frac{1}{2}\nabla\phi\nabla\phi - gz \tag{2-12}$$

$$\frac{dx}{dt} = -U + \frac{\partial \phi}{\partial x}, \quad \frac{dz}{dt} = \frac{\partial \phi}{\partial z} \tag{2-13}$$

Once the solution is found, we have the pressure

$$p_{re} = -\rho(\phi_t - U\phi_x + \frac{1}{2}\nabla\phi\nabla\phi + gz) \tag{2-14}$$

where ρ is the density of the fluid.

When Eq.(2-14) is linearized, we have

$$p_{re} = -\rho(\phi_t - U\phi_x + gz) \tag{2-15}$$

The hydrodynamic force can be obtained through pressure integration over the body

surface. We have

$$F_i = \int_{S_0} p_{re} n_i dS \ , \ i = 1,3,5 \tag{2-16}$$

where $(n_1, n_3, n_5) = (n_x, n_z, \vec{X} \times \vec{n}),\ \vec{X} = (x - x_c, z - z_c)$.

The Kutta condition requires the velocity to be finite at the sharp trailing edge of the structure, or

$$\nabla \phi = \ finite \tag{2-17}$$

at $\vec{x}_T = (x_T, z_T)$ which are the coordinates of the trailing edge.

If the body is in the unbounded flow, the perturbed velocity by the body in the far field disappears, or

$$\nabla \phi = 0 \ \text{as} \ x \to +\infty \tag{2-18}$$

When the free surface is present, the perturbed velocity far away from the body shall be finite or

$$\nabla \phi = \ finite \ \ \text{as} \ x \to \pm\infty \tag{2-19}$$

The potential is discontinuous across the vortex sheet. The difference is usually defined as a dipole, or

$$\mu = \phi_{w+} - \phi_{w-} \tag{2-20}$$

Here when one walks along the wake starting from the trailing edge, ϕ_{w+} and ϕ_{w-} in Eq.(2-20) are the potentials on the right and left hand sides respectively. The normal velocity across the wake is continuous, or

$$\frac{\partial \phi_{w+}}{\partial n} = -\frac{\partial \phi_{w-}}{\partial n} \tag{2-21}$$

where the negative sign is because of the change in direction of the normal from one side of the wake to the other side.

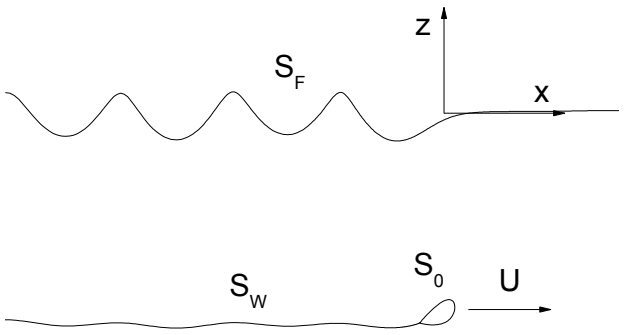

Figure 2.1 The integral boundary of a foil in steady motion near free surface

2.3 The integral boundary equation

The problem can be solved through the boundary integral equation. For a point $p(x,z)$ in the fluid field the potential can be given by Green's third identity

$$2\pi\phi(p)=\int_{S_0+S_F+S_w+S_C}[\frac{\partial G(p,q)}{\partial n_q}\phi(q)-G(p,q)\frac{\partial\phi(q)}{\partial n_q}]ds_q \tag{2-22}$$

where $G(p,q)$ is the Green function, $q(\xi,\eta)$ is the point along the integral boundary, n_q is the normal at point q, S_0 and S_C are the foil surface and control surface, and S_w indicates the wake surface as shown in figure 2.1.

Substituting Eqs.(2-20) & (2-21) into Eq.(2-22), we have

$$2\pi\phi(p)=\int_{S_0+S_F+S_C}[\frac{\partial G(p,q)}{\partial n_q}\phi(q)-G(p,q)\frac{\partial\phi(q)}{\partial n_q}]dS_q+\int_{S_w}\frac{\partial G(p,q)}{\partial n_q}\mu(q)dS_w \tag{2-23}$$

Eq.(2-23) will be modified for specific problems and will be used to solve the BVP throughout the thesis.

With above equations, we will study the linear and nonlinear vortex shedding of marine structures in the following chapters.

Chapter 3 Linear theory for a submerged hydrofoil advancing in waves

3.1 Description of the overall problem

We consider a hydrofoil advancing in water waves with small attack angle. This is one of the major concerns of high speed vehicles such as hydrofoil craft. It shall provide a steady lifting force to balance the weight of the ship. As it encounters incoming waves, the hydrofoil moving along with the craft would experience an oscillatory flow field induced by the waves, leading to a combined wave radiation and diffraction. The overall motion is decomposed into the steady forward speed problem and periodic wave radiation and diffraction problem. The linearized free surface and body surface boundary conditions are imposed. The free surface boundary conditions are accounted for through the Green function. The integral equation involves only the body surface since the Green function satisfies the free surface boundary conditions. As the hydrofoil thickness is considered, the body surface condition is no longer satisfied on the axis line of the foil, but on the mean position of the foil surface. In this sense, for the forward steady problem and wave diffraction problem without body oscillation, the boundary condition on the body surface is satisfied on its exact location. When there is a body oscillation, the body surface condition is satisfied on its mean position. A flat dipole imposed behind the trailing edge is used to approximate the steady and unsteady vortex wake, as shown in figure 3.1.

As the overall hydrodynamic behaviour of a hydrofoil advancing in periodic waves is considered, the total potential Φ can be written as

$$\Phi(x,z,t) = U\bar{\phi}(x,z) + \mathrm{Re}[\tilde{\phi}_p(x,z)e^{i\omega t}] \qquad (3\text{-}1)$$

where $\bar{\phi}(x,z)$ and $\tilde{\phi}_p(x,z)$ are the potential due to steady motion and the combined incident, radiation and diffraction potentials, respectively. The latter are based on the

assumption that the problem is already sinusoidal temporally, $\omega = \omega_0 \pm \frac{\omega_0^2}{g} U$ is the encounter frequency, + and – correspond to waves from the right and left hand sides respectively, ω_0 is the wave frequency.

The potential $\tilde{\phi}_p$ related to the periodic motion can be written as

$$\tilde{\phi}_p = A_0\varphi_0 + A_1\varphi_1 + A_3\varphi_3 + A_5\varphi_5 + A_7\varphi_7 \tag{3-2}$$

where φ_0 is the potential due to the incident wave and φ_7 is due to its diffraction by the hydrofoil; A_0 is the incoming wave amplitude, and $A_7 = A_0$; φ_j ($j = 1, 3, 5$) are the potentials due to surge, heave and pitch motions respectively; $A_i (i = 1, 3, 5)$ are the corresponding amplitudes of these motions.

The potentials due to steady motion in calm water and the radiation and diffraction are calculated separately. Once the steady motion and the unsteady motions are solved, the complete hydrodynamics of the foil can be obtained through superposition.

3.2 Steady motion of a hydrofoil under the free surface

3.2.1 Equations for the steady motion

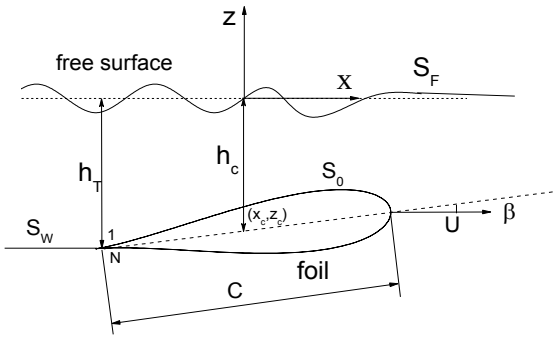

Figure 3.1 Sketch of a submerged hydrofoil advancing near the water surface

The sketch of a hydrofoil moving near the free surface at constant forward speed U is shown in figure 3.1. The distance of the trailing edge and the rotation centre to the mean water line are h_T and h_C respectively. In this chapter the rotation centre (x_c, z_c) is at the centre of the chord. We define the Froude number as $Fn = \frac{U}{\sqrt{gC}}$, and denote C as the chord length, and β as the mean attack angle.

The potential $\bar{\phi}$ due to the steady forward motion satisfies the Laplace equation

$$\nabla^2 \bar{\phi} = 0 \tag{3-3}$$

in the fluid domain.

The boundary conditions for the steady problem, given in Eqs.(2-5) & (2-11) become

$$\frac{\partial \bar{\phi}}{\partial n} = n_x \tag{3-4}$$

on the foil surface, and

$$\kappa \bar{\phi}_z + \bar{\phi}_{xx} = 0 \tag{3-5}$$

on the free surface, where $\kappa = g/U^2$.In the far field, we have

$$\nabla \bar{\phi} = 0, \quad x \to +\infty \tag{3-6}$$

and

$$\nabla \bar{\phi} = finite, \quad x \to -\infty. \tag{3-7}$$

Once the potential is solved, the steady hydrodynamic force F_{sj} is obtained from the full Bernoulli equation since the product term may be more significant near the body. We have

$$F_{sj} = \int_{S_0} p_{re} n_j dS = -\rho U^2 \int_{S_0} (-\bar{\phi}_x + \frac{1}{2} \nabla \bar{\phi} \nabla \bar{\phi}) n_j dS, \; j = 1,\ 3,\ 5 \tag{3-8}$$

where the gravity term is not included, as it contributes a buoyancy force.

Here we defined the non-dimensional pressure c_P and non-dimensional resistance c_R, lift c_L and moment c_M as

$$c_p = \frac{2p_{re}}{\rho U^2} \tag{3-9}$$

$$c_R = \frac{2F_{s1}}{\rho U^2 C} = -\frac{1}{C}\int_{S_0} c_p n_x dS \tag{3-10}$$

$$c_L = \frac{2F_{s3}}{\rho U^2 C} = \frac{1}{C}\int_{S_0} c_p n_z dS \tag{3-11}$$

$$c_M = \frac{4F_{s5}}{\rho U^2 C^2} = \frac{2}{C^2}\int_{S_0} c_p(-Xn_z + Zn_x)dS \tag{3-12}$$

Since the free surface Green function satisfies the free surface boundary conditions automatically, the boundary integral equation in Eq.(2-23) only involves the foil surface and the wake. The Green function can be written as (Wehausen & Laitone 1960)

$$G(p,q) = \ln r + \ln r' + 2p.v.\int_0^\infty \frac{e^{k(z+\eta)}}{k-\kappa}\cos k(x-\xi)dk + 2\pi e^{\kappa(z+\eta)}\sin\kappa(x-\xi) \tag{3-13}$$

where $r = \sqrt{(x-\xi)^2 + (z-\eta)^2}$, $r' = \sqrt{(x-\xi)^2 + (z+\eta)^2}$, and $p.v.$ indicates the Cauchy principal integral.

To solve the steady potential $\bar{\phi}$, the Constant Boundary Element Method (CBEM) is adopted. The boundary of the foil surface is divided into N segments. Thus Eq.(2-23) can be written as

$$\sum_{j=1}^{N}[a_{ij}\phi_j - b_{ij}\frac{\partial \phi_j}{\partial n_q}] + \int_{-\infty}^{\xi_T}\mu(q)\frac{\partial G}{\partial n_q}dS_w = 0 \tag{3-14}$$

where

$a_{ij} = \int_{S_j}\frac{\partial G(p,q)}{\partial n_q}dS_q$, $b_{ij} = \int_{S_j} G(p,q)dS_q$, and i, j are the numbers of the segments

corresponding to p, q respectively. More details on the discretization and collocation of the foil can be found in the book of Katz & Plotkin (1991).

Since the attack angle is small, the linearized vortex sheet is adopted to approximate the wake flow. Physically, the pressure on the two sides of the vortex wake shall be equal. From the linear Bernoulli equation we have

$$\frac{\partial \phi_{w+}}{\partial t} - U\frac{\partial \phi_{w+}}{\partial x} = \frac{\partial \phi_{w-}}{\partial t} - U\frac{\partial \phi_{w-}}{\partial x} \tag{3-15}$$

Noting that $\frac{\partial \phi_{w+}}{\partial t} = \frac{\partial \phi_{w-}}{\partial t} = 0$ in the steady flow, we then have

$$\frac{\partial \mu}{\partial x} = 0 \text{ or } \mu = const. \tag{3-16}$$

The dipole $\mu(q)$ in Eq.(3-14) is constant. This is then obtained by the difference of the potentials on the two elements attached to the trailing edge of the foil. As a result, Eq.(3-14) has N unknowns which are obtained from the N conditions imposed at the centres of N segments.

3.2.2 Pressure distribution and steady force on the foil

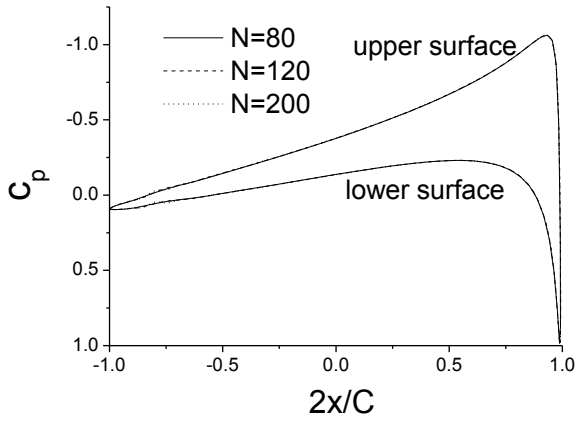

Figure 3.2 Pressure distribution on a symmetric Joukowsky foil with $t_{ck}/C = 11.78\%$, $h_T/C = 1.0$ at $Fn = 1.0$, $\beta = 5^0$

To verify the present method though convergence study and comparison,

simulations are made for a symmetric Joukowsky foil with the ratio of thickness t_{ck} to chord C equals to 11.78% at mean attack angle $\beta = 5^0$, with the number of elements on the body $N = 80, 120$ and 200 respectively. Figure 3.2 presents the non-dimensionalized pressure distribution over the foil surface. It can be seen that the results from these three meshes are graphically indistinguishable. Table 3.1 gives further results for non-dimensionalized resistance, lift and pitch moment. The table shows that these meshes have given the converged results.

Table 3.1 The resistance, lift and pitch moment on a symmetric Joukowsky foil with $t_{ck}/C = 11.78\%$, $h_T/C = 1.0$ at $Fn = 1.0, \beta = 5^0$.

	N=80	N=120	N=200
c_R	0.02182	0.02194	0.02207
c_L	0.34116	0.34267	0.34399
c_M	0.15297	0.15275	0.15275

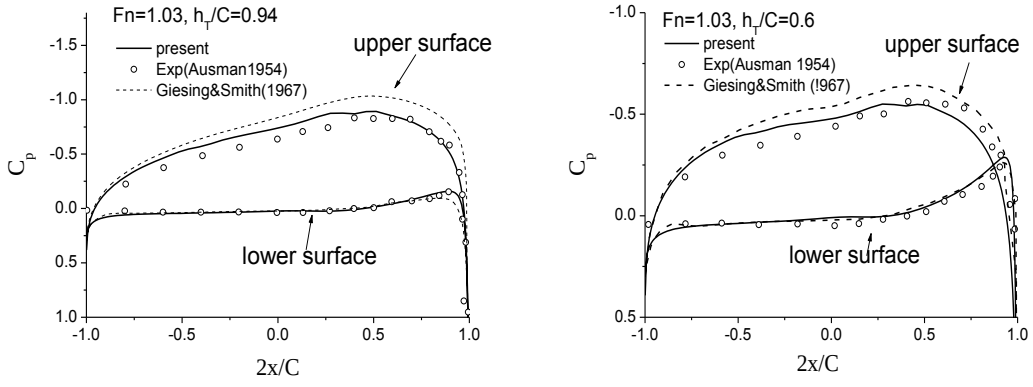

(a) (b)

Figure 3.3 Pressure distribution on the NACA4412 foil at $Fn = 1.03$ and $\beta = 5^0$ (a) $h_T/C = 0.94$ (b) $h_T/C = 0.6$

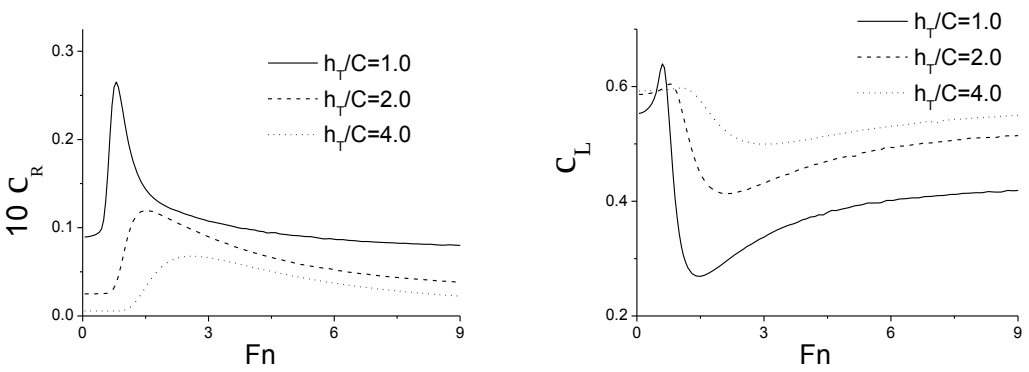

(a)

(b)

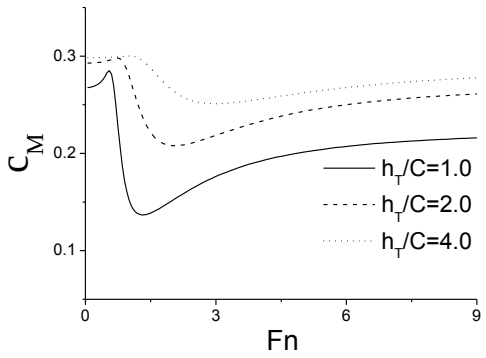

(c)

Figure 3.4 Resistance, lift, and moment on a symmetric Joukowsky foil of $t_{ck}/C = 11.78\%$ at $\beta = 5^0$ and different submergence. (a) resistance (b) lift (c) pitch moment

We now use the present method to consider the NACA4412 foil. The pressure distributions over the body surface are presented in Figure 3.3. They are compared with the experimental data of Ausman (1954), taken manually from the paper of Giesing & Smith (1967), and very good agreement can be found. The numerical results of Giesing & Smith (1967) are also included in the figure, which are slightly different on the upper surface. They adopted source distribution and an additional vortex to account for the flow with circulation, and the Kutta condition is satisfied when the

velocities at the elements of the trailing edge are equal. This treatment is right for steady motion. The results of Giesing & Smith (1967) shall be the same as present results; however, discrepancies can be observed. This could be caused by fewer elements they used or the accuracy of the computer in 1960s.

Having verified the method, figure 3.4 gives the resistance, lifting force and moment on a symmetric Joukowsky foil with $t_{ck}/C = 11.78\%$ against forward speed at different submergence. As can be seen in figure 3.4(a), the resistance coefficients increase with Fn initially. They reach a peak at $Fn \approx 0.8$, $Fn \approx 1.5$, $Fn \approx 2.4$ for $h_T/C = 1.0$, $h_T/C = 2.0$, $h_T/C = 4.0$ respectively and then decrease gradually at larger Fn. We notice that the resistance decreases significantly as the submergence h_T/C becomes larger. In the perspective of energy, the energy of the wave comes from the work done to water by the foil. Hence the increase of resistance usually refers to the wave making resistance. Figure 3.4(b) gives the lifting forces which increase as the speed increases and after the curves reach their peaks they decrease. These curves for the lifting force then go up gradually and tend to a finite limit. There is a similar trend in the curves for the moment. We may also notice that the resistance is one magnitude smaller than the lift. The presence of free surface has a significant effect on the hydrodynamic force due to the induced surface waves. The forward speed in $\kappa = g/U^2$ in Eqs.(3-5) or (3-13) indicates the characteristic of the induced wave. Larger U means smaller κ and longer wavelength. When the submergence is fixed, the variation of the lifting force is mainly due to the changes of the local flow induced by surface wave. When U is small, there would be more than one wavelength above the foil; as U increases, the wavelength increases as well. The foil can be beneath the crest of the wave which is followed by a trough. This can explain the changes of the

lifting force corresponding to the forward speed. When the submergence increases, the free surface will have less effect as shown in the figure.

3.3 Hydrofoil with small amplitude harmonic oscillation in waves

3.3.1 Mathematic equations on the radiation and diffraction problems

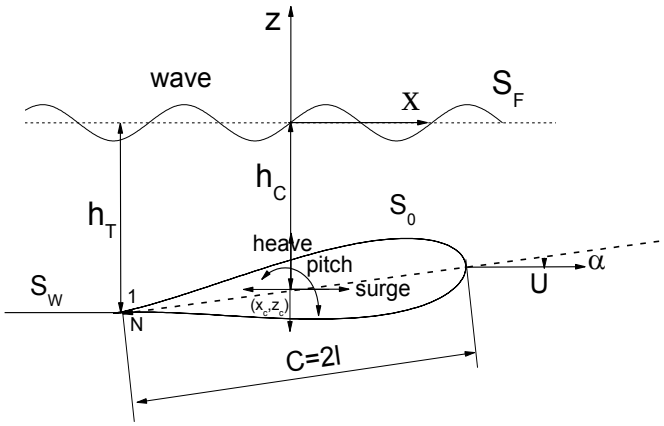

Figure 3.5 Sketch of a hydrofoil advancing in waves

Let us consider an oscillatory foil travelling in waves with constant forward speed. The incoming wave is assumed sinusoidal both temporally and spatially and the hydrofoil is in harmonic surge, heave and pitch motions. The potentials due to wave radiation and diffraction satisfy Laplace equation

$$\nabla^2\varphi_j = 0,\ j = 1,\ 3,\ 5,\ 7 \tag{3-17}$$

in the fluid domain.

The body surface condition can be written as (Newman 1978)

$$\frac{\partial\varphi_j}{\partial n} = i\omega n_j + Um_j,\ (j = 1,\ 3,\ 5) \tag{3-18}$$

$$\frac{\partial\varphi_7}{\partial n} = -\frac{\partial\varphi_0}{\partial n} \tag{3-19}$$

where

$$(m_1, m_3, m_5) = -\left(\frac{\partial \bar{\phi}_x}{\partial n}, \frac{\partial \bar{\phi}_z}{\partial n}, \frac{\partial [z(\bar{\phi}_x - 1) - x\bar{\phi}_z]}{\partial n} \right).$$

Its boundary condition on the free surface can be written as (Wehausen & Laitone, 1960; Wu & Eatock Taylor 1987)

$$\varphi_{jz} + \frac{\tau^2}{\nu}\varphi_{jxx} - 2i\tau\varphi_{jx} - \nu\varphi_j = 0 \tag{3-20}$$

where $\tau = \frac{U\omega}{g}$, $\nu = \frac{\omega^2}{g}$

The potential due to the incident wave can be written as

$$\varphi_0 = \frac{g}{i\omega} e^{k_0 z \pm i(k_0 x + \varepsilon_w)} \tag{3-21}$$

where $k_0 = \frac{\omega_0^2}{g}$ is the wave number and ε_w is the phase of the incoming wave with respect to the foil centre.

Once the BVP is solved, the force and moment on the foil can be obtained from the integration of pressure. We have (Newman 1978, Wu & Eatock Taylor 1987)

$$F_{uj} = \mathrm{Re}[(A_0 F_{uj0} + A_1 F_{uj1} + A_3 F_{uj3} + A_5 F_{uj5} + A_0 F_{uj7})\ e^{i\omega t}] \tag{3-22}$$

where F_{uji} is the complex amplitude of the unsteady force.

The force due to wave radiation and diffraction is obtained from the linear Bernoulli equation as the body surface condition is linear. We have the radiation wave force

$$F_{u_{ji}} = -\rho \int_{S_0} (i\omega\varphi_i + \vec{W} \cdot \nabla\varphi_i) n_j dS\ ,\ i,\ \ j = 1,\ 3,\ 5 \tag{3-23}$$

where $\vec{W} = U\nabla(\bar{\phi} - x)$, which has included the effect of steady potential.

The non-dimensionalized force can be written as

$$f_{u1j} = \frac{2F_{u1j}}{\rho g C},\ f_{u3j} = \frac{2F_{u3j}}{\rho g C},\ f_{u5j} = \frac{4F_{u5j}}{\rho g C^2}, \tag{3-24}$$

The combined incident wave force and diffraction wave force can be written as

$$F_{w_j} = (F_{u_{j0}} + F_{u_{j7}}) = -\rho \int_{S_0} [i\omega(\varphi_0 + \varphi_7) + \vec{W} \cdot \nabla(\varphi_0 + \varphi_7)] n_j dS \,, \quad j = 1,\ 3,\ 5 \tag{3-25}$$

Similar to Eq.(3-24), we have

$$f_{wj} = \frac{2F_{wj}}{\rho g C}, \text{ (j=1, 3)}, \quad f_{w5} = \frac{4F_{w5}}{\rho g C^2} \tag{3-26}$$

One may notice that the linear unsteady body surface boundary condition Eq.(3-18) contains the second order derivatives of the steady potential. This is usually problematic in numerical calculation. The accuracy of this term is a major challenge in this type of numerical solution. Zhao & Faltinsen (1989) attempted to calculate the m_j term directly. The second order derivatives of the potential near the body surface were calculated and the m_j terms on the body surface were obtained through extrapolation. Wu (1991) proposed a numerical scheme to calculate the m_j term by solving the boundary integral equation of the first order derivatives of the steady potential. Here an efficient numerical scheme based on the finite difference method is proposed. The m_j terms are calculated through the finite difference of the potential derivative $\bar{\phi}_x$ and $\bar{\phi}_z$ along the foil surface. We have

$$m_1 = -\frac{\partial \bar{\phi}_x}{\partial n} = -\bar{\phi}_{xx} n_x - \bar{\phi}_{xz} n_z = -\frac{\partial \bar{\phi}_z}{\partial s} \tag{3-27}$$

$$m_3 = -\frac{\partial \bar{\phi}_z}{\partial n} = -\bar{\phi}_{zx} n_x - \bar{\phi}_{xx} n_z = \frac{\partial \bar{\phi}_x}{\partial s} \tag{3-28}$$

where $\vec{s} = (s_x, s_z) = (n_z, -n_x)$ is the vector in the tangential direction of the body surface. From m_1, m_3, we have

$$m_5 = n_z(\bar{\phi}_x - 1) - n_x \bar{\phi}_z + Zm_1 - Xm_3 \tag{3-29}$$

For the potential related to the harmonic motion, the Green function can be written as (Wehausen & Laitone 1960, Wu & Eatock Taylor 1987)

$$G = \ln r - \ln r' + p.v.\int_0^\infty e^{k(z+\eta)}\left[A(k)e^{ik(x-\xi)} + B(k)e^{-ik(x-\xi)}\right]dk + \sum_{j=1}^{4} b_j e^{k_j(z+\eta)} e^{\pm ik_j(x-\xi)} \qquad (3\text{-}30)$$

when $\tau \le \frac{1}{4}$, where

$$A(k) = \frac{1}{\sqrt{1-4\tau}}\left(\frac{1}{k-k_1} - \frac{1}{k-k_2}\right)$$

$$B(k) = \frac{1}{\sqrt{1+4\tau}}\left(\frac{1}{k-k_3} - \frac{1}{k-k_4}\right)$$

$$k_1 = \frac{\nu}{2\tau^2}(1-2\tau+\sqrt{1-4\tau}),\ k_2 = \frac{\nu}{2\tau^2}(1-2\tau-\sqrt{1-4\tau})$$

$$k_3 = \frac{\nu}{2\tau^2}(1+2\tau+\sqrt{1+4\tau}),\ k_4 = \frac{\nu}{2\tau^2}(1+2\tau-\sqrt{1+4\tau})$$

$$b_1 = -\frac{i\pi}{\sqrt{1-4\tau}},\ b_2 = -\frac{i\pi}{\sqrt{1-4\tau}},\ b_3 = \frac{i\pi}{\sqrt{1+4\tau}},\ b_4 = -\frac{i\pi}{\sqrt{1+4\tau}}$$

and the $\pm$ sign in the last term is taken positive when $j = 1,2$, and negative when $j = 3,4$;

and

$$G = \ln r - \ln r' + p.v.\int_0^\infty e^{k(z+\eta)}\left[C(k)e^{ik(x-\xi)} + B(k)e^{-ik(x-\xi)}\right]dk + \sum_{j=3}^{4} b_j e^{k_j(z+\eta)} e^{-ik_j(x-\xi)} \qquad (3\text{-}31)$$

when $\tau > \frac{1}{4}$, where

$$C(k) = \frac{\nu}{\tau^2 k^2 - \nu(1-2\tau)k + \nu^2}.$$

This indicates that there would be four waves of different wave number when $\tau < \frac{1}{4}$, two travelling before the foil and two behind; there are two waves propagating behind

the foil, when $\tau > \frac{1}{4}$. It is a critical point when $\tau = 1/4$. We also notice that when $\tau \to 0$, the wave radiation problem becomes the steady motion problem.

For the periodic motion, the pressure at the wake is obtained through the linear Bernoulli equation

$$p_{re} = i\omega\varphi_i - U\varphi_{ix} \tag{3-32}$$

which ignores the effect of the steady disturbed potential. As in Newman (1977), its continuity across the wake means that μ in Eq.(2-19) satisfies

$$i\omega\mu - U\mu_x = 0 \tag{3-33}$$

This gives

$$\mu(x) = \mu_0 e^{ik_w x} \tag{3-34}$$

where $k_w = \omega/U$, and the value of $\mu(\bar{x}_T)$ can be obtained from the difference between the potentials on the two elements attached to the trailing edge, as in the steady potential.

3.2.2 Numerical results on the radiation and diffraction forces

We shall first calculate the m_j terms. To obtain the m_j terms through Eqs.(3-27) & (3-28), there are a few steps to follow: (1) calculate the potential on the nodes of each element through fourth-order Lagrangian interpolation formula (see Abramowitz & Stegun, 1965, p878); (2) the tangential derivative $\bar{\phi}_s$ at the middle of the element is calculated through finite difference of the potentials at the nodes of the element. (3) $\bar{\phi}_x$ and $\bar{\phi}_z$ are obtained through the known $\bar{\phi}_s$ and $\bar{\phi}_n$ at the middle of the elements; (4) the values of $\bar{\phi}_x$ and $\bar{\phi}_z$ at the nodes of each element are again obtained through the fourth-order Lagrangian interpolation; (5) the m_j is then obtained at the middle of the

element through the finite difference of $\bar{\phi}_x$ and $\bar{\phi}_z$ at the nodes of each element.

To test the convergence of the above procedures, we calculate the m_j terms with 3 sets of meshes. Figure 3.6 shows that the present scheme can give very good results for these second derivatives. However, compared with the pressure in figure 3.2 and steady force in table 3.1, a finer mesh is needed to give converged results, especially at places where the curvature is high. We also notice that m_j is quite large especially near the leading edge. We further notice that n_j in Eq.(3-18) are the components of the normal and thus their magnitudes are always less than one. As a result, the second term could play an important role, which reflects the significance of the effect of the steady potential on the unsteady potential.

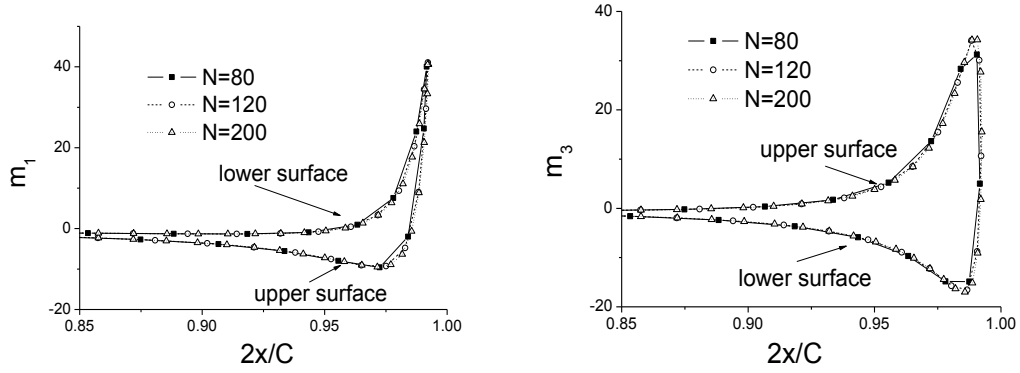

(a) (b)

Figure 3.6 m_j term for the symmetric Joukowsky foil with $t_{ck}/C = 11.78\%$, $h_T/C = 1.0$ at $Fn = 1.0$, $\beta = 5^0$ (a) m_1 (b) m_3

We consider the hydrofoil advancing in a regular wave and with small amplitude harmonic heave and pitch motions. Figure 3.7 gives the heave force and pitch moment on the symmetric Joukowsky foil of $t_{ck}/C = 11.78\%$, with Froude number $Fn = 0.6$ and submergence $h_T/C = 1.0$. The figure shows that the attack angle has significant effect

on the vertical force and rotational moment, especially at smaller νC. One of the reasons is that the mean position of the body changes when the attack angle changes. In this sense, the body becomes different. More importantly, the circulation around the foil changes as the attack angle changes. This will significantly affect the steady potential $\bar{\phi}$. As it has been seen in figure 3.6, the m_j term can be very large. When it varies, its effect on the radiation potential can be very significant, as can be seen in Eq.(3-18), especially at lower frequency. We notice in figure 3.7 that there is a sharp discontinuity at $\nu C \approx 0.17$. This in fact corresponds to $\tau \approx 0.25$. The data closest to this point used to plot these curves are at $\nu C = 0.168$ corresponding to $\tau = 0.246 < 0.25$ and $\nu C = 0.2$ corresponding to $\tau = 0.268 > 0.25$, respectively. The reason for the sharp variation at this point can be explained by the wave structure discussed after Eqs.(3-30) &(3-31). Further discussions could be found in the work of Grue & Palm (1985) and Wu & Eatock Taylor (1987). Figure 3.8 presents the force and moment of Joukowsky foil of $t_{ck}/C = 11.78\%$, with $\beta = 5^0$, $Fn = 0.6$ at different submergence h_T/C. The hydrodynamic force varies significantly when $\nu C > 0.2$ due to different submergence.

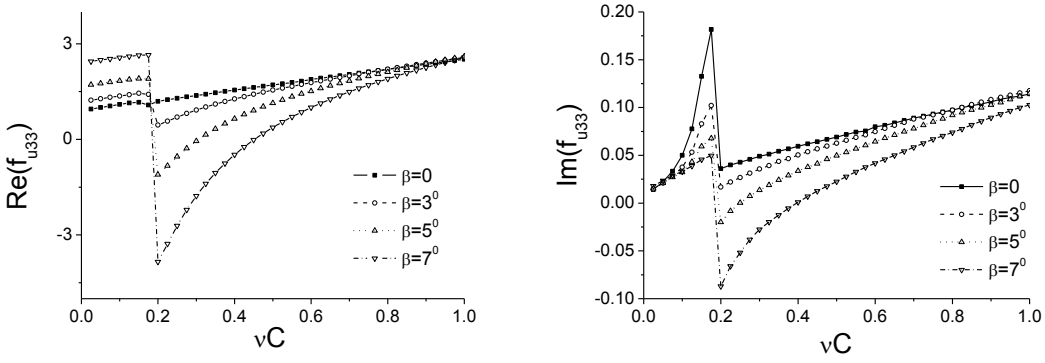

(a) (b)

Figure 3.7 to be continued on next page

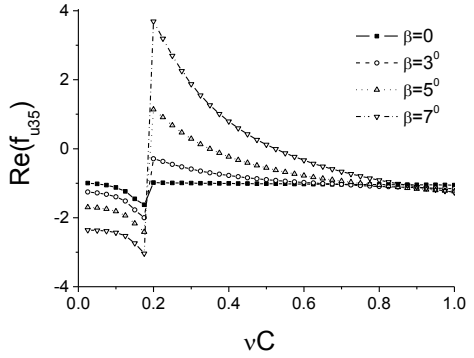

(c)

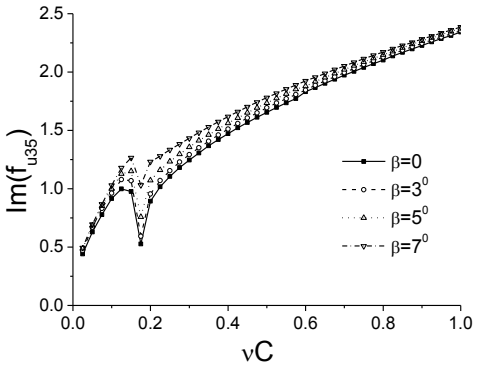

(d)

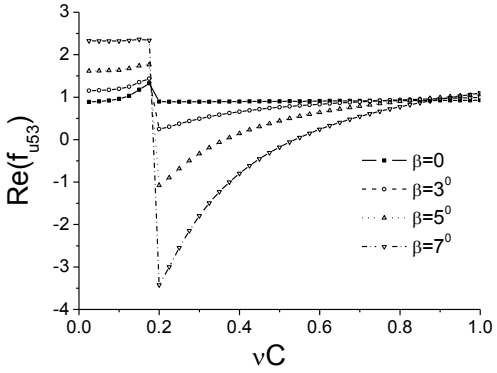

(e)

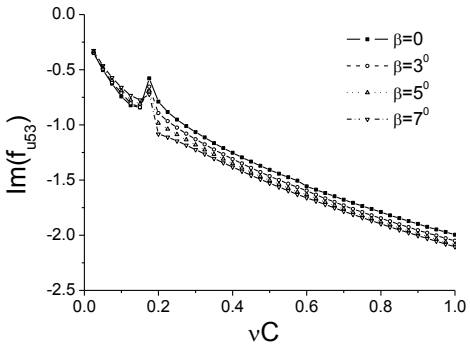

(f)

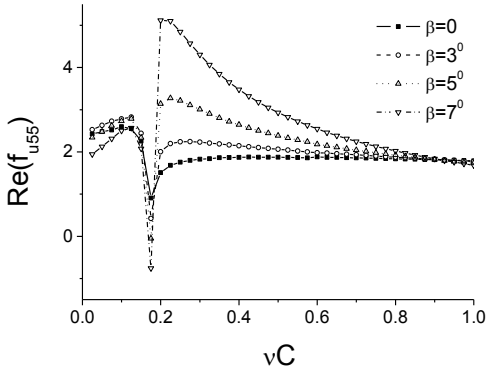

(g)

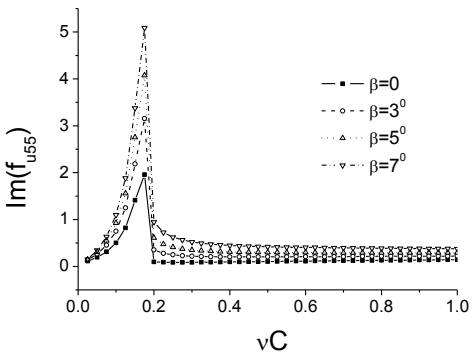

(h)

Figure 3.7 Hydrodynamic force on a symmetric Joukowsky foil with $t_{ck}/C = 11.78\%$, at

$$Fn = 0.6,\ h_T/C = 1.0$$

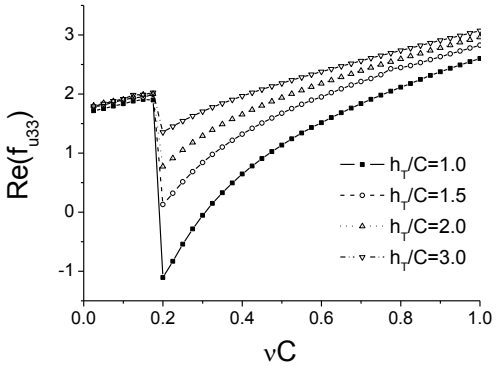

(a)

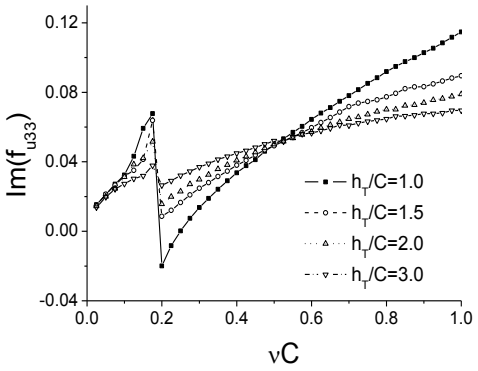

(b)

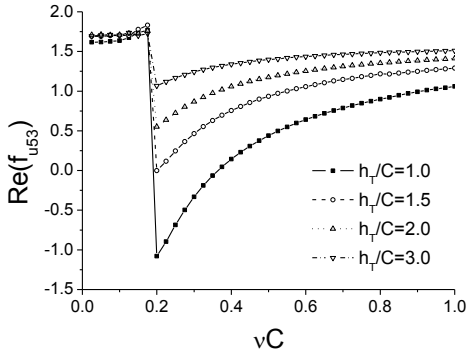

(c)

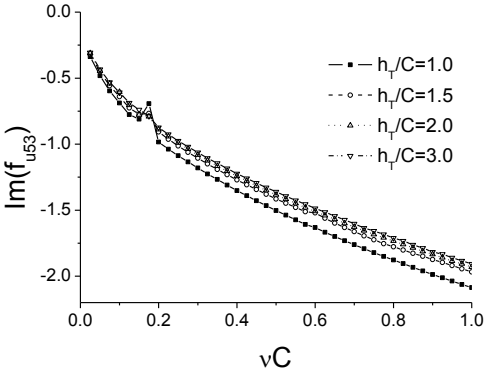

(d)

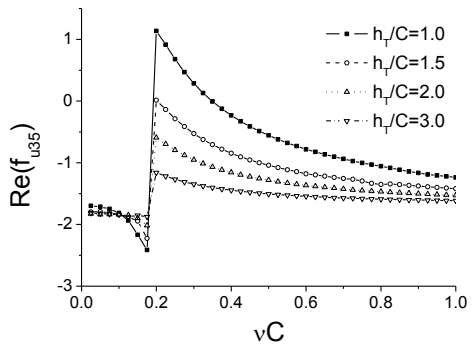

(e)

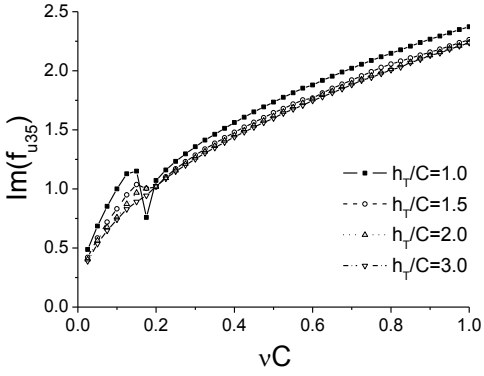

(f)

Figure 3.8 to be continued on next page

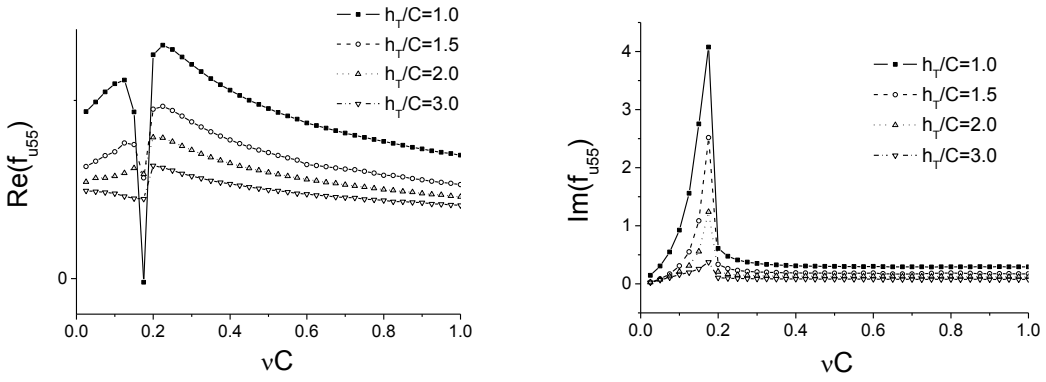

(g) (h)

Figure 3.8 Hydrodynamic force on a symmetric Joukowsky foil with $t_{ck}/C = 11.78\%$, at

$$Fn = 0.6,\ \beta = 5^0$$

For a submerged body, Timman & Newman (1962) have shown that the hydrodynamic forces associated with the wave radiation f_{uij} $(i, j = 1,3,5)$ satisfy

$$f_{uij}(U) = f_{uji}(-U) \tag{3-35}$$

which was further confirmed by Wu & Eatock Taylor (1990) at low forward speed. For a two dimensional body with fore/aft symmetry, Eq.(3-35) means that

$$f_{uij} = -f_{uji} \tag{3-36}$$

except that

$$f_{u15} = f_{u51} \tag{3-37}$$

due to anti-symmetry of the rotational motion when view from the fore/aft body.

It was, however, found by Wu & Eatock Taylor (1988) that this relationship is valid only at low forward speed. At large forward speed, Wu & Eatcok Taylor (1988) have shown that

$$\mathrm{Re}(f_{uij}) = \mathrm{Re}(f_{uji}),\ \mathrm{Im}(f_{uij}) = -\mathrm{Im}(f_{uji}) \tag{3-38}$$

which do not require the body to have fore/aft symmetry.

We consider an example at $\nu C = 2.012$ or $\omega = \pi$ and plot f_{uij} and f_{uji} against Froude number in figure 3.9. The data plot in figure 3.9 starts from $Fn = 0.25$ with an increment of 0.25. The results do not satisfy the Timman & Newman relation at low Froude number. This is in fact not a surprise, because the hydrofoil does not have fore/aft symmetry and because of the presence of the wake effect here. One can also see in the figure that Eq.(3-36) is not satisfied either in most cases. This is again due to the effect of the wake, as the relationship does not require fore/aft symmetry of the body. There are in fact further relationships to link these hydrodynamic forces with the radiated wave at infinity for a non-lifting body (Wu 1991b). However because of the wake effect, such a relationship may not be relevant here.

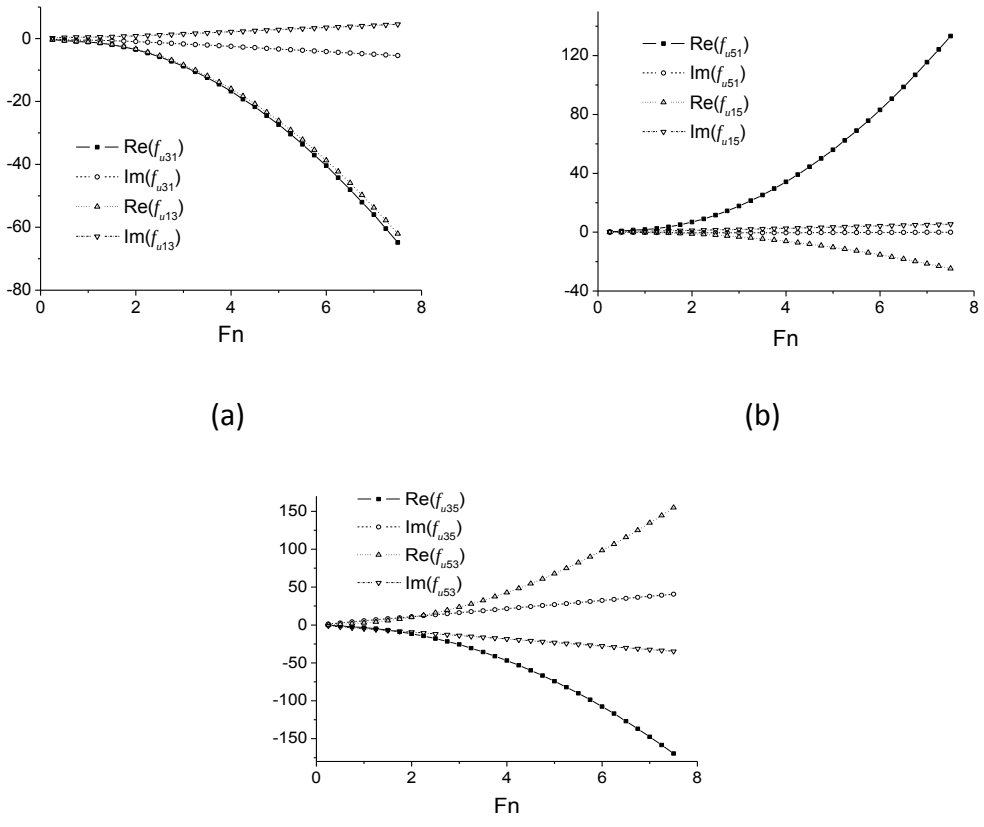

Figure 3.9 f_{uij} and f_{uji} of a symmetric Joukowsky foil with $t_{ck}/C = 11.78\%$, $\beta = 5^0$, $\nu C = 2.012$.

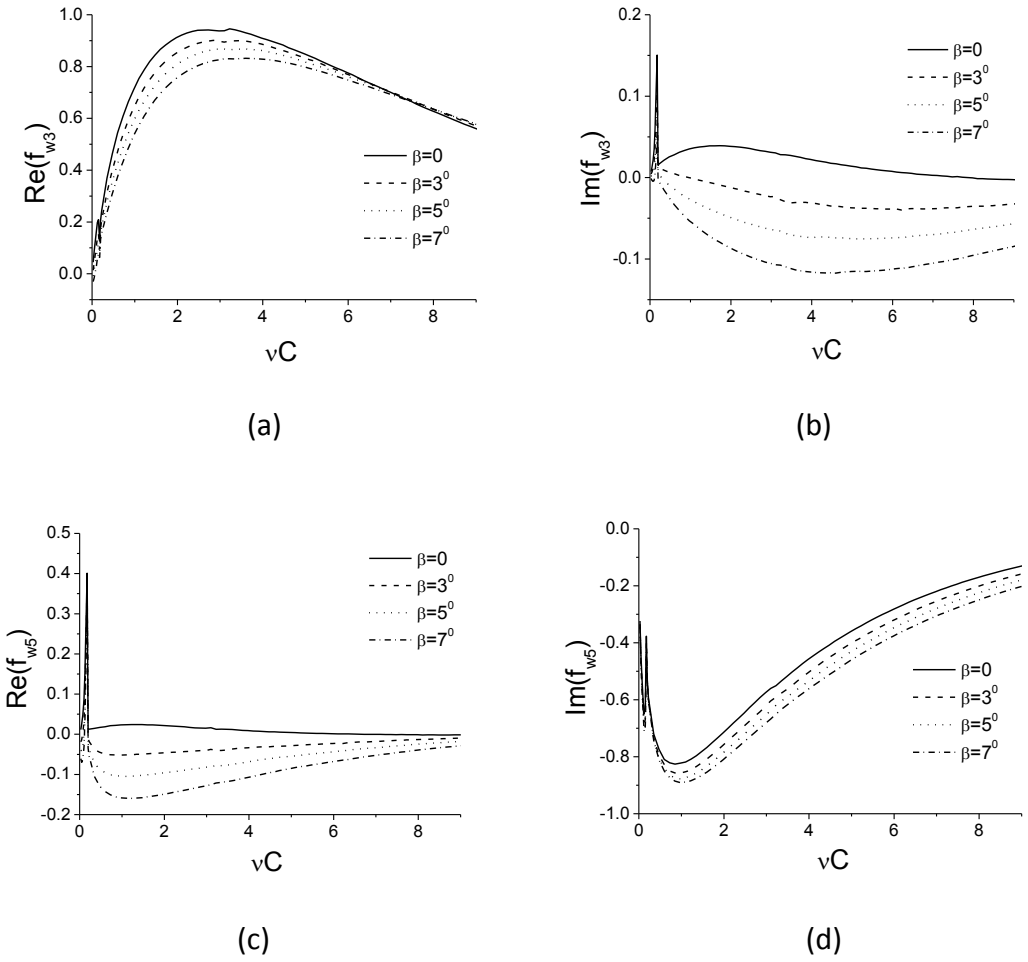

Figure 3.10 The hydrodynamic force due to the incident wave, with $Fn = 0.6$, $h_T / C = 1.0$, $t_{ck} / C = 11.78\%$, and $\varepsilon_w = 0$. (a)(b) vertical force and (c)(d) moment

Figure 3.10 presents the wave excitation force and moment due to incident potential and diffracted potential when the wave is from the right hand side, or the head sea. For the diffraction problems, there is also a relationship linking the force with the amplitude of the diffracted wave at infinity (Wu, 1991b) and a relationship linking the amplitudes of the reflected and transmitted waves themselves (Wu 1993). The wake here however has changed the validity of these relationships. In particular, for a non-lifting body the wave structure is that discussed after Eq.(3-31). For a hydrofoil in waves, however, because the vortex sheet in Eq.(3-34) extends to infinity, the waves

will become more complicated. The curves show the force, including contribution from both the incoming wave and diffracted wave. The differences due to the attack angle become significant when νC increases. These curves increase when νC becomes larger and then decrease after they reach their peaks. It is expected that these curves approaching zero when νC be very large because of the $e^{-k_0 h}$ term in the incident wave.

Chapter 4 Nonlinear vortex shedding of an oscillatory foil or plate in unbounded flow

4.1 Introduction

When the attack angle and/or the amplitude of oscillation becomes large, or there is oscillation without forward speed, the shed vortex can no longer be approximated using the flat vortex sheet behind the trailing edge. The vortices would tend to move out of the centre plane, and the flow near or behind the trailing edge would be affected. Figure 4.1 shows the snapshots of these kinds of vortices behind a foil. The non-linear vortex shedding of a foil or plate shall be investigated in this chapter.

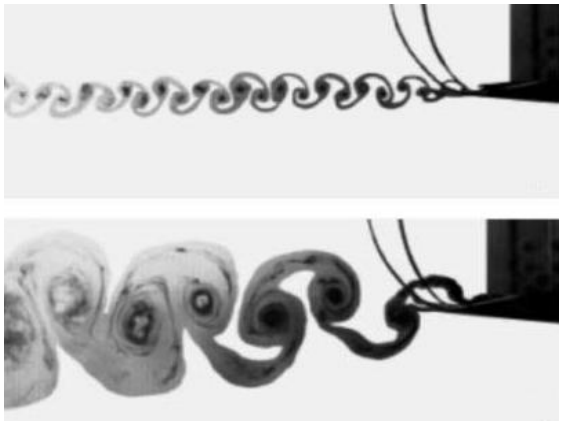

Figure 4.1 the visualization of vortex snapshots behind a foil (Lai *et al* 2002)

The nonlinear vortex shedding is prevailing in the scope of biomimetics. Swimming fish and flying birds are experts in fluid mechanics. Their tails or wings appear to be highly efficient. Man-made robots to fully mimic fast moving fish/cetaceans are still in progress. The manipulation of the shed vortices is a high technology and the motion of a flexible body has a great number of degrees of freedom. Review of oscillatory foil and biomimetic studies have been presented by Triantafyllou et al (2000, 2005). Among a large volume of theoretical and experimental studies, the foil is one of the most

popular geometries. For propulsive foils, Anderson et al (1998), Read et al (2003) presented their experimental data, and the thrust, input power and the efficiency of foil NACA0012 at various oscillatory frequencies was extensively investigated. High propulsive efficiency was observed in both works, although there were some differences in the exact results.

To simulate continuous vortex shedding, a numerical time stepping scheme is developed. The boundary element method through distribution of singularities over the body surface and over the vortex sheet is used. The unsteady Kutta condition is imposed at the trailing edge. The summation of tangential velocities on the upper and lower surfaces of the sharp edge of the foil equals the tangential derivative of the wake dipole attached to the trailing edge. The boundary integral equation is solved through linear elements on the body surface and on the newly shed vortex dipole element, together with point vortex in the wake which is tracked as part of the solution.

The numerical method is verified through a convergence study. Extensive simulations are made for the foil NACA0012. The results are first compared for the lifting force with the experimental data for the steady motion of the foil at various Reynolds numbers. Further comparison is made for the propulsive mode of the foil with the experimental data presented by Triantafyllou et al (2005). After these verifications, simulations are carried out to investigate the motion modes for propulsion/swimming, energy harvesting and flying. For propulsion and flying, the foil advances with constant forwards speed; while for energy harvesting, a foil with zero forward speed in current is studied. The kinematic energy of the flow is extracted by manipulating the motion of the foil. The effects of oscillatory frequency, effective attack angle, vertical motion amplitude, and phase difference of the motions on the performance of propulsive

efficiency or power coefficient are analysed.

When the foil thickness approaches zero, the implementation of this form of the integral equation becomes difficult. The body is then replaced by a plate. The numerical vortex shedding scheme is applied with minor changes. The unsteady Kutta condition is implemented by the continuous distribution of dipoles. The boundary integral equation is solved based on the non-penetration condition and the linear vortex element is used. The steady and unsteady oscillatory motion is studied. The numerical scheme is further applied to study the vortex shedding of a compartment with a bottom orifice. The damping effect due to the vortices is analysed.

4.2 The nonlinear vortex shedding of a foil

4.2.1 Description of numerical scheme

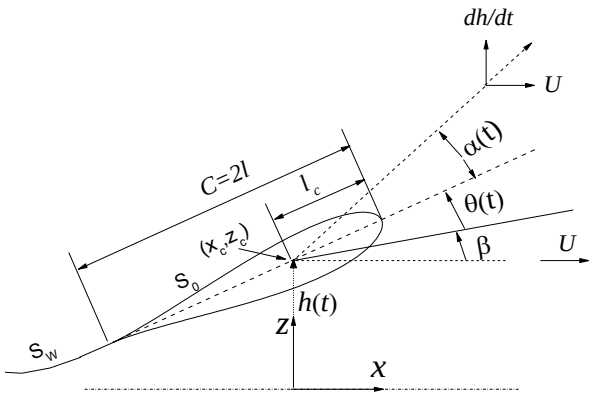

Figure 4.2 The sketch of the problem, vertical and rotational motion of a foil

We consider a foil moving forward at translational speed U or in the uniform coming flow with harmonic vertical and rotational motions with their motion amplitudes h_0 and θ_0 respectively. They are referred to heave and pitch motions, respectively, in

some publications. We do not adopt the terms here to avoid the confusions with the terms used in naval architecture. The Cartesian coordinate system oxz, as shown in figure 4.2, originates at the mean position of the rotation centre. The governing equations and the boundary conditions are the same as those in chapter 2. The perturbed potential ϕ satisfies the Laplace equation; the body surface condition on S_0 is the same as that in Eq.(2-5), and $\dot{A}_3$, $\dot{A}_5$ in Eq(2-5) shall be replaced by $\dot{h}$, $\dot{\theta}$, we have

$$\frac{\partial \phi}{\partial n} = (U - \dot{\theta} Z) n_x + (\dot{h} + \dot{\theta} X) n_z \tag{4-1}$$

on the body surface S_0, the dot over θ, h means the time derivative, and $X = (x - x_c)$, $Z = (z - z_c)$ with $l_c / C = 1/3$ for the cases in this chapter, l_c is denoted as the distance from leading edge to $(x_c,\ z_c)$.

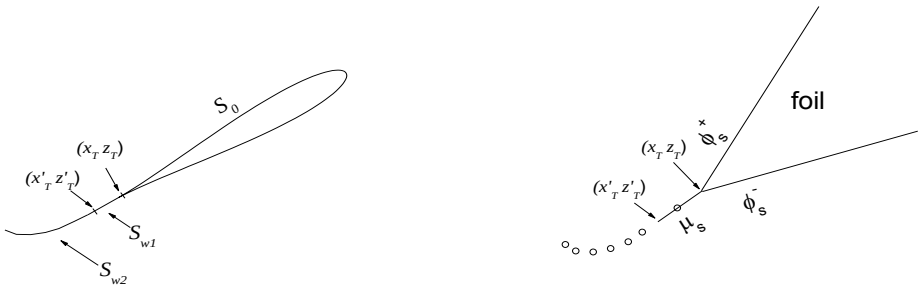

(a) (b)

Figure 4.3 Illustration of vortex wake at the trailing edge (a) shed vortex and (b) Kutta condition

Vortices will be shed from the trailing edge to form a wake sheet. For a linearized problem, it is usually assumed that the shape of the wake is a straight line in the

direction of incoming flow behind the trailing edge. When the attack angle and/or amplitude motion becomes larger, the shape and location of the wake will be part of the solution, which becomes one of the main challenges in the present work. As shown in Fig.(4.3a), the element in the wake attached to the trailing edge is denoted as S_{w1}, where the Kutta condition and vortex shedding scheme will be imposed, and the rest of the wake is denoted as S_{w2}.

To improve the computational performance, the differential Eq.(2-23) can be modified. We notice that

$$\frac{\partial G(p,q)}{\partial n} = \frac{\partial H(p,q)}{\partial s} \tag{4-2}$$

where $H(p,q) = \arctan\frac{x-\xi}{z-\eta}$, $\vec{s} = (s_x, s_z)$ is the tangential vector along the integral boundary, and when one walks along the $\vec{s}$ direction, $\vec{n}$ points to the right hand side. It is common that when there is a discontinuity between tangential velocities across a sheet, their difference is defined as vorticity γ. As a result, from Eq.(2-20) we have

$$\frac{\partial \mu}{\partial s} = \gamma \tag{4-3}$$

Substituting Eqs.(4-2) & (4-3) into Eq.(2-23) and using integration by parts over S_{w2}, we have

$$\begin{aligned} 2\pi\phi(p) &= \int_{S_0} [\frac{\partial G(p,q)}{\partial n_q}\phi(q) - G(p,q)\frac{\partial \phi(q)}{\partial n_q}]dS \\ &+ \int_{S_{w1}} \frac{\partial G(p,q)}{\partial n_w}\mu(q)\ dS + \mu(\vec{x}'_T)H(p,\vec{x}'_T) + \int_{S_{w2}} H(p,q)\gamma(q)\ dS \end{aligned} \tag{4-4}$$

where $\vec{x}_T = (x_T, z_T)$ is the starting point of the S_{w1}, or the trailing edge and $\vec{x}'_T = (x'_T, z'_T)$ is the finishing point of S_{w1}, as shown in Fig.4.3(a). It should be noticed that the fact that the dipole strength is zero at the end of the wake has been used in

Eq.(4-4).

We then discretize the integral boundary. The foil surface is divided into N elements, and in the wake there are one dipole element S_{w1} and m vortex elements at $(m+1)th$ time step. We have

$$2\pi\phi(p)=\sum_{k=1}^{N}\int_{S_k}[\frac{\partial G(p,q)}{\partial n_q}\phi(q)-G(p,q)\frac{\partial\phi(q)}{\partial n_q}]dS$$
$$+\int_{S_{w1}}\frac{\partial G(p,q)}{\partial n_w}\mu(q)\ dS+\mu(\vec{x}'_T)H(p,\vec{x}'_T)+\sum_{j=1}^{m}\int_{S_{wj}}H(p,q)\gamma(q)\ dS \tag{4-5}$$

For a non-lifting body, the boundary integral equation in Eq.(4-5) will have the term over the body surface only. The existence of the wake distinguishes a foil from a smooth body and therefore presents the major computational challenges. The choice of a right scheme for the vortex shed from the trailing edge, the suitable form of the Kutta condition and the appropriate method to track the wake are essential components in a successful solution technique. We may use linear distribution of ϕ over the body surface. At $t=0$, we impose the body surface boundary condition at the nodes of the each element on the body. Since no circulation has yet developed around the foil, Eq.(4-4) can be solved without the wake and $\phi^{+}=\phi^{-}$ is used at the trailing edge. At the next time step $t=dt$, S_{w1} will be formed and $\vec{x}'_T=(x'_T,z'_T)$ is obtained from

$$x'_T=x_T+(-U+\bar{u}_{\vec{x}_T})dt \tag{4-6}$$

$$z'_T=z_T+\bar{w}_{\vec{x}_T}dt \tag{4-7}$$

where $\bar{u}_{\vec{x}_T}$ and $\bar{w}_{\vec{x}_T}$ are the average horizontal and vertical velocities obtained by ϕ, when approaching the trailing edge from the upper and lower sides of the foil. From the continuity of the pressure p_{re} across S_{w1}, or $p_{re}{}^{+}=p_{re}{}^{-}$, we shall have

$$\frac{\overline{D}\mu}{\overline{D}t} = 0 \text{ or } \frac{d\mu}{dt} - U_{s_T}\frac{\partial \mu}{\partial s} = 0 \tag{4-8}$$

where $U_{s_T} = (-U + \overline{u}_{\vec{x}_T},\ \overline{w}_{\vec{x}_T})$. In the discretised form, this can be written as

$$\mu(\vec{x}'_T, t+dt) = \mu(\vec{x}_T, t) \tag{4-9}$$

which means the dipole strength at $\vec{x}'_T = (x'_T, z'_T)$ can be obtained from the dipole strength at $\vec{x}_T = (x_T, z_T)$ at the previous time step. However, at $t = dt$, $\phi^+ \neq \phi^-$ at the trailing edge and therefore $\mu(\vec{x}_T, t+dt)$ in Eq.(4-5) is unknown although $\mu(\vec{x}'_T, t+dt)$ is known from Eq.(4-9), and there is still no S_{w2} at this stage. This means that when we impose the body surface boundary condition at element nodes, there will be one equation short. This shortfall is met by the Kutta condition at the trailing edge in the following form

$$\left.\frac{\partial \phi^+}{\partial s}\right|_{\vec{x}_T} - \left.\frac{\partial \phi^-}{\partial s}\right|_{\vec{x}_T} = \left.\frac{\partial \mu}{\partial s}\right|_{\vec{x}_T} \tag{4-10}$$

where $\left.\frac{\partial \phi^+}{\partial s}\right|_{\vec{x}_T}$, $\left.\frac{\partial \phi^-}{\partial s}\right|_{\vec{x}_T}$, $\left.\frac{\partial \mu}{\partial s}\right|_{\vec{x}_T}$ denote the tangential derivatives based on the definition of the direction of $\vec{s}$ after Eq.(4-2).

We then have the right number of equations for the unknowns in Eq.(4-4) which can now be solved. At the next time, the dipole in S_{w1} moves downstream and the first element in S_{w2} will be formed. The strength of the vortex in this element can be obtained from

$$\frac{\overline{D}\gamma}{\overline{D}t} = 0 \tag{4-11}$$

in the Lagrangian sense. This means that the vortex strength in the first element at this time step can be obtained from its strength in S_{w1} at the previous time step, which is

in fact $\frac{\partial \mu}{\partial s}$ and is therefore known. In particular, we shall use point vortex κ_1 to replace the distributed γ in the element. Its total strength will be clearly the integration of $\frac{\partial \mu}{\partial s}$ over S_{w1} at the previous time step, or

$$\Gamma_1(t+dt) = \mu(\vec{x}_T, t) - \mu(\vec{x}'_T, t) \tag{4-12}$$

The position of Γ_1 can be obtained by following the movement of the fluid particle at middle of S_{w1} at time t to its new location at $t+dt$ using the average velocity on both sides of S_{w1}. Eq.(4-5) can then be solved again. In the next time step, the strength Γ_1 will not change and its position can be obtained by following the fluid particle in the Lagrangian sense. A new point vortex κ_2 formed from S_{w1} will be obtained. S_{w1} will be updated using Eqs.(4-6) & (4-7) and Kutta condition will be imposed through Eq.(4-10). In the following steps, the above procedure can be repeated and the position of Γ_i $i = 1,2,3...m$ can be updated using the Lagrangian method. The calculation can continue until the desired time step. The vortex wake S_{w1} is like the tail of the foil, and there will be a newly shed point vortex behind the trailing edge at each time step. The vortex shedding scheme is an 'egg-laying' procedure.

The force and moment on the foil can be obtained through the integration of pressure, which is calculated using Bernoulli equation, or

$$p_{re} = -\rho[\frac{D\phi}{Dt} - (U - \dot{\theta}Z, \dot{h} + \dot{\theta}X) \cdot \nabla\phi + \frac{1}{2}\nabla\phi\nabla\phi] \tag{4-13}$$

where $\frac{D}{Dt}$ is the derivative with respect to time for a point fixed on the body. Consequently, the horizontal, vertical force and moment can be obtained through pressure integration in Eq.(2-16). We have

$$F_j = \int_{S_0} p_{re} n_j dS = -\rho \int_{S_0} [\frac{D\phi}{Dt} - (U - \dot{\theta}Z, \dot{h} + \dot{\theta}X) \cdot \nabla\phi + \frac{1}{2}\nabla\phi\nabla\phi] n_j dS \text{ , } j = 1,\ 3,\ 5 \qquad (4\text{-}14)$$

4.2.2 Numerical results of different motion modes

4.2.2.1 Steady motion of a foil

We first consider the foil at steady forward motion only. In this case, it is possible that one could introduce

$$\phi = UC\varphi \qquad (4\text{-}15)$$

Boundary conditions can then be applied to φ together with the treatment at the trailing edge. The forward speed U has no explicit effect on the non-dimensional results. This means that when the problem is solved using ϕ, the results normalized by U should be independent of forward speed. To investigate the convergence of the results with respect to time step, we use $dt = \lambda_1 C / U_{S_T}$, where U_{S_T} is the shedding velocity of the vortex elements attached to the trailing edge, λ_1 is a parameter that can be chosen from 0.01-0.05 and a variable time step has been used. In the case of every U_{S_T}, a large value of allowed dt can also be specified. For periodic motion, the time step $dt < \lambda_2 T$ is also required, where parameter λ_2 shall be chosen smaller than 0.02. We consider a case in which the foil starts moving at a given forward speed suddenly with 5^0 angle of attack. Foil NACA 0012 is used as an example to study the vortex shedding problem. Figure 4.4 presents the lifting force. The results from different time steps agree well and there is no graphically visible difference in the curves. Here we have to state that all the force history curves have a very big value at the first and/or second time step, the spike of the curve has been ignored here and throughout the thesis.

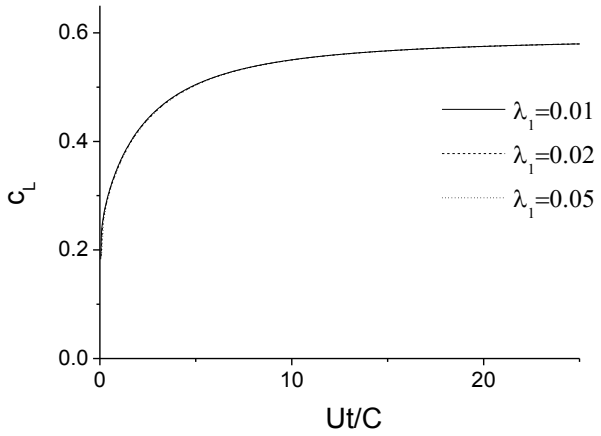

Figure 4.4 The lifting force history of NACA0012 foil with an impulsive constant motion at $\beta = 5^0$

To validate the present results, comparison is made with the experimental data. In figure 4.5, the calculated lifting force is taken at the time when the foil has travelled a distance equal to 50 chords. The experimental data is taken from Sheldahl et al (1981). The experiment was conducted in the Walter H. Beech Memorial Wind Tunnel, Wichita State University. The wind tunnel has a 2.13mx3.05m test section fitted with floor to ceiling two-dimensional inserts for testing two-dimensional airfoil sections. A balance system is used to obtain the lift, drag and moment data. All the data were corrected for wake and solid blockage, buoyancy, upwash and wind tunnel factor. The published data can be used for the comparison of present study. As shown in the figure, the agreement is quite good when the attack angle is small. Discrepancy appears as the attack angle increases. However, the discrepancy at higher Reynolds number is reduced due to the reduced flow separation.

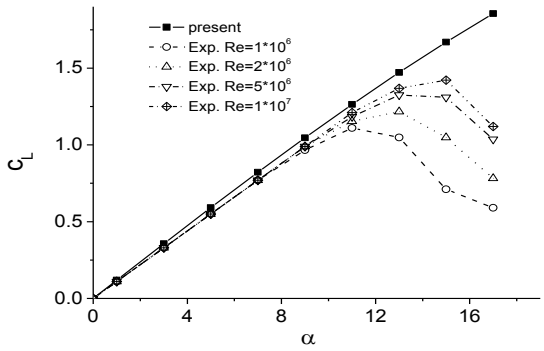

Figure 4.5 The lifting force of NACA0012 foil with various attack angle at $Ut/C = 50$.

4.2.2.2 Propulsion / swimming mode

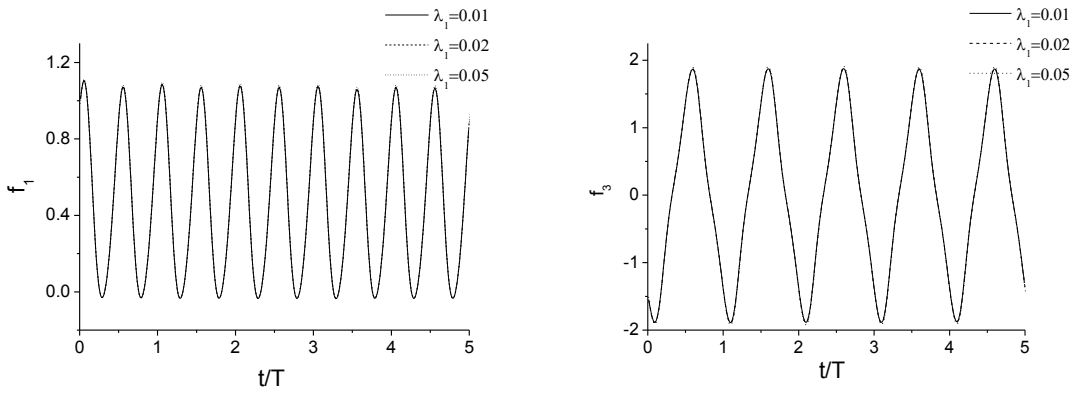

(a) (b)

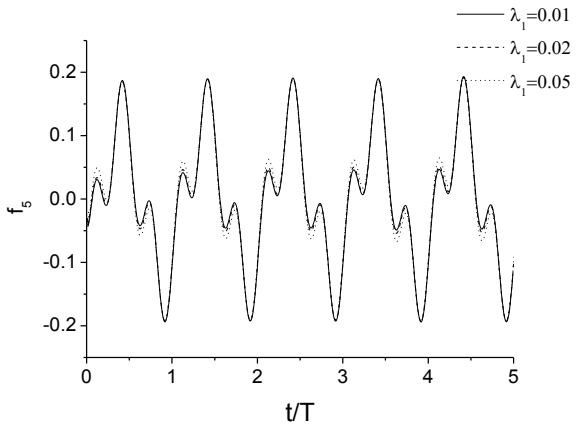

(c)

Figure 4.6 The forces history under $St = 0.3$ $h_0/C = 0.75$, $\alpha_0 = 15^0$, $\varepsilon = 90^0$

It has been found that generally, when ε is close to 90^0, an oscillatory foil can produce thrust when $\arctan\frac{\omega h_0}{U} > \theta_0$, or $\alpha_0 > 0$ (Anderson et al 1998). We shall use the present methodology to investigate such a case. Convergence study on the oscillatory motion has been carried out similar to that for the case of steady forward speed; the forces history are in good agreement when $\lambda_1 = 0.01$, $\lambda_1 = 0.02$, $\lambda_1 = 0.05$ are used for $dt = \lambda_1 C/U_{S0}$, as shown in figure 4.6. In the figure, we can observe that the thrust is always above the zero line. It is interesting to see that the period of the thrust is half of the motion period or it has two cycles for each oscillation period; while the periods of vertical force and rotational moment are the same as that of motion. This is in fact similar to the behaviour of the force on a floating body undergoing periodic horizontal oscillation perpendicular to its vertical symmetry plane (Wu 1994, 2000). As the foil is symmetric and in the periodic motion, the body and flow pattern at t and $t+T/2$ form the mirror images about $z=0$. Using this fact and following the procedures of Wu (1994, 2000), it can be shown that the force in the x direction will have only components of frequencies $2n\omega$, $n = 0, 1, 2\ldots$ and the force in the z direction and rotational moment have only components of $(2n+1)\omega$. This is what is reflected in Fig.4.6.

If we use the definition in Eq.(4-15) again, the boundary condition in Eq.(4-1) in the non-dimensional coordinate system $(\hat{x}, \hat{z}) = (x, z)/C$ becomes

$$\frac{\partial \varphi}{\partial n} = [1 - \hat{Z}B\cos(\frac{2\pi t}{T} + \varepsilon)]n_x + [D\cos\frac{2\pi t}{T} + \hat{X}B\cos(\frac{2\pi t}{T} + \varepsilon)]n_z \qquad (4\text{-}16)$$

where

$$B = \frac{C\omega\theta_0}{U} = \frac{\pi CSt}{h_0}[\alpha_0 - \arctan(\pi St)]$$

$D = \pi St$

This shows that in addition to St, the results normalised by U will depend on the vertical amplitude h_0 / C, nominal maximum effective attack angle α_0 and phase difference of vertical and rotational motion ε. Their effects are now investigated.

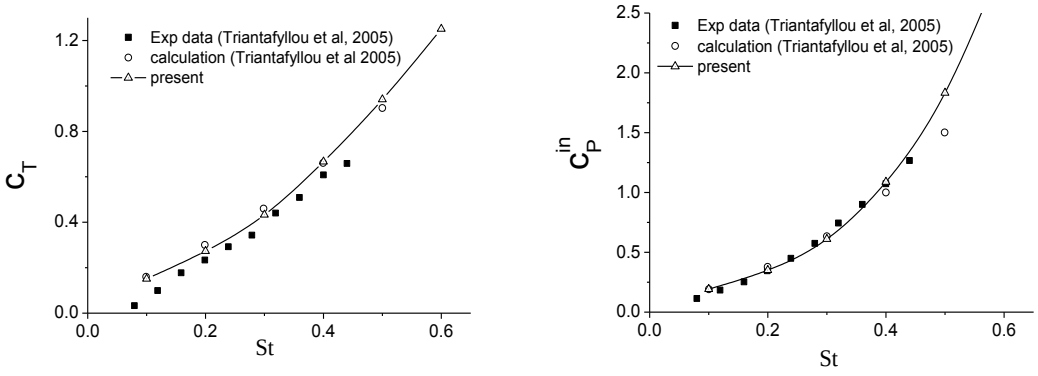

(a) (b)

Figure 4.7 (a) Thrust coefficient c_T , (b) input power coefficient c_P^{in} with $h_0 / C = 0.75$, $\alpha_0 = 15^0$, $\varepsilon = 90^0$ at various St.

We consider the foil motion with $h_0 / C = 0.75$, $\alpha_0 = 15^0$, $\varepsilon = 90^0$ at various St. As shown in figure 4.7, the present results agree well with the experimental data and the nonlinear numerical solution presented by Triantafyllou et al (2005), which is obtained using a complex potential method. The experiment was carried out by Anderson et al (1998) at MIT tank; the data was obtained from a NACA0012 foil with 10cm chord and 60cm span. The submergence of the foil is 60cm. Since the side plate had been used and the chord-span-ratio and chord-submergence-ratio are as large as 6, the three-dimensional effect and free surface effect would be insignificant. As St increases, thrust coefficient c_T and the input power c_P^{in} increase rapidly. However, we can see that the thrust curves from the calculation are slightly higher than the experimental data in figure 4.7(a). As commented by Triantafyllou et al (2005), this might be due to

the frictional resistance, which would be 0.05 approximately. We notice that the discrepancy is larger when St is near 0.1. A leading edge vortex shedding (LEV) might appear and a larger discrepancy between experimental data and inviscid flow theory results can be observed at lower St. When St becomes larger, the oscillatory frequency increases, and the LEV would be reduced or eliminated (Maresca et al 1979, Ellington 1984, Ellington et al 1996, and Dickinson et al, 1999). However, as St keeps increasing, for example when $St > 0.4$, the maximum of the varying attack angle $\alpha(t)$ can be very large and excessively large attack angles may cause LEV (Pan et al 2012) or 'stall' phenomena. As a result, larger discrepancy of c_T can be found when $St > 0.4$.

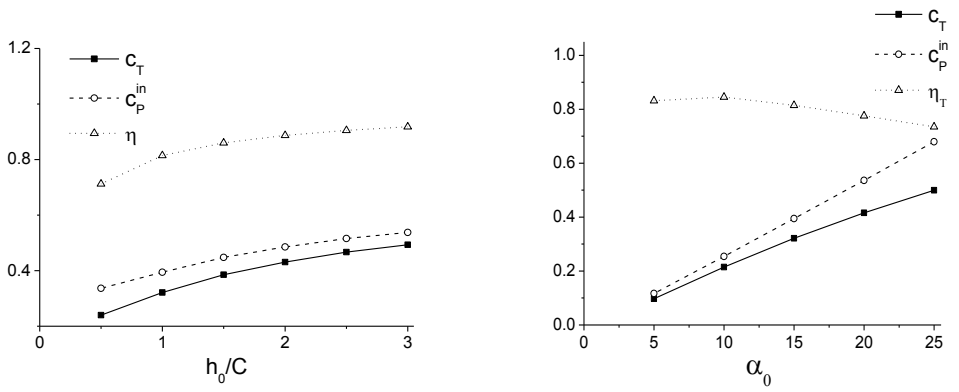

(a) (b)

Figure 4.8 The effects of (a) heave amplitude h_0/C at $St = 0.2$, $\alpha_0 = 15^0$, $\varepsilon = 90^0$ and (b) nominal maximum attack angle α_0, at $St = 0.2$, $h_0/C = 1.0$, $\varepsilon = 90^0$.

Figure 4.8(a) presents the effect of vertical motion amplitude h_0/C on the propulsive foil at $St = 0.2$, $\alpha_0 = 15^0$, $\varepsilon = 90^0$. The data in the figure show that the thrust, input power and propulsion efficiency all increase with the vertical motion amplitude. The effect of nominal maximum effective attack angle α_0 is shown in figure 4.8(b), at $St = 0.2$, $h_0/C = 1.0$, $\varepsilon = 90^0$. When α_0 increases, both the thrust and input

power increase rapidly; but the rate of input power increase is higher than the propulsion power. As a result, the efficiency decreases.

We further study the effect of the phase difference of the vertical and rotational motion on the thrust and propulsive efficiency. From their experimental data, Anderson et al (1998) stated that the highest efficiency can be achieved when ε is around 70^0, while Read et al (2003) reported that the highest efficiency is found when ε is around 110^0. The experiments were carried out by Anderson et al (1998) and Read et al (2003) using the same equipment. However, it is really unusual that their data are different. Here we simulate the specific oscillatory motion with $St = 0.22$, $h/C = 0.75$, $\alpha_0 = 15^0$, which are the same as one set of data in their experiment. ε varies from 45^0 to 135^0. The thrust coefficient, power coefficient and the propulsive efficiency are presented in figure 4.9. We notice that the lowest thrust coefficient c_T and power coefficient c_P^{in} are achieved when $\varepsilon \approx 75^0$, and the highest propulsive efficiency appears when $\varepsilon \approx 70^0$. The numerical results of present simulation support the data of Anderson et al (1998).

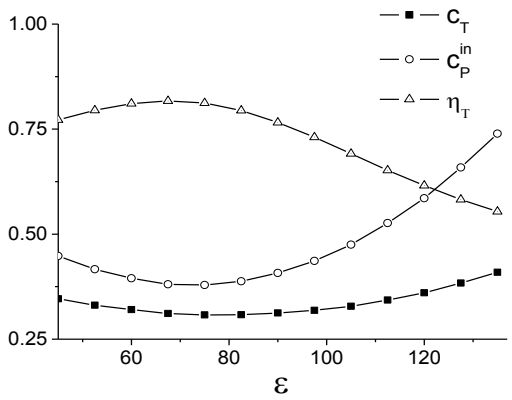

Figure 4.9 The effect of the phase difference between vertical and rotational motions, with $St = 0.22$, $h_0/C = 0.75$, $\alpha_0 = 15^0$

4.2.2.3 Energy harvesting mode

When the foil has no forward speed but in a uniform incoming flow, the foil can absorb energy from the current through its vertical and/or rotational motion. This is usually defined as energy harvesting mode and can be achieved if the oscillatory motion of a foil is adjusted properly. The foil in a current with velocity $-U$ is equivalent to the foil with forward speed U . Therefore the boundary conditions and the vortex shedding scheme are the same. In fact it has been found from the extensive simulations that the vertical motion is likely to become energy harvesting mode when $\alpha_0 < 0$ and $\varepsilon \approx 90^0$.

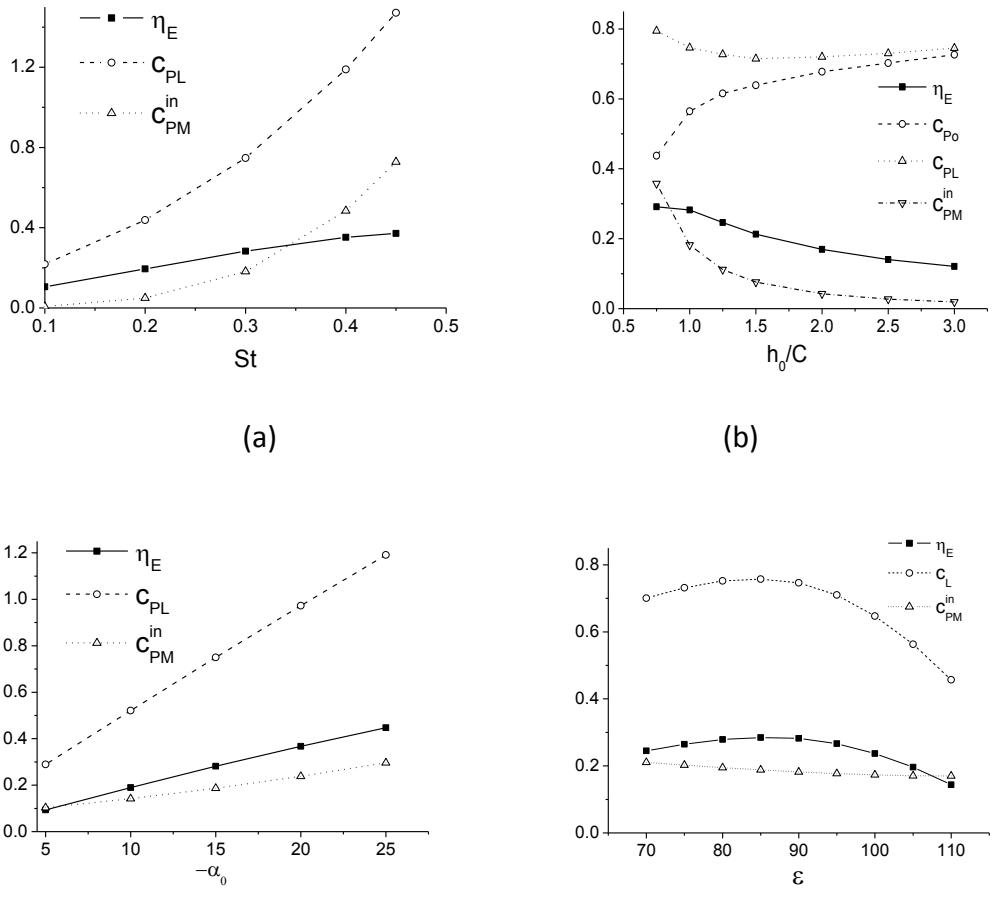

Figure 4.10 Effects of (a) St (b) h_0 / C, (c) α_0 and (d) ε

Here the effects of St, h_0/C, α_0, ε on the performance of an oscillatory foil are investigated, which are given in figures 4.10 (a) (b) (c) & (d) respectively. When one parameter varies in each of these figures, the other three will be fixed at $St=0.3$, $h_0/C=1.0$, $\alpha_0=-15^0$, $\varepsilon=90^0$. As can been seen in figure 4.10(a), the power coefficient c_{PL} due to vertical motion and the input power c_{PM}^{in} due to rotational motion are both positive and increase with St. The total power coefficient can be obtained as $c_{PO}=c_{PL}-c_{PM}^{in}$. Here we adopt the assumption that the total fluid energy which can be absorbed is within the span of the vertical motion at the rotation centre, which differs from that based on the motion amplitude of the leading or trailing edge. Thus we have the fluid energy as $\frac{1}{2}\rho(2Uh_0)U^2=\rho U^3h_0$ and the harvest energy efficiency can be written as $\eta_E=\frac{P}{\rho U^3h_0}=c_{PO}\frac{C}{h_0}$. We notice that η_E is proportional to c_{PO} .for fixed C/h_0, and for this reason the curve for c_{PO} is not presented in figures 4.10(a) (c) & (d) but only in figure 4.10(b) where h_0/C varies. As can been seen in figure 4.10(a), η_E increases with St within the region given. Figure 4.10(b) shows that the net power coefficient c_{PO} increases with h_0/C. This is because although the reduction of power coefficient c_{PL} can be observed at smaller St, the input power coefficient c_{PM}^{in} decreases more rapidly. The power coefficient c_{PO} of an oscillatory foil increases with h_0/C but the power efficiency η_E, which is normalized by vertical motion amplitude, decreases. Figure 4.10(c) shows an almost linear increase of c_{PL}, c_{PM}^{in} and η_E with α_0. A higher increase rate of c_{PL} can be observed, and thus results in the increase of η_E. Figure 4.10(d) gives results for ε varying from $70^0\sim110^0$. It can be seen that the

highest value of η_E is achieved when $\varepsilon \approx 90^0$.

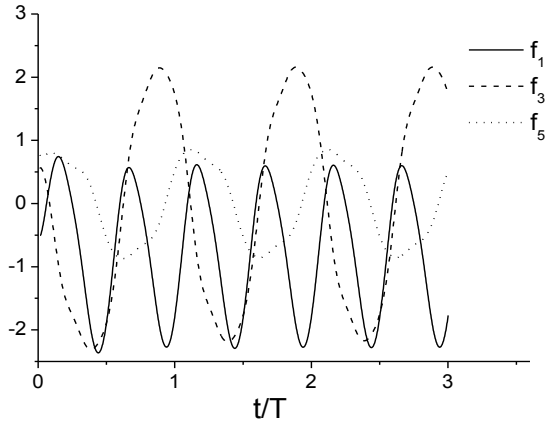

Figure 4.11 Force history with $St = 0.3, h_0 / C = 1.0$, $\alpha_0 = -15^0, \varepsilon = 90^0$

Figure 4.11 further presents the force history for the case at $St = 0.3$. Similar to figure 4.6, the frequency of the horizontal force is double that of motion. In this case however, the most part of the horizontal force is below the zero line, which means that the force is a drag. It suggests that the foil is no longer in the propulsive mode. Since the drag is produced in the energy harvesting mode, it can also be called the braking mode when in comparison of the propulsion mode.

4.2.2.4 Flying mode

One major difference between a flying bird and swimming fish is that the former needs constant lifting force to support its weight while fishes can balance themselves principally with the help of their buoyancy. A flying mode is therefore defined as the motion which will create lifting force and propulsive force. For an oscillatory foil it is observed that with a mean upward attack angle or a biased rotational angle, it will normally be in a flying mode. We investigate this mode under $h_0 / C = 0.75$, $\alpha_0 = 10^0$, $\varepsilon = \pi / 2$. The results are provided in figure 4.12. It can be seen in Figs.4.12(a) (c) & (d)

that results for the thrust, input power coefficient and propulsive efficiency from the two cases of $\beta = 5^0$ and $\beta = 10^0$ are close to each other, although the former is slightly higher than the latter. However, the lifting force almost doubled when the bias angle doubled for same St, as shown in figure 4.12(b). It suggests that there is a linear relationship between mean lifting force and β, as in the case of pure steady motion at small attack angle. The average lifting forces for zero mean attack angle in figures 4.6 & 4.11 are expected to be zero, while for biased rotational motion, apart from increasing β, higher lifting force can also be obtained by increasing St as expected.

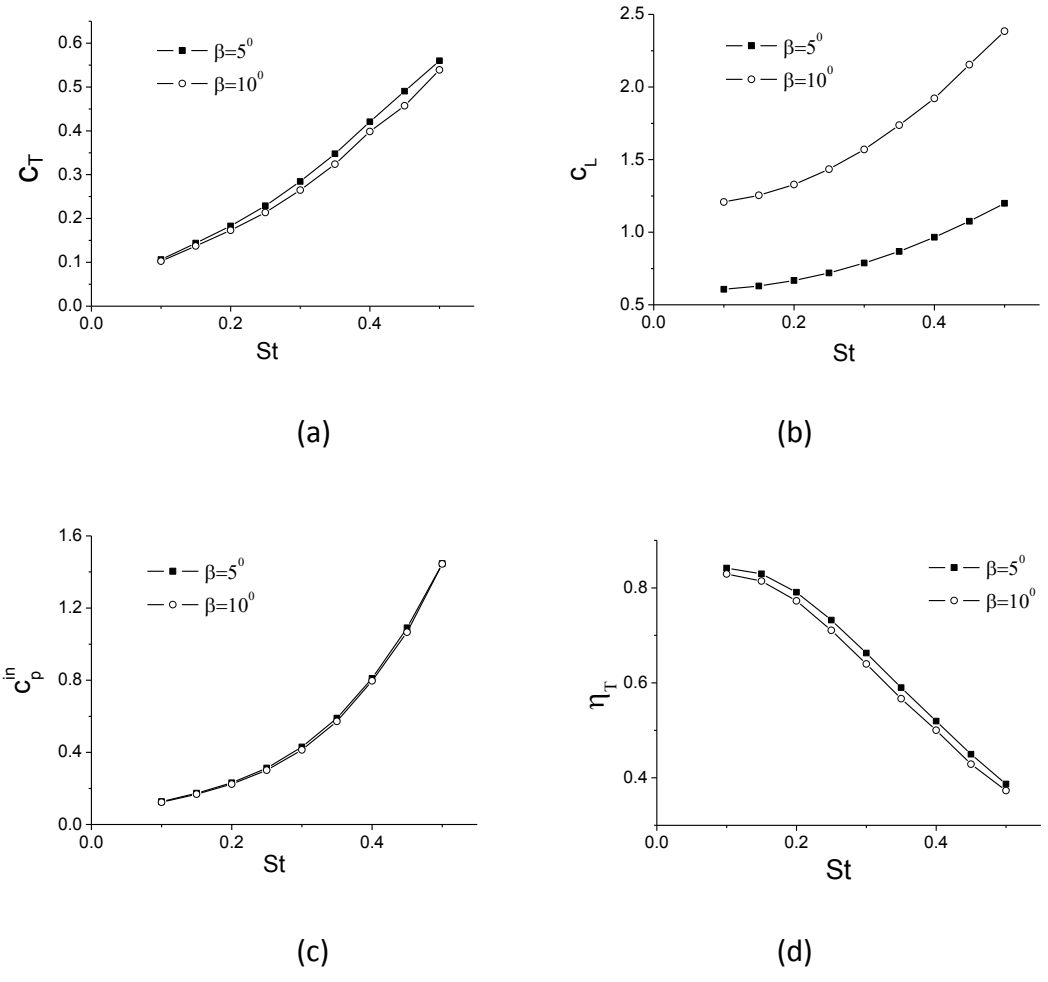

Figure 4.12 the performance with $h_0 / C = 0.75$, $\alpha_0 = 10^0$, $\varepsilon = 90^0$. (a) thrust (b) lifting force (c) input power (d) propulsive efficiency.

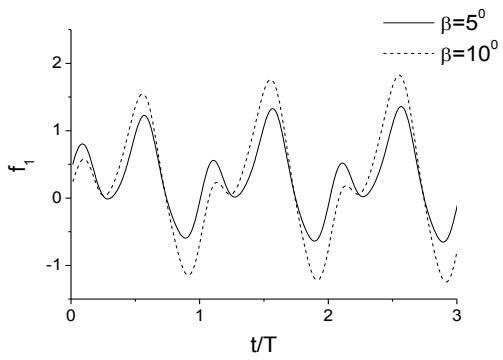

(a)

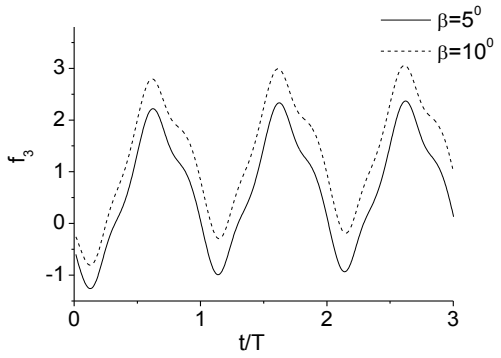

(b)

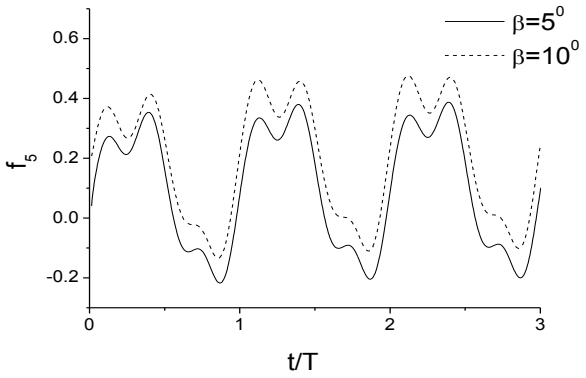

(c)

Figure 4.13 The forces histories with $St = 0.3, h_0 / C = 0.75$, $\alpha_0 = 10^0, \varepsilon = 90^0$. (a) f_1 (b) f_3 (c) f_5

We further present the forces histories with $St = 0.3$, $h_0 / C = 0.75$, $\alpha_0 = 10^0$, $\varepsilon = 90^0$ in figure 4.13. The amplitude of the horizontal force curve with $\beta = 10^0$ is larger than that of $\beta = 5^0$, although their mean values are close. The lifting forces, as shown in figure 4.13(b), are periodical and have a non-zero mean line, which explains the mean lifting force in figure 4.13(b). The moment curves also have similar non-zero offsets as shown in figure 4.13(c). There are troughs and peaks in each motion cycle, which differ from these curves in figures 4.11. The curves do not show the simple superposition of

those induced by the steady motion and the oscillatory motion. They are then decomposed into components of frequencies $n\omega$. We have similar to Hu et al (2002) and Wang & Wu (2006)

$$f_i = b_0 + \sum_{n=1}^{\infty}(a_n \sin n\omega t + b_n \cos n\omega t),\ i = 1,\ 3,\ 5, n = 1,\ 2,\ 3.... \tag{4-17}$$

The least square method has been used to obtain the coefficients a_n and b_n, by truncating the expansion at $n = 4$. Table 4.1 shows the details of the coefficients of each component. Unlike the case of $\beta = 0$ in above sections, the force and moment at $\beta \neq 0$ have all the components $n\omega$, $n = 0,\ 1,\ 2...$ It is evident that the argument of Wu (1994, 2000) is no longer valid in this case and this kind of behaviour of the force and moment there can no longer be expected here. As β doubles its value from 5^0 to 10^0, the components of the horizontal force at $n = 1,\ 3$ and the components of the lifting force and moment at $n = 0,\ 2,\ 4$ are also approximately doubled. These components are in fact zero when $\beta = 0$, as discussed previously. It is therefore not too surprising to see they vary approximately linearly with β when β is small. The peaks and troughs in figure 4.13(c) are the results of first, second and third order terms, since the coefficients of the second and third order terms are $20\% \sim 30\%$ of the first order terms.

Table 4.1 decomposition of the forces with $St = 0.3, h_0 / C = 0.75,\ \alpha_0 = 10^0, \varepsilon = 90^0$

	b_0	a_1	b_1	a_2	b_2	a_3	b_3	a_4	b_4
$f_1, \beta = 5^0$	0.285	0.068	-0.614	0.491	0.243	0.032	-0.032	0.065	-0.040
$f_1, \beta = 10^0$	0.270	0.133	-1.229	0.500	0.220	0.061	-0.063	0.062	-0.038

$f_3, \beta = 5^0$	0.798	-1.184	-0.802	-0.027	0.078	-0.201	0.120	0.013	-0.003
$f_3, \beta = 10^0$	1.590	-1.161	-0.774	-0.052	0.154	-0.192	0.112	0.025	-0.006
$f_5, \beta = 5^0$	0.118	0.278	-0.051	0.017	0.026	0.084	-0.001	-0.002	0.001
$f_5, \beta = 10^0$	0.233	0.274	-0.037	0.033	0.051	0.083	-0.002	-0.004	0.003

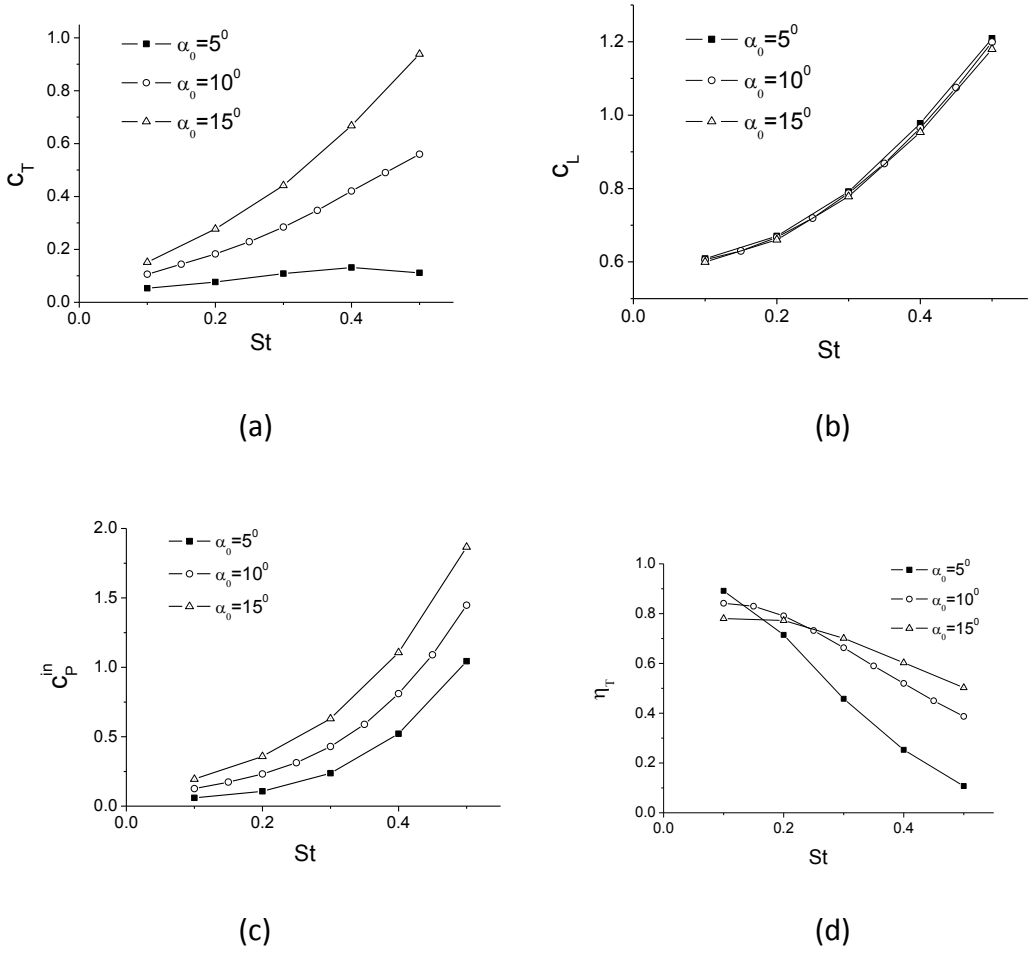

Figure 4.14 the performance with $h_0/C = 0.75$, $\beta = 5^0$, $\varepsilon = 90^0$. (a) thrust (b) lifting force (c) input power (d) propulsive efficiency.

Figure 4.14 gives the performance of the foil with $h_0/C = 0.75$, $\beta = 5^0$, $\varepsilon = 90^0$ at different α_0 against St. We can see in figures 4.14(a) & (c) that the thrust coefficient

and input power increase with St. Generally, the thrust, shown in figure 4.14(a), is linearly proportional to α_0 at smaller St number. As St increases, the thrust force with $\alpha_0 = 10^0$, 15^0 keep increasing, but the curve with $\alpha_0 = 5^0$ decreases. Figure 4.14(b) shows that the average lifting force increases with St. However it is not strongly affected by α_0. Figure 4.14(d) shows that the propulsive efficiency decreases as St increases. To give some insight into the effect of α_0, figure 4.15 gives the forces history at $St = 0.3, h_0 / C = 0.75$, $\beta = 5^0$, $\varepsilon = 90^o$. We further give the coefficients of the force components in Table 4.2, decomposed using Eq.(4-17). The whole horizontal force curve, as shown in figure 4.15(a), moves up as α_0 increases. As expected then, the mean value term $|b_0|$ for thrust increases in table 4.2. For the second order terms, $|a_2|$ decreases and $|b_2|$ increases as α_0 increases, which result in a slight change of the phase of troughs and peaks. In addition, the third and fourth order terms have some non negligible effects. Figures 4.15(b) & (c) present the lifting force and moment. Their decomposed coefficients in table 4.2 show that the constant term b_0 changes slightly and first order terms $|a_1|$ and $|b_1|$ decrease and increase respectively, as α_0 increases. This means that there is a change of location of the peak.

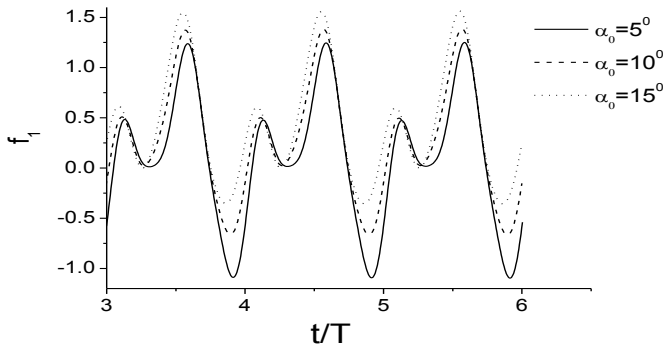

Figure 4.15(a) To be continued on next page

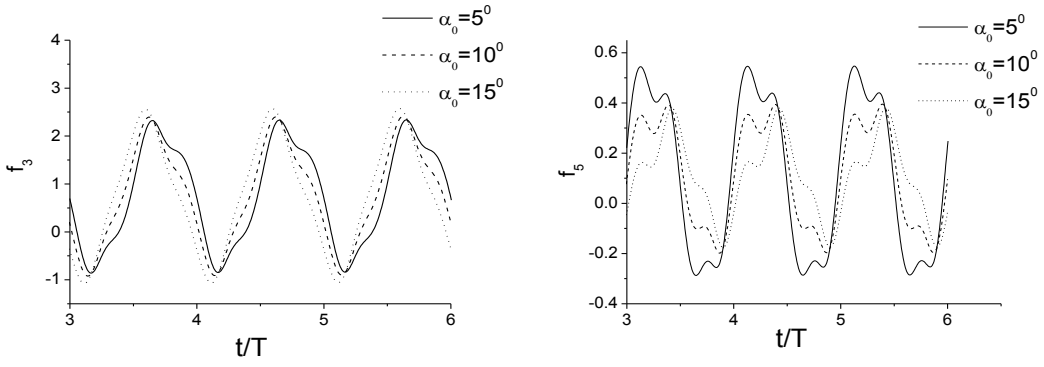

(b) (c)

Figure 4.15 The force history with $St = 0.3, h_0 / C = 0.75$, $\beta = 5^0$, $\varepsilon = 90^0$ (a) f_1 (b) f_3 (c) f_5

Table 4.2 Decomposition of the forces in figure 4.15.

	b_0	a_1	b_1	a_2	b_2	a_3	b_3	a_4	b_4
$f_1, \alpha_0 = 5^0$	0.110	0.112	-0.656	0.623	0.054	0.033	-0.038	0.082	-0.058
$f_1, \alpha_0 = 10^0$	0.285	0.068	-0.614	0.491	0.243	0.032	-0.032	0.065	-0.040
$f_1, \alpha_0 = 15^0$	0.442	0.022	-0.568	0.399	0.409	0.028	-0.025	0.048	-0.023
$f_3, \alpha_0 = 5^0$	0.802	-1.420	-0.314	-0.004	0.076	-0.198	0.161	0.017	-0.007
$f_3, \alpha_0 = 10^0$	0.798	-1.184	-0.802	-0.027	0.078	-0.201	0.120	0.013	-0.003
$f_3, \alpha_0 = 15^0$	0.788	-0.950	-1.292	-0.044	0.075	-0.185	0.074	0.009	0.000
$f_5, \alpha_0 = 5^0$	0.122	0.425	0.066	0.014	0.030	0.097	0.007	-0.003	0.002
$f_5, \alpha_0 = 10^0$	0.118	0.278	-0.051	0.017	0.026	0.084	-0.001	-0.002	0.001
$f_5, \alpha_0 = 15^0$	0.112	0.136	-0.161	0.018	0.020	0.069	-0.007	-0.001	0.001

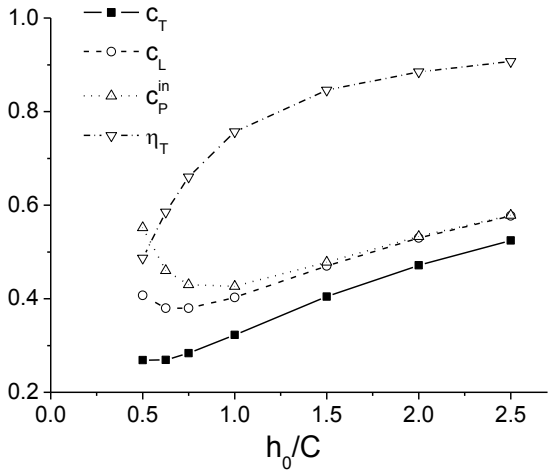

Figure 4.16 The effect of h_0 / C to the flying mode under $St = 0.3$, $\beta = 5^0$, $\alpha_0 = 10^0$, $\varepsilon = 90^0$

As discussed in section 4.2.2.2, the increase of vertical motion amplitude would result in the increase of the thrust and propulsive efficiency. Here we study its effect on the flying mode. The simulations are carried out at $St = 0.3$, $\beta = 5^0$, $\alpha_0 = 10^0$, $\varepsilon = 90^0$, with h_0 / C varying from 0.5 to 2.5. The thrust coefficient increases with h_0 / C; and the input power and mean lifting force decrease and then increase, as shown in figure 4.16. However, the propulsive efficiency increases as h_0 / C becomes larger.

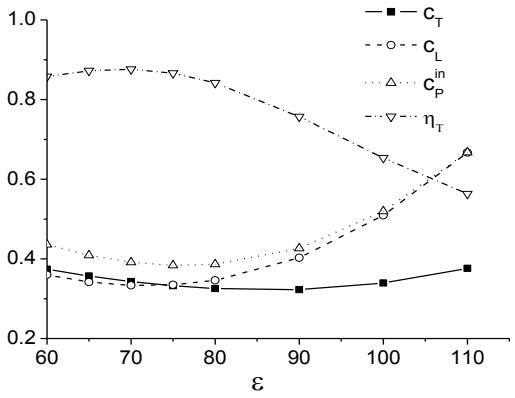

Figure 4.17 The effect of ε on the flying mode under $St = 0.3$, $\beta = 5^0$, $\alpha_0 = 10^0$, $h_0 / C = 1.0$

The effect of phase difference ε on vertical and rotational motion is also investigated. We choose $\beta = 5^0$, $St = 0.3$, $h_0 / C = 1.0$, $\alpha_0 = 10^0$, and ε increases from 60^0 to 110^0. We plot the thrust, mean lifting force, input power and propulsive efficiency in figure 4.17. The lowest value of c_T, c_P^{in} appear when $\varepsilon \approx 90^0$ and $\varepsilon \approx 75^0$ respectively. The highest efficiency of propulsion $\eta_T \approx 84\%$ when $\varepsilon \approx 70^0$.

4.3 The vortex shedding of a thin plate

When the thickness of the foil approaches zero, the foil becomes a plate. The continuous vortex shedding from the plate is similar to that of a foil. To solve the BVP, the body surface boundary condition and Kelvin vortices conservation condition are satisfied. Comparing the vortex shedding scheme for a foil, the time stepping procedures have minor changes when imposing the Kutta condition.

4.3.1 Equations and time stepping scheme for a plate

We consider a plate advancing forward with/without harmonic vertical and rotational motions. The governing equation and the body surface boundary condition are the same as those in chapter 2. As the plate is concerned, the normal velocities on the two sides of the plate have same magnitude and direction but opposite in sign with respect to $\vec{n}$. We have

$$\frac{\partial \phi_+}{\partial n} = -\frac{\partial \phi_-}{\partial n} \tag{4-18}$$

where ϕ_+, ϕ_- are the potential on the right and left hand sides of the plate when one walks along the plate towards trailing edge.

We define

$$\mu = \phi_+ - \phi_- \tag{4-19}$$

on the body surface. As p approaches the plate, the coefficient on the left hand side of Eq(2-23) remains 2π . Using Eqs.(4-18) & (4-19), the boundary integral equation (2-23) can then be written as

$$2\pi\phi(p) = \int_{S_0} \frac{\partial G(p,q)}{\partial n_q} \mu(q) dS_q + \int_{S_W} \frac{\partial G(p,q)}{\partial n_q} \mu(q) dS_w \tag{4-20}$$

Substituting Eqs.(4-2) & (4-3) into Eq.(4-20), we have

$$\begin{aligned} 2\pi\phi(p) &= \int_{S_0} \frac{\partial H(p,q)}{\partial s} \mu(q) dS + \int_{S_w} \frac{\partial H(p,q)}{\partial s} \mu(q) dS \\ &= -\int_{S_0} H(p,q)\gamma(q) dS - \int_{S_w} H(p,q)\gamma(q) dS \end{aligned} \tag{4-21}$$

in which integration by parts and zero $\mu(q)$ value at the leading edge and at the end of the vortex ending have been applied.

Applying the body surface condition Eq.(4-1) to Eq.(4-21), we have

$$\frac{\partial \phi(p)}{\partial n_p} = -\frac{1}{2\pi} \int_{S_0} \frac{\partial H(p,q)}{\partial n_p} \gamma(q) dS - \frac{1}{2\pi} \int_{S_w} \frac{\partial H(p,q)}{\partial n_p} \gamma(q) dS \tag{4-22}$$

To solve the BVP through boundary elements, the plate is divided into N segments. Linear distribution of vortex on each segment is assumed and the non-penetration boundary condition is imposed at the middle of each segment. At $t = 0$, there is no vortex wake. There are N equations based on Eq.(4-22). To solve the $N+1$ unknowns on the segment nodes, one complementary equation is required. Kelvin theorem requires the total circulation to be zero, we have

$$\int_{S_0} \gamma(q) dS = 0 \tag{4-23}$$

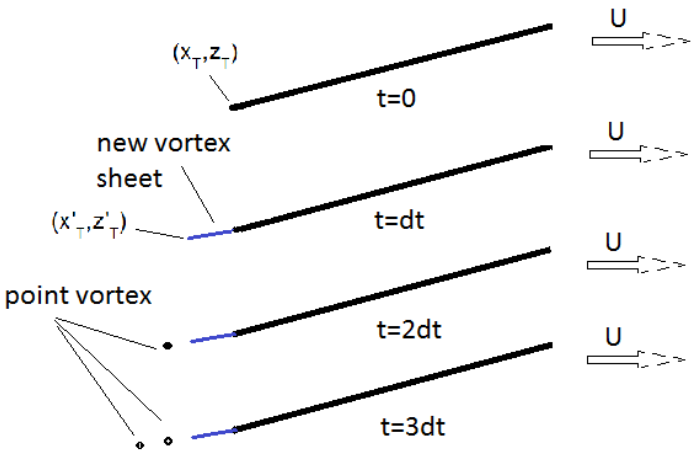

Figure 4.18 Scheme of the vortex shedding of a plate

Figure 4.18 presents an illustration for the scheme. At $t = dt$, there will be one free vortex segment connected to the trailing edge. Eqs.(4-6) & (4-7) are adopted to update the position of the end node of S_{w1}. The vortex strength is updated similar to Eq.(4-9), we have

$$\gamma(\vec{x}'_T, t+dt) = \gamma(\vec{x}_T, t) \tag{4-24}$$

The unsteady Kutta condition is circumvented by the assumption of continuous distribution of vortex over the plate and free vortex sheet. The Kelvin theorem in Eq.(4-23) at $t = dt$ becomes

$$\int_{S_0} \gamma(q)dS + \int_{S_{W1}} \gamma(q)dS = 0 \tag{4-25}$$

which means that the total circulation of the plate and the newly shed vortex wake is zero. There are $N+1$ unknowns (the vortex strength at the end node of S_{w1} is known) and the algebraic equation can then be solved.

As the time step advances forward, the wake segment of S_{w1} will move downstream and is approximated by a point vortex at the middle of the segment. We have the

strength of the point vortex

$$\Gamma_i = \int_{S_{W1}} \gamma(q) dS \tag{4-26}$$

The strength of the point vortex is known and will remain unchanged subsequently and new S_{w1} will form. At $t = 2dt$, The new vortex segment, which is shed from the trailing edge, is developed and its end node position is calculated by Eqs.(4-6) & (4-7). Eq.(4-22) can then be rewritten as

$$\frac{\partial \phi(p)}{\partial n_p} = -\frac{1}{2\pi} \int_{S_0} \frac{\partial H(p,q)}{\partial n_p} \gamma(q) dS - \frac{1}{2\pi} \int_{S_w} \frac{\partial H(p,q)}{\partial n_p} \gamma(q) dS - \frac{1}{2\pi} \sum \Gamma_i \frac{\partial H(p,q)}{\partial n_p} \tag{4-27}$$

The Kelvin theorem gives an additional equation

$$\int_{S_0} \gamma(q) dS + \int_{S_{W1}} \gamma(q) dS + \sum \Gamma_i = 0 \tag{4-28}$$

Repeat the scheme and the simulation continues.

In the present simulation, the shedding velocity of the new point vortex in Eqs.(4-6) & (4-7) is replaced by the velocity of the newly shed vortex sheet at the middle point of S_{w1} for approximation. This treatment is not mathematically rigorous. However, numerical tests show a convergent solution and this will be verified.

The pressure difference over the plate can be written as

$$\begin{aligned} \Delta p_{re} &= p_{re}^{+} - p_{re}^{-} == -\rho[\frac{D(\phi^{+} - \phi^{-})}{Dt} - U_{s0} \cdot \frac{\partial \mu}{\partial s}] \\ &= -\rho(\frac{D\mu}{Dt} - U_{s0} \cdot \gamma) \end{aligned} \tag{4-29}$$

where $U_{s0} = (U + \dot{\theta} Z, \dot{h} - \dot{\theta} X) \cdot \vec{s}$ is the tangential velocity of the plate.

The force on the plate is obtained from pressure integration, we have

$$F_i = \int_{S_0} \Delta p_{re} n_i dS = -\rho \int_{S_0} (\frac{D\mu}{Dt} - U_{s0} \cdot \gamma)\ n_i dS\ , i = 1,\ 3,\ 5 \tag{4-30}$$

We notice that the integration is performed numerically and the 'suction force' at the leading edge has been ignored.

4.3.2 Simulation of vortex shedding of plate

4.3.2.1 Numerical results for a flat plate

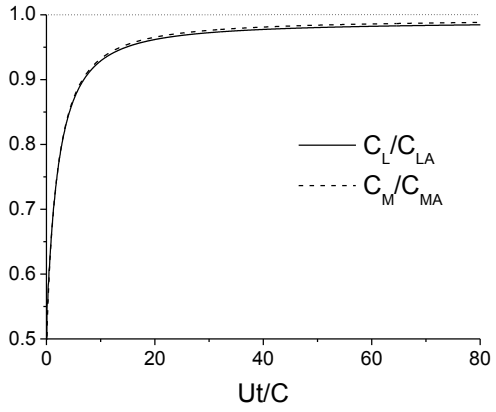

Figure 4.19 The lifting force and moment of a plate start with constant U , $\beta = 5^0$.

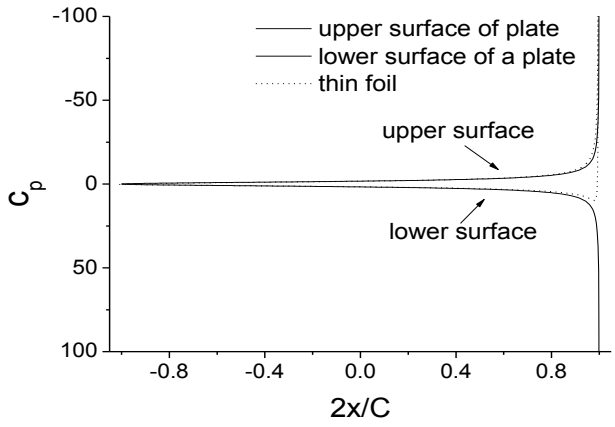

Figure 4.20 The pressure distribution over a plate at $Ut/C = 80$

The numerical scheme is first verified through a plate in steady motion. We consider a plate travelling at constant speed with small attack angle. The node of the element is based on equal spaced cosine function with $x_i = 0.5C\cos(i\pi/100),\ i = 1 \sim 100$. The result in figure 4.19 shows the force history on the plate against travelled distance. The

curves are ratios of the calculated results to the steady linear analytical lifting force coefficient $c_{LA} = 2\pi\beta$ and moment coefficient $c_{MA} = \pi\beta$ (Newman, 1977). The lifting force and moment approach the analytical solution of a steady plate. However, the gap between the numerical results and the analytical solution can be observed, even when $Ut/C = 80$, we have $c_L / c_{LA} = 0.985$ and $c_M / c_{MA} = 0.988$. The discrepancy would be further reduced if the plate travels a longer distance. However, we notice that the analytical solution of the vortex strength at the leading edge is infinite and will result a suction force (Newman, 1977, Grue et al 1988); while the present numerical solution is from a nonlinear vortex shedding method and the results at the leading edge are finite. Therefore, there is small discrepancy. We further present the pressure distribution over the plate, as shown in figure 4.20. Comparing the pressure of a thin foil with thickness $t_{ck} / C = 0.003$ and the plate, the overall pressure is very close except at the leading edge. The pressure on the lower surface of the thin foil is much smaller than that of a plate. This indicates that using a plate to replace the thin foil will bring in inaccuracy due to the difference at the leading edge (Giesing & Smith 1967).

We then consider the problem of a plate travelling at constant forward speed with oscillatory vertical and rotational harmonic motions. Small amplitude vertical motion is simulated first. Figure 4.21 presents the shed vortex structure and the lifting force history on the plate under $U = 1.0$, $\omega = \pi$, $h_0 / C = 0.025$, $\beta = 0$ or the Strouhal number $St = 0.05$. The shed vortices move up and down with the oscillatory motion. There are two rows of vortices close to the centre line, which resemble the Kármán Vortex Street. However, the vortices strength is reversed. This is referred to the reversed Kármán Vortex Street (Lighthill 1975, Anderson et al 1998). The vertical force is shown in figure 4.21(b). When compared with the linear analytical solution (Newman

1977), they are in good agreement although the amplitude of present result is a bit smaller.

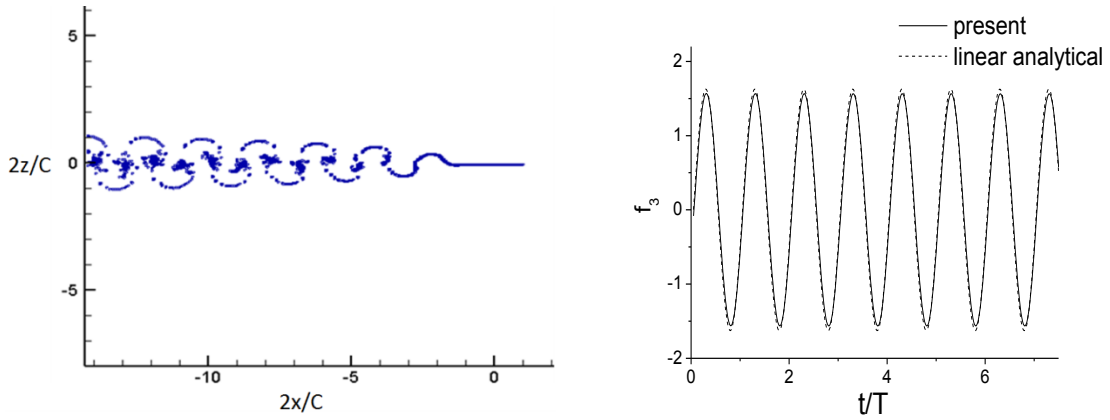

(a) (b)

Figure 4.21 Vertical motion of a plate in the unbounded flow, with $U = 1.0$, $h_0 / C = 0.025$, $\omega = \pi$ or $St = 0.05$ (a) vortex structure (b) vertical force history

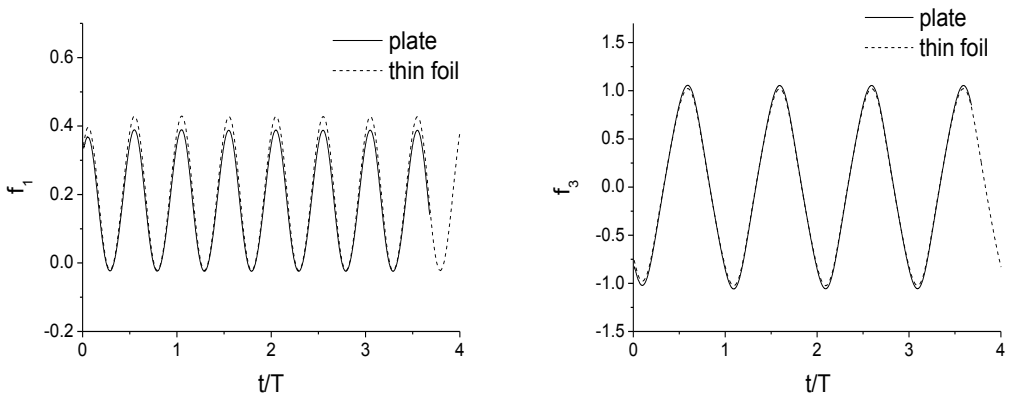

(a) (b)

Figure 4.22 To be continued on next page

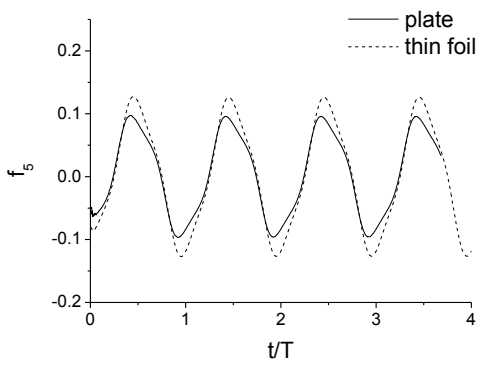

(c)

Figure 4.22 The force history under $St = 0.2$, $h_0 / C = 1.0$, $\alpha_0 = 10^0, \varepsilon = 90^0, \beta = 0$ (a) f_1 (b) f_3 (c) f_5

Table 4.3 The performance of the plate under $St = 0.2, h_0 / C = 1.0$, $\alpha_0 = 10^0, \varepsilon = 90^0$, $\beta = 0$

	c_T	c_P^{in}	η_T
plate	0.175	0.274	0.637
$t_{ck} / C = 0.003$	0.197	0.266	0.738

We further study a plate with larger amplitude motion. The force histories under $St = 0.2$, $h_0 / C = 1.0$, $\alpha_0 = 10^0, \varepsilon = 90^0, \beta = 0$ are shown in figure 4.22. Similar to figure 4.6, most of f_1 is above the zero line; the period of the horizontal force is half of the motion period due to the 'mirror effect' of the motions and flow at t and $t + T/2$ about $z = 0$ (Wu 1994, 2000). Comparing the force history of the plate and thin foil with $t_{ck} / C = 0.0015$, the peak of the horizontal force is slightly smaller; and the vertical forces are close although minor difference can be observed; the amplitude of the

moment is slightly smaller. As discussed above, the flow near the leading edge would be singular although numerical results give a finite value. The leading edge suction force has been ignored. The overall propulsive performance is shown in table 4.3. Comparing with the results from the thin foil, the thrust c_T is slightly smaller and input power c_P^{in} is slightly larger; therefore the propulsive efficiency is lower.

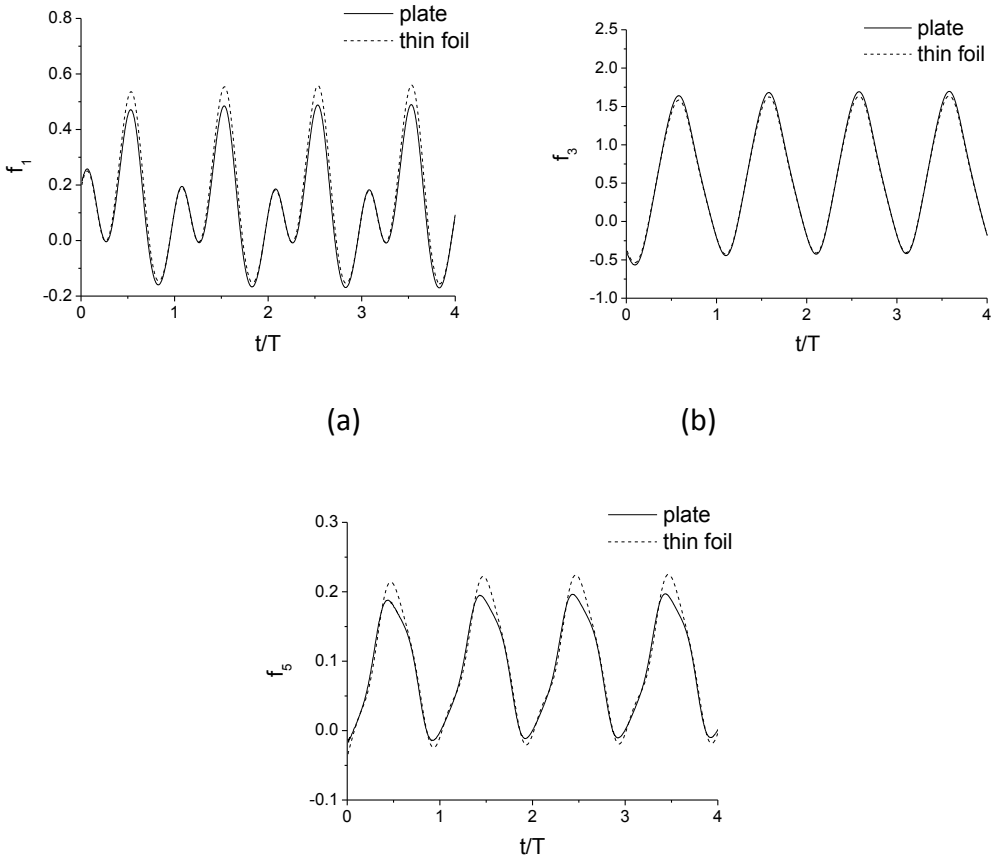

Figure 4.23 The force history under $St = 0.2$, $h_0 / C = 1.0$, $\alpha_0 = 10^0$, $\varepsilon = 90^0$, $\beta = 5^0$

(a) f_1 (b) f_3 (c) f_5

When the flying mode is considered, a non-zero mean attack angle $\beta = 5^0$ is introduced. The force histories under $St = 0.2$, $h_0 / C = 1.0$, $\alpha_0 = 10^0$, $\varepsilon = 90^0$ are shown in figure 4.23. Similar to figures 4.13 & 4.15, peaks and troughs in each period

can be observed and most of these curves are above the zero line. Comparing the results with that of thin foil with $t_{ck}/C = 0.0015$, the peak of the horizontal force is slightly smaller; and the vertical force amplitude is slightly larger; while the moment of the plate has smaller amplitude. The overall performance of the plate is presented in table 4.4. The thrust coefficient is smaller and the input power is slightly larger than that of the thin foil, which results a lower propulsive efficiency.

Table 4.4 The performance of the plate under $St = 0.2$, $h_0/C = 1.0$, $\alpha_0 = 10^0$, $\varepsilon = 90^0$, $\beta = 5^0$

	c_T	c_P^{in}	η_T
plate	0.117	0.274	0.430
thin foil	0.144	0.267	0.542

When a thin foil is replaced by a plate with zero thickness, the pressure distribution near the leading edge is no longer smooth but sharp (Giesing & Smith 1967). The velocity at the leading edge shall be infinite in the analytical solution. Grue & Palm (1988) treated the leading edge as a point with suction force by applying Blasius formula to a small circle of radius surrounding the leading edge. In the present study, the velocity at the leading edge is large and finite since the element size at the leading edge shall be finite; the contribution of the 'suction force' at the leading edge has been ignored. This could be the reason for the discrepancy when compared with thin foil.

4.3.2.2 Application to a compartment with bottom opening

Here we attempt to simulate the vortex shedding of a two dimensional compartment

with a bottom orifice/opening in heave motion. A semi-circular cylinder with bottom orifice/opening, which consists of two curved plates, as shown in figure 4.24, is adopted to approximate a damaged ship structure. The vortex shedding scheme for the plate is applied at the edge of the orifice at the bottom.

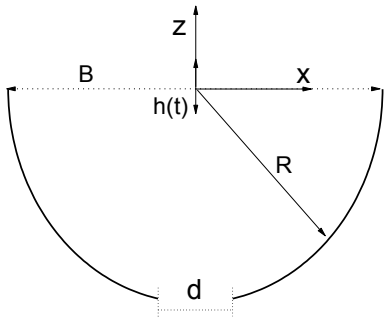

Figure 4.24 The sketch of a semi-circular column model with orifice

To avoid the impulsive motion or acceleration, the vertical motion of the compartment is then given by

$$\dot{h}(t) = \begin{cases} \omega h_0 \cos(\omega t + \pi) \dfrac{(1 - \cos\dfrac{\pi t}{T})}{2}, & t < iT \\ \omega h_0 \cos(\omega t + \pi), & t > iT \end{cases} \tag{4-31}$$

where an initial phase angle π is added, i is the number of the smoothing period.

Unlike the vortex shedding of a foil the vortices will not move away the structures. When longer time simulations are considered, one key numerical problem is the damping of vortices. The vortices will not dissipate since viscosity has been ignored in the framework of potential flow. Kristiansen & Faltinsen (2008, 2010) attempted to

'dump' the vortex sheet when the dipole strength equals zero after it shed a short time. However, the 'dumping' of the vortex sheet would cause a sudden variation of the local flow; the discontinuity of the flow field would cause a large impulse force when the Bernoulli equation was used to calculate the pressure. For a compartment with symmetric orifice, the vortices appear in pairs. Consider the mixing and cancelling of the vortices, a smooth artificial dissipative function is introduce to damp the vortices. Here we assume that the strength of the vortices decreases gradually through a dissipative function based on time. We have

$$f_{damping}(t_i)=\begin{cases}0, & t_i > t_{end}\\ \frac{1}{2}(1+\cos\frac{\pi(t_i-t_{start})}{t_{end}-t_{start}}), & t_i > t_{start}\\ 1, & t_i < t_{start}\end{cases} \tag{4-32}$$

where $t_i = t - t_{temp}$ is the existing time of the point vortex from the moment the point vortex is generated, t_{start}, t_{end} are the start and end time of the damping.

Parameters t_{start}, t_{end} used in the present simulation are usually chosen between $[\frac{1}{4}T, T]$ as long as the chosen parameters have no significant effect on the main flow and hydrodynamic force.

Figures 4.25(a)&(b) show the vortices moving along with the ingress and egress flow near the orifice of the compartment under $h_0/B=0.1$, $f=1.0$, $d/B=0.1$. Here the frequency f is used to describe the motion instead of St in this section since the forward speed $U=0$. In the simulation, $i=1$ is used in Eq.(4-31) and $t_{start}=0.25T$, $t_{end}=0.5T$ are used in Eq.(4-32). The shed vortex from the orifice always appears in pairs. Its motion mainly depends on the velocity of the motion and the flow through

the orifice. The pattern of those vortices is quite similar although the vortices strength and mean velocity are different. It is expected that the flow and hydrodynamic force would be affected by the orifice size, motion amplitude and frequency. These parameters will be investigated. When one parameter varies, the others will be fixed at $h_0 / B = 0.1,\ f = 1.0, d / B = 0.1.$

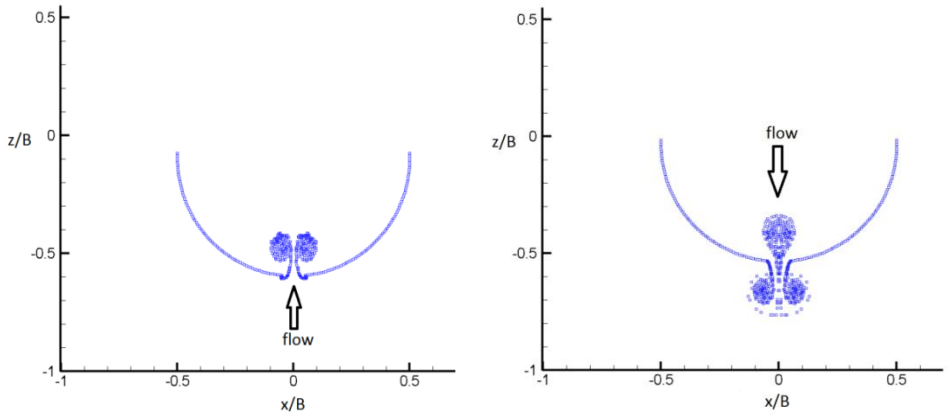

(a) (b)

Figure 4.25 The vortex structure near the orifice with $h_0 / B = 0.1,\ f = 1.0,$ $d / B = 0.1$ (a) ingress and (b) egress of the flow

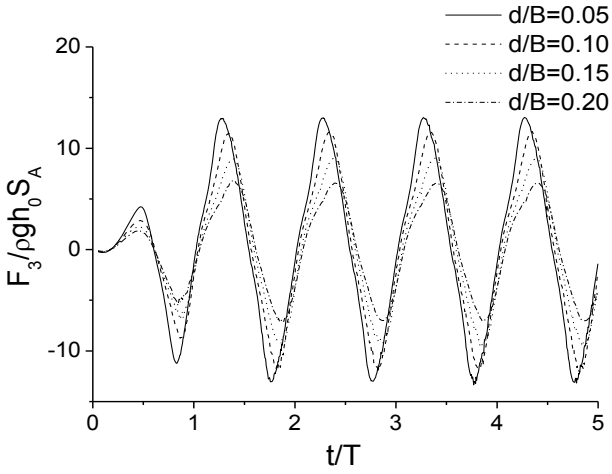

Figure 4.26 The effect of orifice size d / B

The effect of orifice size is investigated first. As shown in figure 4.26, the vertical force decreases as the orifice size increases. When the orifice size increases, it is expected that more fluid flow can ingress/egress the compartment and less fluid

moves along with the compartment. Table 4.5 shows the decomposed force obtained through Eq.(4-17). The constant term b_0 increases slightly; and the first order component a_1, which is referred to the 'added mass' term, decreases as d/B increases; while the value of $|b_1|$, which is referred to the 'damping' term, increases and then decreases. This indicates that the most significant damping effect appears with medium size orifice. Comparing with the first order terms, those higher order terms are less important.

Table 4.5 Decomposition of the vertical forces with different d/B under $f=1.0$, $h_0/B=0.1$

	b_0	a_1	b_1	a_2	b_2	a_3	b_3	a_4	b_4
$d/B=0.05$	0.40	11.52	-2.70	-0.04	0.42	-0.85	0.60	0.04	-0.04
$d/B=0.10$	0.35	9.65	-4.23	0.02	0.70	0.37	1.07	-0.08	-0.05
$d/B=0.15$	0.28	7.14	-4.80	0.37	0.63	0.72	0.18	-0.03	-0.02
$d/B=0.20$	0.19	5.04	-4.17	0.49	0.37	0.46	-0.15	-0.02	0.01

Table 4.6 Decomposition of the vertical forces with different h_0/B under $f=1.0$, $d/B=0.1$

	b_0	a_1	b_1	a_2	b_2	a_3	b_3	a_4	b_4
$h_0/B=0.05$	0.12	7.03	-4.58	0.27	0.25	0.69	0.02	0.01	0.02
$h_0/B=0.10$	0.35	9.65	-4.23	0.02	0.70	0.37	1.07	-0.08	-0.05
$h_0/B=0.15$	0.56	10.5	-3.46	-0.21	0.69	-0.31	1.15	-0.01	-0.11
$h_0/B=0.20$	0.78	10.8	-2.90	-0.22	0.68	-0.72	1.0	0.05	-0.16

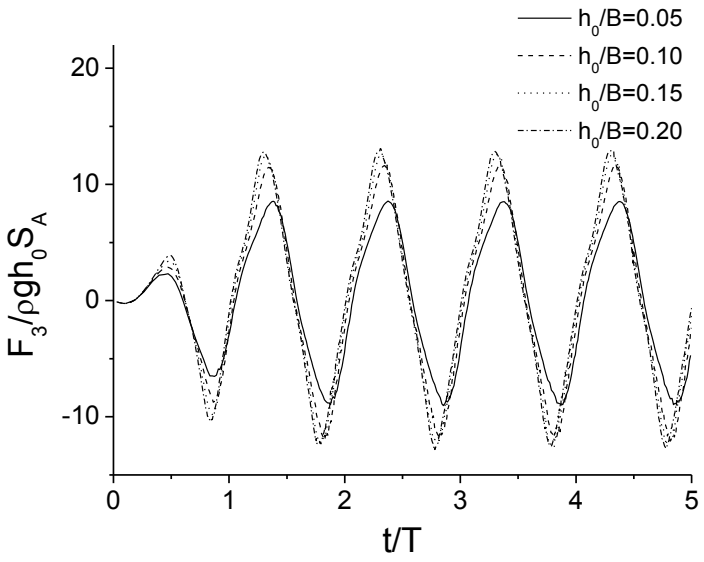

Figure 4.27 The effect of vertical motion amplitude h_0 / B with $f = 1.0$, $d / B = 0.1$

The effect of motion amplitude h_0 / B under $f = 1.0$, $d / B = 0.1$ is studied. The overall vertical force increases as h_0 / B, as shown in figure 4.27. In table 4.6, the value of b_0 and a_1 increases and $|b_1|$ decreases as h_0 / B increases, and the increment of a_1 is larger than the decrement of $|b_1|$. This results in the increase of the overall force amplitude.

Table 4.7 Decomposition of the vertical forces with different f under $h_0 / B = 0.1$, $d / B = 0.1$

	b_0 / f^2	a_1 / f^2	b_1 / f^2	a_2 / f^2	b_2 / f^2	a_3 / f^2	b_3 / f^2	a_4 / f^2	b_4 / f^2
$f = 0.5$	0.35	9.66	-4.20	0.01	0.70	0.36	1.07	-0.07	-0.05
$f = 1.0$	0.35	9.65	-4.23	0.02	0.70	0.37	1.07	-0.08	-0.05
$f = 1.5$	0.36	9.67	-4.23	0.04	0.68	0.37	1.10	-0.07	-0.03

The effect of frequency is considered next. A increase of vertical force amplitude is expected as the frequency increases. The force history is not plotted here as the periods of different frequency are very different. However, table 4.7 shows the decomposed force components over the square of the frequency. The value of $|b_0|$, $|a_1|$, $|b_1|$ and most of these higher order components over the square of the frequency are very close. This indicates that the motion and vortex shedding can be non-dimensionalized with the square of the frequency in the unbounded flow when h_0 / B and d / B are fixed. This indicates that the effect of damping force in the unbounded flow is quadratic to the motion frequency.

Chapter 5 The nonlinear free surface effect on a hydrofoil

5.1 Introduction

Many previous works on 2D and 3D foils with steady or periodic motion, including Giesing & Smith (1967), Bal (1999), and Zhu, Liu & Yue(2006), adopted linear free surface conditions. The free surface effect, which has been studied in chapter 3, varies significantly under different submergence and Froude number. When the foil is close to the surface, the nonlinear effect of the free surface and free vortex wake would become important. The free vortices shed from the trailing edge interact with the free surface, and in return affect the flow around the foil. Faltinsen & Semenov (2008) adopted the nonlinear free surface boundary condition in their studies and the wave profile was achieved through iteration. However, there are only a few works that focus on the transient motion of an arbitrary foil. The nonlinear free surface effect on a foil in steady motion at small attack angle has been studied by Landrini, Lugni & Bertram (1999), the free surface was tracked using the time stepping method. However, large amplitude motion of a foil near the water surface seems absent, where the cross-coupling effect of foil, wave motion and vortex wake shall be investigated.

Here we consider a foil traveling under the water surface with constant forward speed and harmonic vertical and rotational motions; the vortex shedding and wave motion are tracked through the time stepping scheme. Nonlinear free surface boundary conditions are used when updating the free surface. The nonlinear vortex shedding scheme, which is outlined in chapter 4, is adopted to track the free vortices. As the free surface effects are included, the hydrodynamic performances of a hydrofoil travelling at different Froude number and submergence are studied. NACA 0012 is used for the simulation. The oscillatory vertical and rotational motion for propulsion, energy harvesting and flying are simulated under a few selected submergence and Froude

number.

When the foil is very close to the free surface, the nonlinear effect of the surface wave becomes important; the wave may break and cause difficulties in the simulation. One of the challenges is the instability caused by the vortex wake when the vortices nearly touch the free surface. The free surface may distort or break. Therefore, the simulation has been made with certain limits of the submergence of the foil. The present work is for non-breaking wave. To avoid the breaking of the free surface, the foil cannot penetrate the free surface. The amplitude of the vertical motion shall be much smaller than the submergence. There shall be a sufficient gap between the water surface and the top position of the foil.

5.2 Description of the free surface

Apart from the nonlinear vortex shedding behind a hydrofoil, the transient nonlinear free surface effect on the foil is the concern of this chapter. A moving coordinate system oxz, with origin on the mean free surface, is adopted (see figures 3.1 and 5.1). The fluid flow satisfies the Laplace equation, the body surface boundary condition, Kutta condition as those in chapter 4. The Lagrangian form of the non-linear free surface boundary conditions are used in this chapter. The boundary integral equation, therefore, includes the foil surface S_0, vortex wake S_w, free surface S_F and control surface S_C, as shown in figure 5.1. Once the BVP is solved, the free surface is updated and the simulation continues. This is actually the procedures of the well-known Mixed-Eular-Lagrangian method proposed by Longuet-Higgins & Cokelet (1976). The pressure and force on the foil can be obtained using Eq.(4-13).

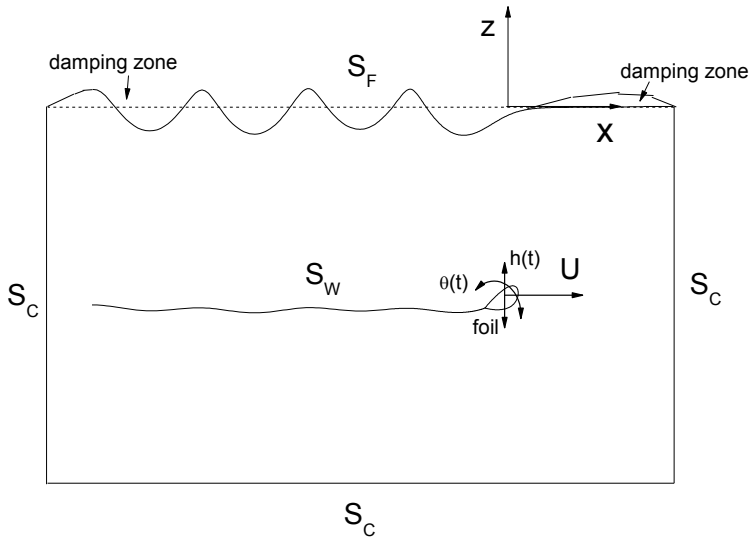

Figure 5.1 The sketch of the foil under free surface

The free surface is discretized by small elements, the size of the elements on the free surface near the foil (say $|x| < 2C$) is of the similar order of those on the foil surface. The element size on the free surface increases gradually when approaching the far field. We also notice that the element would be very large when large computational area is considered. Therefore, 20 to 30 elements in each wavelength are required. To save the computational effort without losing accuracy, the size of the elements is set as f_{elemt} times its basic element size l_0 based on the coordinates system in x axis. We have

$$f_{elemt} = \begin{cases} 1\ ,\ |x| < 2C \\ s_{elemt} + (1 - s_{elemt})(1 + |x| - 2C)\ ,\ |x| > 2C,\ [s_{elemt} + (1 - s_{elemt})(1 + |x| - 2C)] < \dfrac{\lambda_w}{25 l_0} \\ \dfrac{\lambda_w}{25 l_0},\ [s_{elemt} + (1 - s_{elemt})(1 + |x| - 2C)] > \dfrac{\lambda_w}{25 l_0} \end{cases} \tag{5-1}$$

where λ_w is the typical wave length, the parameter s_{elemt} is chosen within $[0.2,\ 0.5]$.

To update the free surface, free surface boundary conditions in Eqs.(2-11) & (2-12) will be imposed. The constant forward velocity is incorporated since we use a moving coordinate system. As the oscillation is considered, the radiation wave propagates outside to the far field. A wave absorbing zone / damping zone is introduced. Here we adopted the damping zone used by Tanizawa & Swada (1996) and Wang & Wu (2006). The free surface boundary condition can be written as

$$\frac{d\phi}{dt} = \frac{1}{2}\nabla\phi\nabla\phi - gz - c(x)\phi \tag{5-2}$$

$$\frac{dx}{dt} = \frac{\partial\phi}{\partial x}, \quad \frac{dz}{dt} = \frac{\partial\phi}{\partial z} - c(x)z \tag{5-3}$$

where $c(x) = \begin{cases} 0, & |x| < x_1 \\ c_a\omega(\dfrac{|x| - x_1}{\lambda_w})^2, & x_1 < |x| < x_1 + c_b\lambda_w \end{cases}$

As suggested by Tanizawa & Swada(1996), $c_a = 1$ and $c_b = 1$ can be used and the wave would be absorbed; there would not be a significant reflecting wave. The wave motion near the control surface is very limited and therefore can be treated as a solid boundary (Wang & Wu 2006). We have

$$\frac{\partial\phi}{\partial n} = 0 \tag{5-4}$$

on S_C.

When updating the free surface, the time step is chosen to make sure that the displacement of each element is less than or equal to one quarter of the basic element. The time step dt is chosen based on the maximum velocity of free surface and vortex wake, we have

$$dt = \min(dt_0,\ dt_w,\ \frac{l_0}{4V_{f\_\max}}) \tag{5-5}$$

where $dt_0 = 0.005T$ is the time step base on the oscillation period if applicable; dt_w is the time step based on the shed vortex, details have been discussed in chapter 4; $V_{f\_\max}$ is the maximum velocity of the free surface.

The re-meshing procedures are followed since the element sizes on the free surface are not even. Here the re-meshing is achieved through interpolation. The original x coordinate of each element is used during the interpolation; the value of z coordinate and the potential ϕ at each time step are obtained through four-point-Lagrangian interpolation equation. For the normal interpolation point, two points before and two points after it are used, as shown in figure 5.2(a); while for the point near the fore/aft control surface, the first or last four points are used, as shown in figure 5.2(b). The procedures can give good results for the present simulations. When the free surface becomes steep or the overturning wave appears, the interpolation procedures would be a problem; a re-meshing procedure based on the arc length shall be used (Wang & Wu 2006).

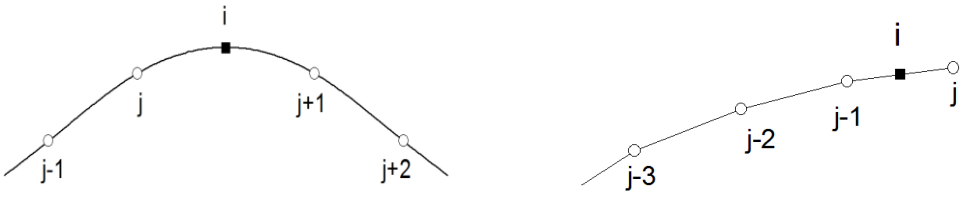

(a) (b)

Figure 5.2 Illustration of the interpolation, i is the interpolation point. (a) two before and two after the interpolation point (b) interpolation near the control surface

For longer time simulations, smoothing technique becomes necessary since the free surface profile would have saw-tooth behaviour due to numerical instability. The five point algorithms, which were used by Longet-Higgins & Cokelet (1976), Maruo & Song (1994), Xu, Duan & Wu (2010), can be adopted to smooth the wave elevation and the potential. Here we adopt what has been used by Maruo & Song (1994), Xu, Duan & Wu (2010). If the element nodes are numbered sequentially from 1 to m, we then have

$$f_1 = \frac{1}{70}(69x_1 + 4x_2 - 6x_3 + 4x_4 - x_5) \tag{5-6}$$

$$f_2 = \frac{1}{35}(2x_1 + 27x_2 + 12x_3 - 8x_4 + 2x_5) \tag{5-7}$$

$$f_i = \frac{1}{35}(-3x_{i-2} + 12x_{i-1} + 17x_i + 12x_{i+1} - 3x_{i+2}) \tag{5-8}$$

$$f_{m-1} = \frac{1}{35}(2x_{m-4} - 8x_{m-3} + 12x_{m-2} + 27x_{m-1} + 2x_m) \tag{5-9}$$

$$f_m = \frac{1}{70}(-x_{m-4} + 4x_{m-3} - 6x_{m-2} + 4x_{m-1} + 69x_m) \tag{5-10}$$

The coordinate z or potential ϕ can also be smoothed using the above equations after x is replaced by z or ϕ.

5.3 Results on the transient free surface effect and discussion

5.3.1 Steady motion near free surface

The transient motion of a foil beneath the free surface at constant forward speed is considered. The transient force on a foil in unbounded flow has been studied in chapter 4. Before the steady force on the foil is achieved, the lifting force on the foil increases rapidly when the foil starts to move at constant speed. Here we attempt to study the transient surface wave effect on a foil in steady motion. The simultaneous interaction of foil, nonlinear wave and vortex wake are simulated through the time

stepping method. The hydrodynamics of a foil travelling at different speed and different submergences are investigated.

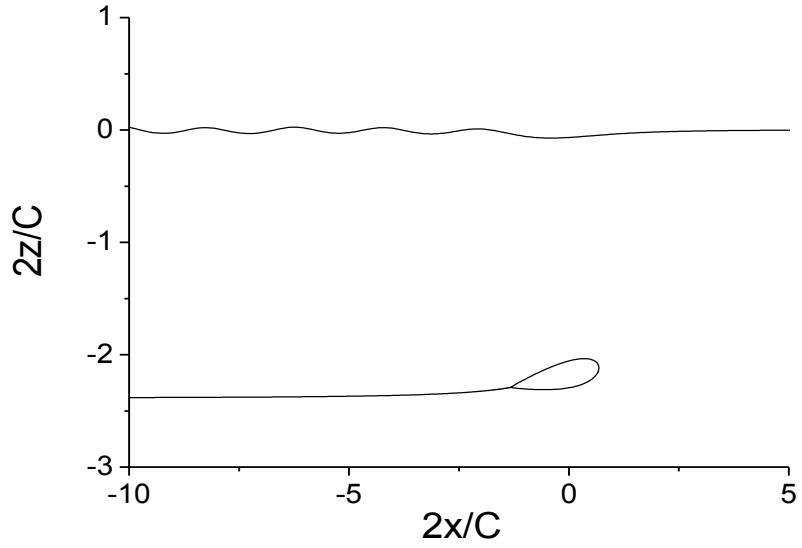

(a)

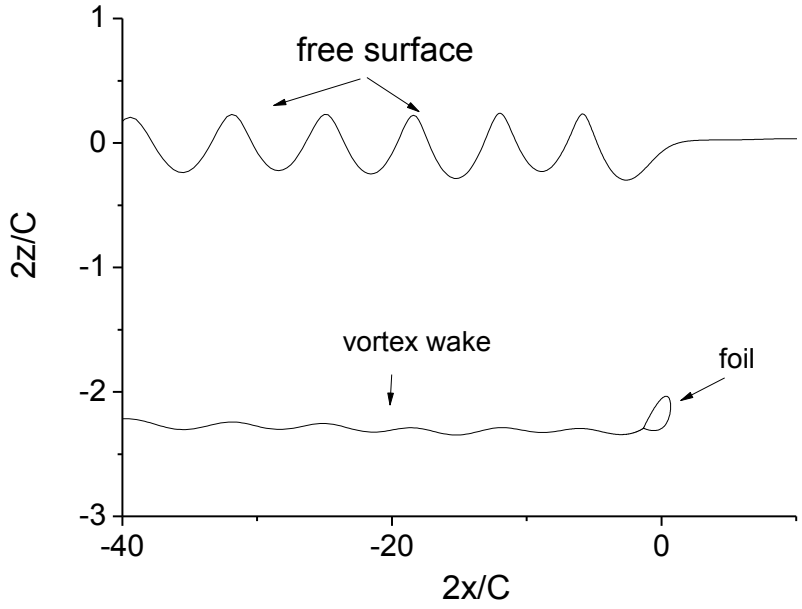

(b)

Fig. 5.3 To be continued on next page

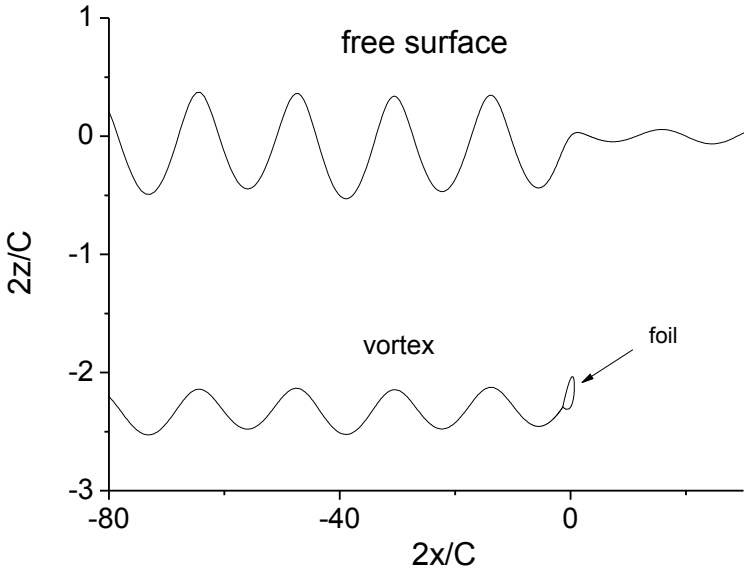

(c)

Figure 5.3 The free surface profile and wake of NACA 0012 with $h_C/C=1.0$, $\beta=5^0$ (a) $Fn=0.4$, $Ut/C=23$ (b) $Fn=0.8, Ut/C=80$ (c) $Fn=1.2$, $Ut/C=140$

First of all, the simulations on NACA0012 at different forward speed are undertaken. Figure 5.3 shows the vortex wake behind the foil and the wave profile of different velocities under $h_C/C=1.0$, $\beta=5^0$. Comparing the curves in figures 5.3(a) (b) & (c), the wave amplitude and wave length increase with Fn. According to the linear steady theory, we have the wave number of the induced wave $\kappa=g/U^2$. As Fn increases at given C, the wave number becomes smaller, which means the induced wave has a longer wave length in space or larger period. This can explain figure 5.3 in spite of the fact that nonlinear free surface conditions are imposed. We also notice that the surface wave profile in figure 5.3(b) & (c) is similar to the nonlinear Stokes wave with steeper wave crests and flatter troughs. There is an obvious downwash of flow above the foil in figures 5.3(b) & (c) which would decrease the effective attack angle. While in figure

5.3(a), there is a small downwash and a following wave crest above the foil; this would increase the effective attack angle. Due to the induced waves, the lifting force coefficient shall be different. We notice that there is a small wave before the foil in figure 5.3(c), while in figures 5.3(a) & (b) there is no significant wave before the foil. This could be caused by the cross-coupling effect of the foil motion and the oscillatory vortex wake. It is expected that the induced wave would affect the vortex shedding. The vortex wake fluctuates with the surface wave and there is a downwash near the trailing edge in figures 5.3(b) & (c); the amplitude of the vortex wake increases when the wave amplitude becomes larger. Therefore the local flow around the foil is the coupled interaction of foil, surface wave and vortex wake. As expected, the circulation around the foil fluctuates due to the fully coupled motion of wave, body and vortex wake.

The time history of resistance, lifting force and moment under $h_C / C = 1.0$, $\beta = 5^0$ are shown in figure 5.4. When the foil starts moving at constant speed, the forces, including resistance, lift and moment, increase rapidly. Different from those lifting force in the unbounded flow in figure 4.4, these curves approaching their steady state with fluctuation with reduced amplitude as shown in figure 5.4. The surface wave due to impulsive motion of the foil affects the hydrodynamic force significantly. Comparing the lifting force of linear theory in chapter 3, the lifting force from the present study is larger at $Fn = 0.4$ and $Fn = 1.2$, but smaller at $Fn = 0.8$, as shown in figure 5.4(b). The discrepancy could be caused by the nonlinear free surface effect and nonlinear vortex shedding. In figure 5.3(b) (c), the downwash of the free surface and the vortex wake change the effective attack angle and affect the circulation of the foil. As discussed in the book of Katz & Plotkin (1991), the influence of the shed vortex sheet has a

significant effect on the lifting force. The force history is the history of the coupled motion of foil, nonlinear free surface and vortex wake.

Figure 5.5 gives the pressure distribution on the foil in figure 5.4 at $Fn = 0.4,\ 0.8,\ 1.2$ when the foil travels $Ut/C = 23,\ 80,\ 140$ respectively. As expected, the pressure coefficient difference of the upper and lower surface decreases as the velocity increases.

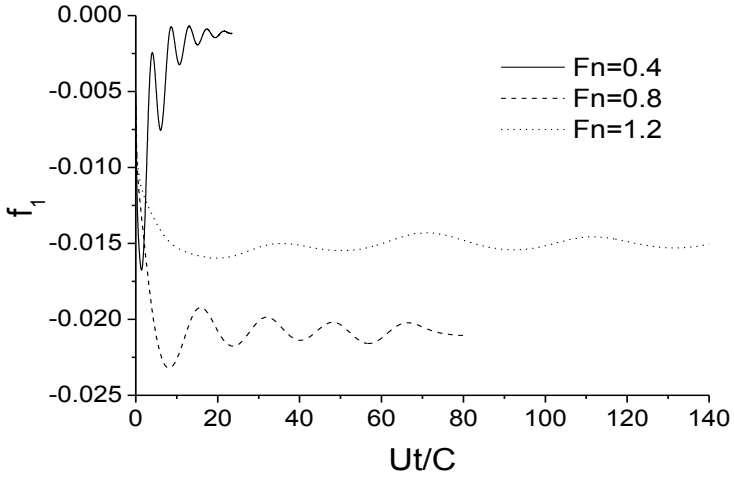

(a)

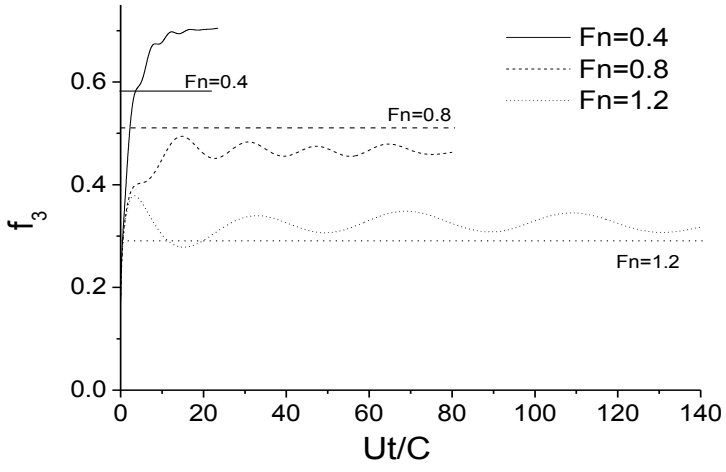

(b)

Figure 5.4 to be continued on next page

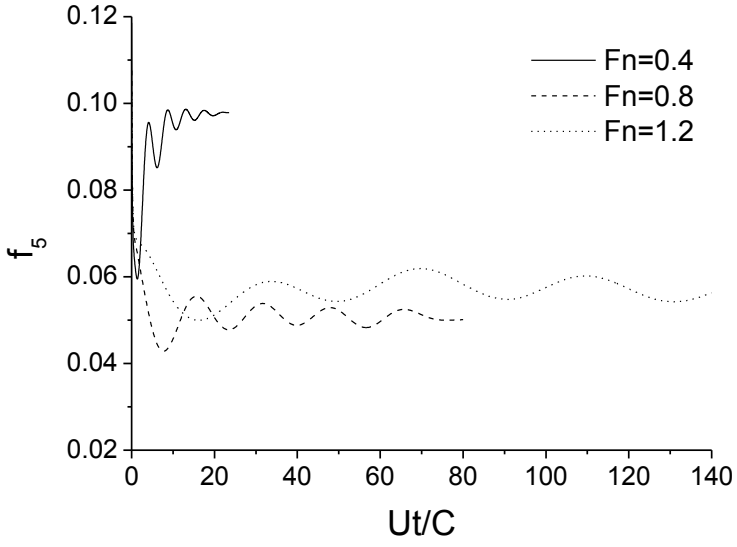

(c)

Figure 5.4 The (a) resistance, (b) lifting force and (c) moment on NACA 0012 at different velocity with $h_C / C = 1.0$, $\beta = 5^0$.

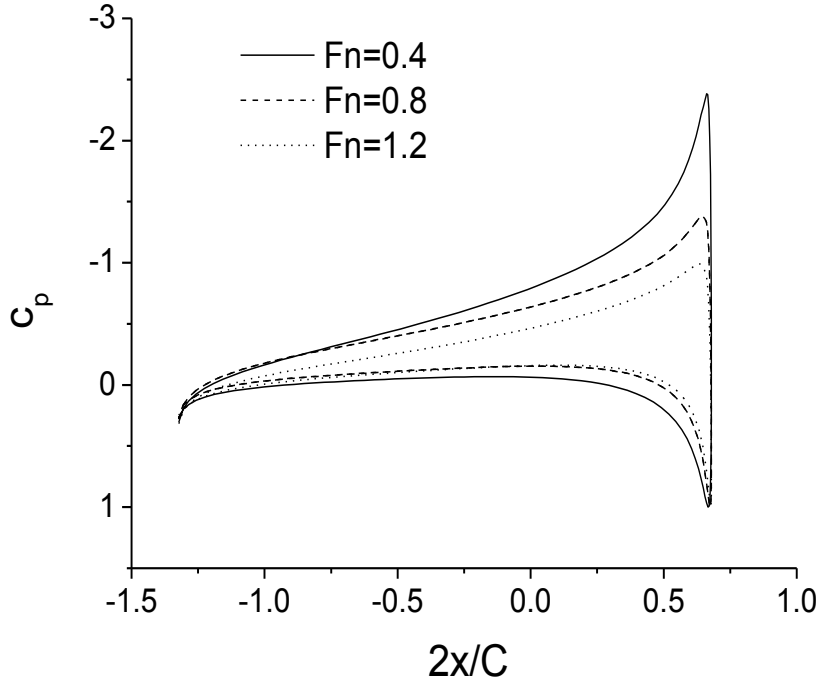

Figure 5.5 Pressure distribution on the foil under $h_C / C = 1.0$, $\beta = 5^0$ with $Fn = 0.4,\ 0.8,\ 1.2$ and $Ut / C = 23,\ 80,\ 140$ respectively.

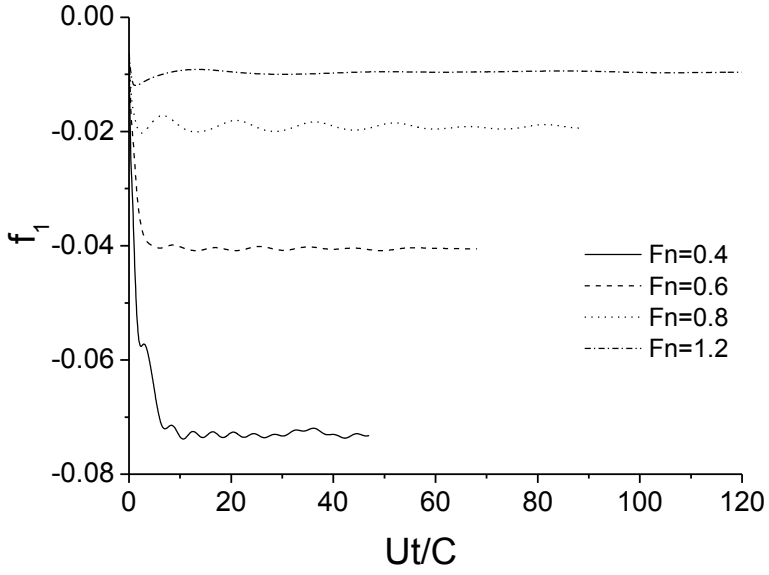

(a)

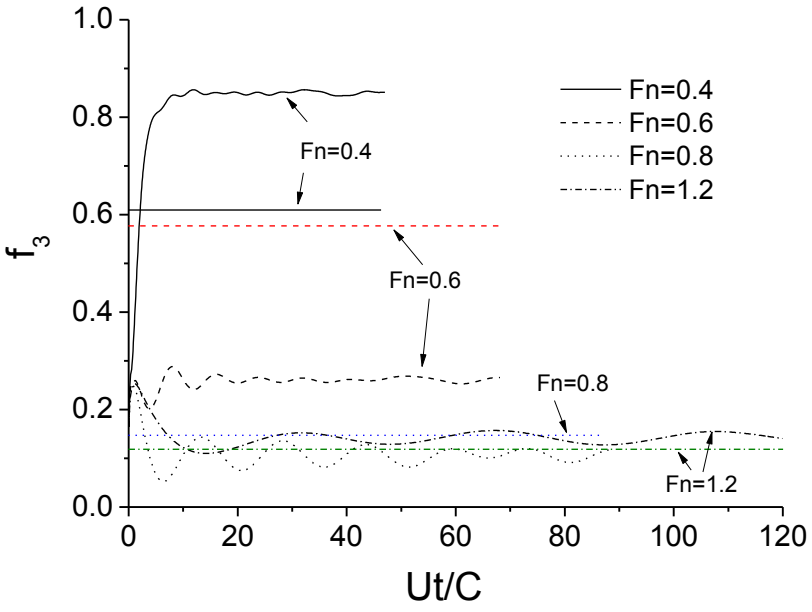

(b)

Figure 5.6 Continued on next page

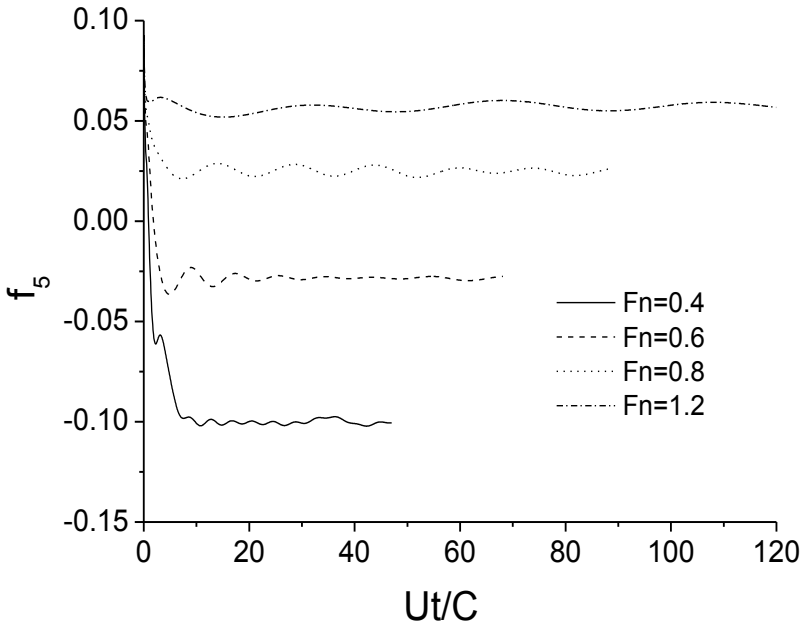

(c)

Figure 5.6 The resistance, lifting force and moment on NACA 0012 at different velocity with $h_C / C = 0.5$, $\beta = 5^0$, the flat straight line in (b) is from the linear theory. (a) F_1 (b) F_3 (c) F_5

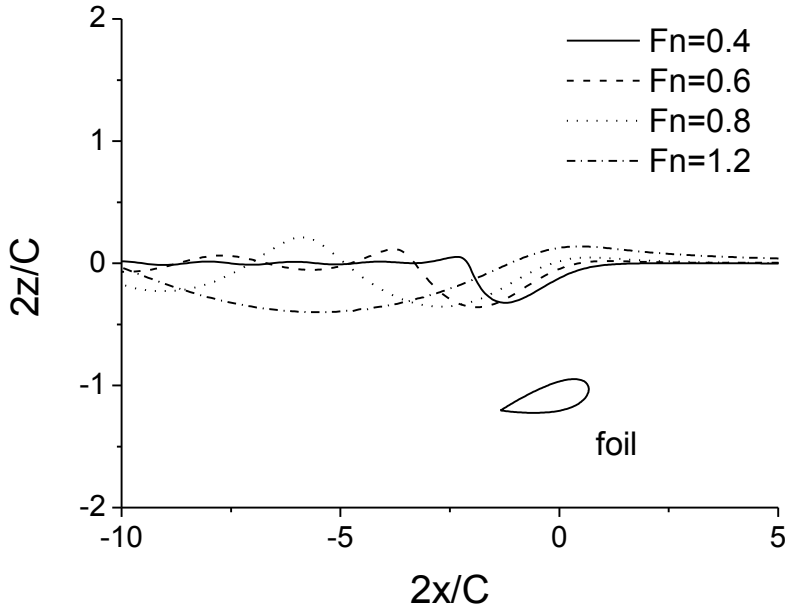

Figure 5.7 Highlight of the local free surface profile

We further reduce the submergence to $h_C / C = 0.5$. The simulation on the transient fully coupled problem of foil, free surface and vortex wake is carried out. The transient forces on the foil at $Fn = 0.4,\ 0.6,\ 0.8,\ 1.2$ are shown in figure 5.6. The resistance and the moment decrease as Fn increases; the lifting force decreases when Fn increases from 0.4 to 0.8. However, the lifting force at $Fn = 1.2$ increases. We also notice that the lifting force by the present method is very different with that based on the linear free surface theory in chapter 3. The lifting force coefficient of the present simulation at $Fn = 0.6$ is around 0.27, which is almost half of that from linear free surface theory. While the lifting force coefficient at $Fn = 0.4$ is around 0.85, which is much higher than that from the linear free surface theory. This would again be due to the coupled effect of the nonlinear free surface and vortex wake. More details on the nonlinear wave effect will be investigated.

Figure 5.7, shows the local wave profiles at $Fn = 0.4,\ 0.6,\ 0.8,\ 1.2$ when the foil travels a distance at $Ut / C = 45,\ 63,\ 88,\ 120$ respectively. There is a leading wave starting with a downwash of the free surface above the foil, which is followed by a smaller amplitude wave. When $Fn = 0.4$ is considered, the downwash of the first wave is significantly larger than the following wave, and the wave profile rises up to its crest just above the foil. The downwash free surface flow at $Fn = 0.4$ is actually confined to a small area near the leading edge; and it becomes an uprising flow above the trailing edge of the foil. The surface flow actually increases the effective attack angle when $Fn = 0.4$. This explains the higher lifting force. Linear free surface theory is valid when the ratio of wave amplitude and wave length are small, or $\frac{A_0}{\lambda_w} < 0.05$. As shown in Fig.5.7, $\frac{A_0}{\lambda_w}$ is not a small value and the linear free surface green function may give

inaccurate results. The free surface profile is definitely nonlinear and its full effect cannot be included by the linear free surface theory. The downwash of wave profile at $Fn = 0.6,\ 0.8,\ 1.2$ affect the lifting forces in a different way as the wave length becomes longer. When $Fn = 0.8$, for example, the effective attack angle decreases due to the downwash of the free surface. Generally the overall hydrodynamic force on the foil is significantly affected by the free surface flow.

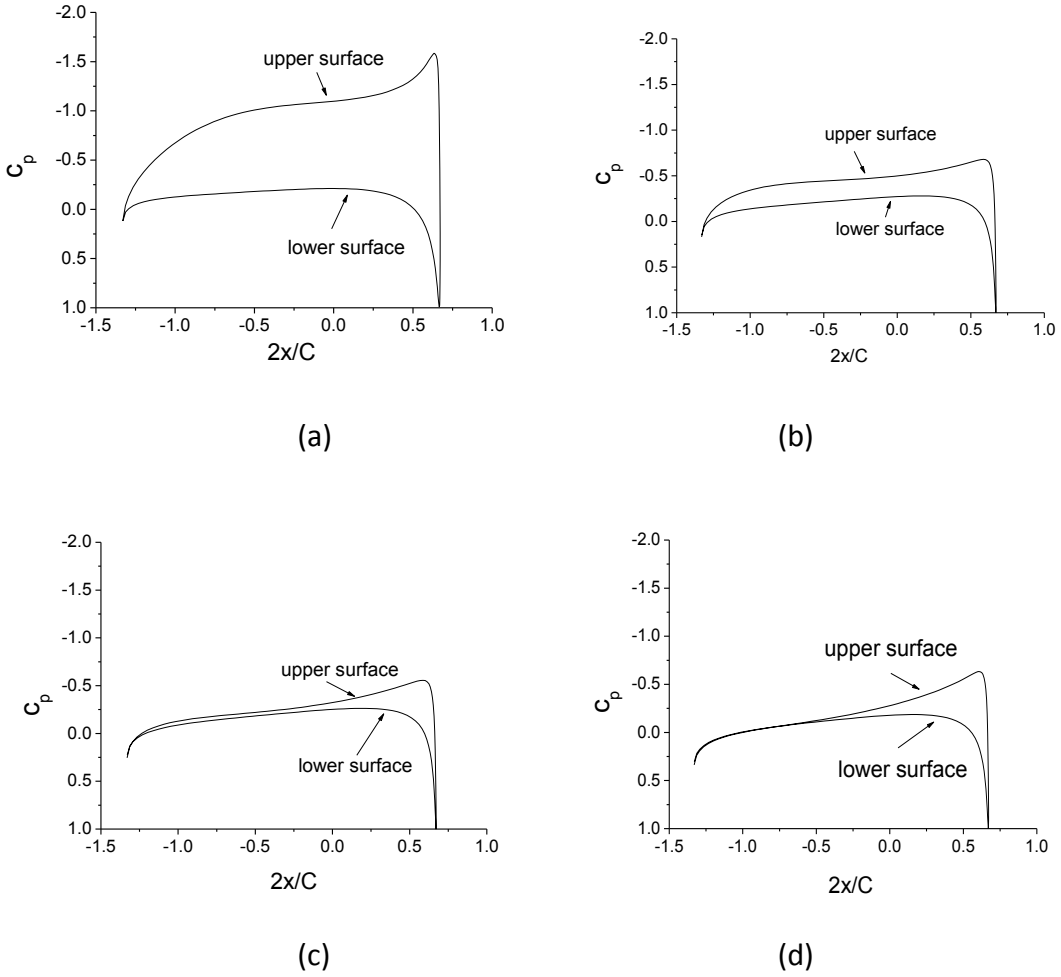

Figure 5.8 Pressure distribution on the foil under $h_C / C = 0.5$, $\beta = 5^0$, (a) $Fn = 0.4$, $Ut/C = 45$ (b) $Fn = 0.6$, $Ut/C = 63$ (c) $Fn = 0.8$, $Ut/C = 88$ (d) $Fn = 1.2, Ut/C = 120$

The pressure distributions on the foil provide further details, as shown in figure 5.8. The pressures on the lower surface are similar as shown in figure 5.8 (a) (b) (c) & (d).

However, the upper surface pressure decreases as the Froude number increases. Therefore the difference of the pressure coefficient on the upper and lower surface becomes smaller. We notice that the pressure of the upper and lower surface are almost the same on the aft body at $Fn = 1.2$. The pressure distribution gives good explanation of the overall force in figure 5.6.

5.2.2 Nonlinear free surface effect on an oscillatory foil

We consider the wave effect on the oscillatory foil. The transient free surface effect on the hydrodynamics of a foil in steady motion is significant. However the nonlinear free surface effect for a foil with small or large amplitude oscillatory motion is not clear enough. Would the wave effect improve the propulsive efficiency sometimes? Will the 'mirror effect' (Wu 1994, 2000) remain the same as for those in the unbounded flow? Here we will first simulate the small amplitude oscillatory motion, and then the simulations are carried out at various submergences and Froude number with large amplitude oscillatory motion. The free surface effect on the propulsion, energy harvesting and flying modes will be investigated.

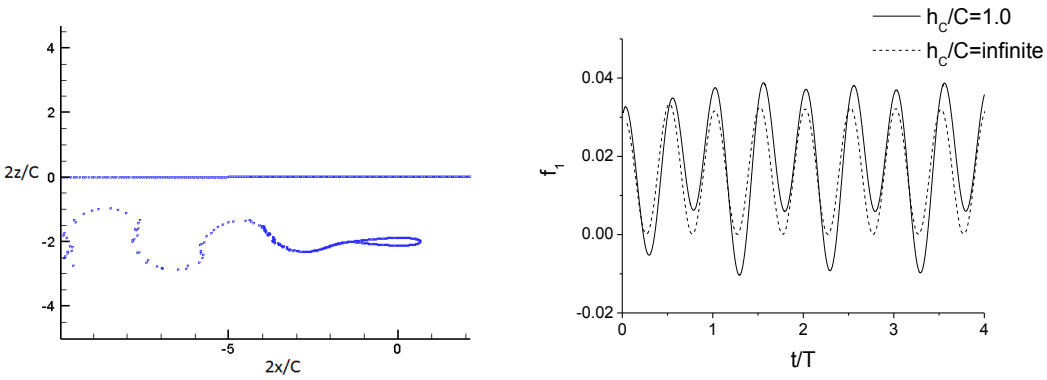

(a) (b)

Figure 5.9 To be continued on next page

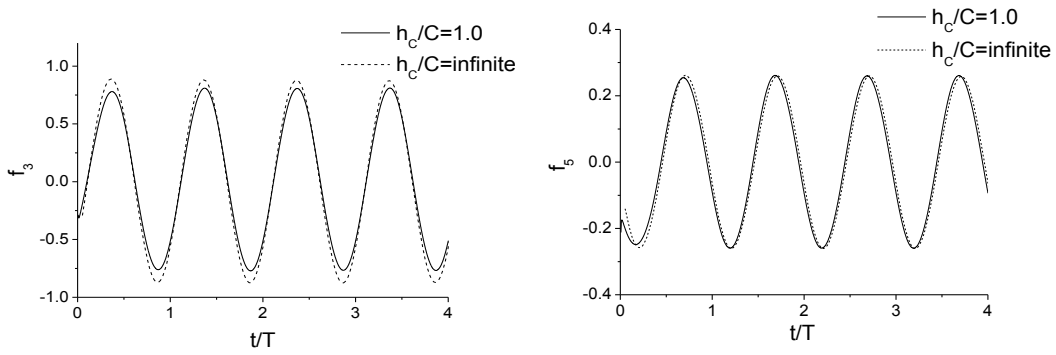

(c) (d)

Figure 5.9 The shed vortices and the force history under $h_C / C = 1.0$, $St = 0.05$, $h_0 / C = 0.05$, $\theta_0 = 0$, $Fn = 0.22576$

We first study the wave effect on the small amplitude vertical motion with submergence $h_C / C = 1.0$ under $Fn = 0.22576$, $St = 0.05$, $h_0 / C = 0.05$, $\theta_0 = 0$ $\beta = 0$. The vortex structure behind the foil at $t / T = 4.0$ is shown in figure 5.9(a). The vortices move up and down as the vertical oscillatory motion. The horizontal force history, as shown in figure 5.9(b), has two peaks and troughs in each period. However, compared with the results in the unbounded flow in each period, the peaks are higher; and the first trough is higher and the other, corresponding to the top position of the foil, is lower. This indicates that the procedures of Wu (1994, 2000) would not be applicable here due to asymmetry of the flow about its mean position due to the wave effect. The surface wave radiation would induce downwash or uprising of the flow. Compared with the result in unbounded flow, the vertical force has smaller amplitude, however the moment is very close, as shown in figure 5.9(c) & (d). The peak value of the vertical force is slightly higher than the absolute value of troughs, which means there is a small steady suction force. The overall performance of the foil is shown in table 5.1. Compared with the results in unbounded flow, the thrust coefficient is slightly higher and the input power is slightly lower, therefore lead to a higher propulsive efficiency.

We shall note that the propulsive efficiency may decrease when different submergences and frequencies are considered.

Table 5.1 The performance of the foil under $St = 0.05$, $h_0 / C = 0.05$, $\theta_0 = 0$, $\beta = 0$

	c_T	c_P	η_T
$h_C / C = 1.0$	0.0178	0.0418	0.426
$h_C / C = \infty$	0.0157	0.0437	0.359

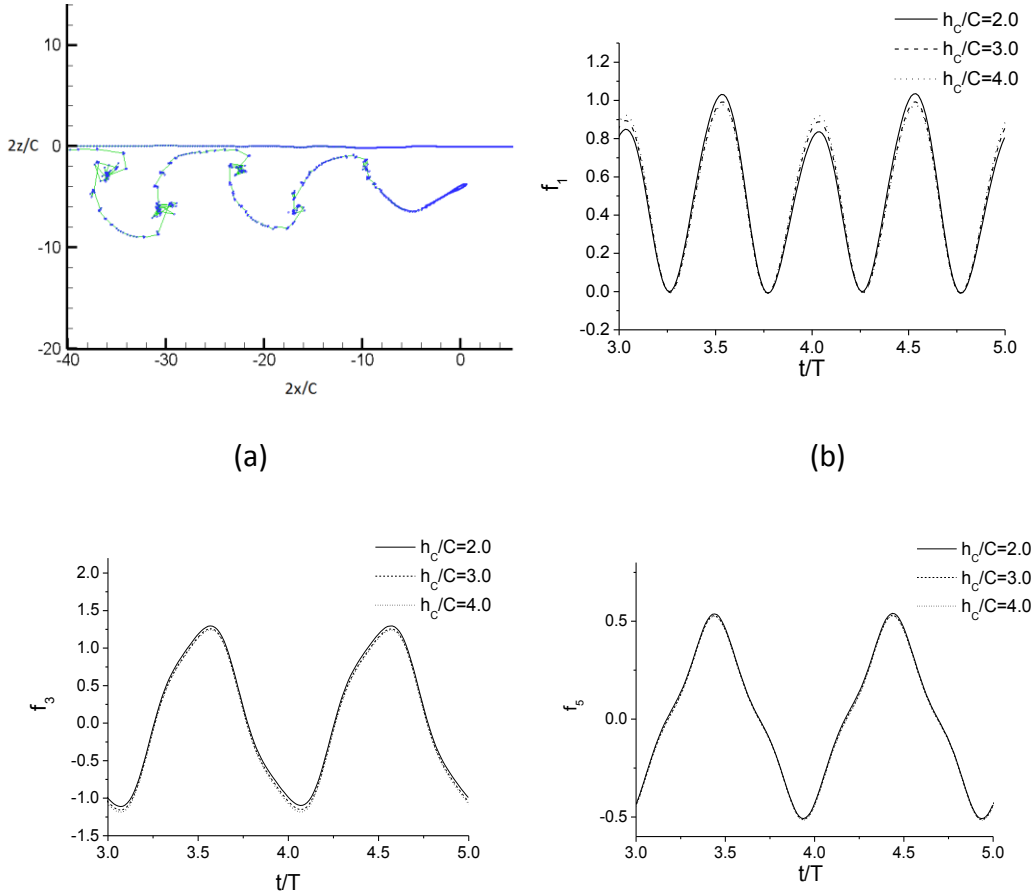

Figure 5.10 Vortex structure and the force histories on the foil at various submergence under $h_0 / C = 1.0$, $St = 0.3$ $\alpha_0 = 15^0$, $Fn = 0.8$, $\varepsilon = 75^0$, $\beta = 0$ (a) vortex structure at $t / T = 4.0$ with $h_C / C = 2.0$ (b) F_1 (c) F_3 (d) F_5

Let us consider larger amplitude vertical and rotational oscillatory motion of the foil

near the water surface. The propulsive mode with various submergences $h_C / C = 2.0$, $h_C / C = 3.0$ and $h_C / C = 4.0$ at $Fn = 0.8$ under $h_0 / C = 1.0$, $St = 0.3$ $\alpha_0 = 15^0$ $\beta = 0$ are considered first. As shown in figure 5.10(a), the vortices are very close to the free surface after the vortices move a distance behind the foil. The simulation may break down if the vortices penetrate the free surface due to numerical instability. This is the limitation of the present simulation. Therefore the submergence of the foil cannot be too small; and the gap between the mean free surface and the top position of the foil shall be large enough. The horizontal force, as shown in figure 5.10(b), is not a sinusoidal function of double frequency of the motion; the two peaks in each period are slightly different. When the foil is leaving the mean position upwards when $t \approx iT$, the peak value of the horizontal force is a bit smaller when compared with the peak value when it is leaving the mean position downwards when $t \approx (i + 0.5)T$, where i is a positive integer number. When the submergence increases, the higher peak decreases and the lower peak increases slightly, which results in a smaller difference of the two peaks in one period. It is expected that when the submergence of the foil becomes very large, the value of these two peaks shall be equal. We also notice that the troughs of the horizontal force are not significantly affected by the submergence. As shown in figures 5.10 (b) & (c), the absolute value of the peak is larger than the absolute value of the troughs, which means the mean value is larger than zero. There would be a constant lifting force and moment on the foil when it is decomposed by Eq.(4-17). Table 5.2 gives the coefficients of these decomposed forces for $h_C / C = 2.0$. Generally, the coefficients are very close to those in the unbounded flow. We have $b_0 = 0.0894$ for the mean vertical force, which is the mean value of the 'suction force' due to the free surface effect. There is a constant term for the moment too. The overall

performance in terms of propulsion is given in table 5.3. The mean thrust and input power at $h_C / C = 2.0$ is slightly smaller when compared with those in the unbounded fluid. However the propulsive efficiency is very close to that in the unbounded fluid. The effect of free surface is insignificant against submergence at $Fn = 0.8$, $h_C / C = 2.0$.

Table 5.2 The decomposition of the forces with $h_C / C = 2.0$, $St = 0.3$, $h_0 / C = 1.0$, $\alpha_0 = 15^0$, $\varepsilon = 75^0$, $\beta = 0$

	b_0	a_1	b_1	a_2	b_2	a_3	b_3	a_4	b_4
$f_1, \frac{h_C}{C} = 2$	0.486	-0.007	-0.093	0.141	0.446	-0.003	-0.003	0.012	-0.031
$f_1, \frac{h_C}{C} = \infty$	0.499	0.000	0.001	0.1550	0.463	0.000	0.000	0.012	-0.031
$f_3, \frac{h_C}{C} = 2$	0.089	-0.214	-1.169	0.001	0.009	-0.079	0.082	0.001	-0.002
$f_3, \frac{h_C}{C} = \infty$	-0.001	-0.217	-1.218	0.000	0.000	-0.080	0.082	0.000	0.000
$f_5, \frac{h_C}{C} = 2$	0.016	0.179	-0.421	0.001	0.000	0.058	0.030	0.001	0.001
$f_5, \frac{h_C}{C} = \infty$	0.000	0.167	-0.403	0.000	0.000	0.056	-0.027	0.000	0.000

Table 5.3 The performance of the hydrofoil under $h_C / C = 2.0$, $St = 0.3$, $h_0 / C = 1.0$, $\alpha_0 = 15^0$, $\varepsilon = 75^0$, $\beta = 0$

	c_T	c_P	η_T
$h_C / C = 2.0$	0.486	0.584	0.832
$h_C / C = \infty$	0.501	0.606	0.826

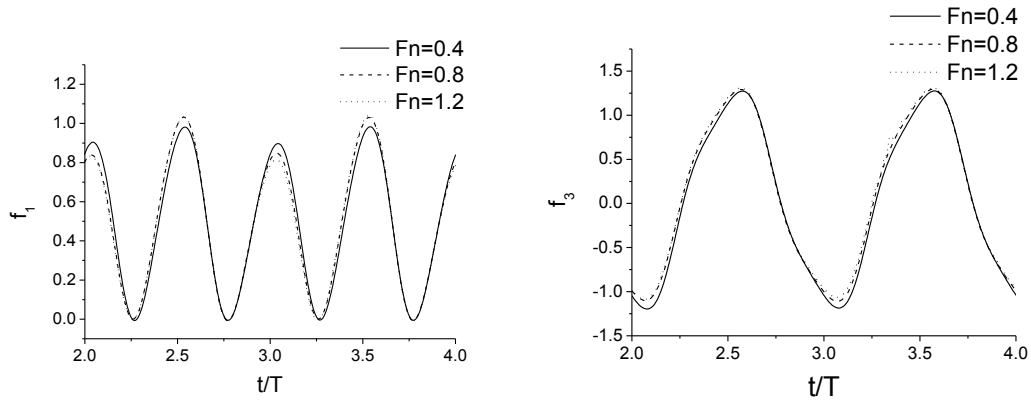

(a) (b)

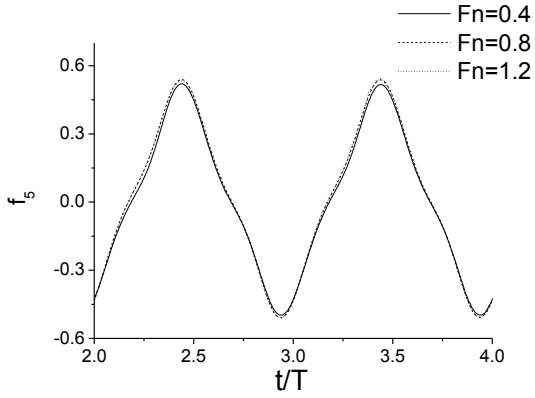

(c)

Figure 5.11 The forces histories of the foil with different Fn under $h_C / C = 2$,

$h_0 / C = 1.0$, $St = 0.3$ $\alpha_0 = 15^0$, $\varepsilon = 75^0$, $\beta = 0$

Table 5.4 The overall performance of the foil with different Fn under $h_C / C = 2$,

$h_0 / C = 1.0$, $St = 0.3$ $\alpha_0 = 15^0$, $\varepsilon = 75^0$, $\beta = 0$

	c_T	c_P	η_T
$Fn = 0.4$	0.481	0.581	0.8282
$Fn = 0.8$	0.486	0.584	0.8323
$Fn = 1.2$	0.481	0.582	0.8270

We then study the propulsion of this foil at different Froude number Fn. We run the simulation with $h_C/C=2.0$, $h_0/C=1.0$, $St=0.3$, $\alpha_0/C=15^0$, $\varepsilon=75^0$, $\beta=0$ at $Fn=0.4$, $Fn=0.8$, $Fn=1.2$ respectively. The force history is shown in figure 5.11. Again, we can see from the figure that the absolute values of the two peaks in each period are slightly different when the foil is moving away from the mean position upwards and downwards. When the Froude number increases, an increase of the higher peak and decrease of the lower peak can be observed. We note that the frequency of the oscillatory motion increases with Fn when St is fixed. The free surface effect becomes more obvious when Fn increases. Figures 5.11 (b) & (c) show the vertical force and moment; these curves are slightly affected as Fn increases. It can be observed that the troughs of the vertical force move up slightly when the foil is leaving its mean position upwards. Table 5.4 gives the overall performance of the foil at different Fn. The thrust coefficient, input power and the propulsive efficiency are very close when different Fn are considered, although there are slight differences in the force histories in figure 5.11. This means that Fn has limited influence to the propulsion of an oscillatory foil at $h_C/C=2.0$.

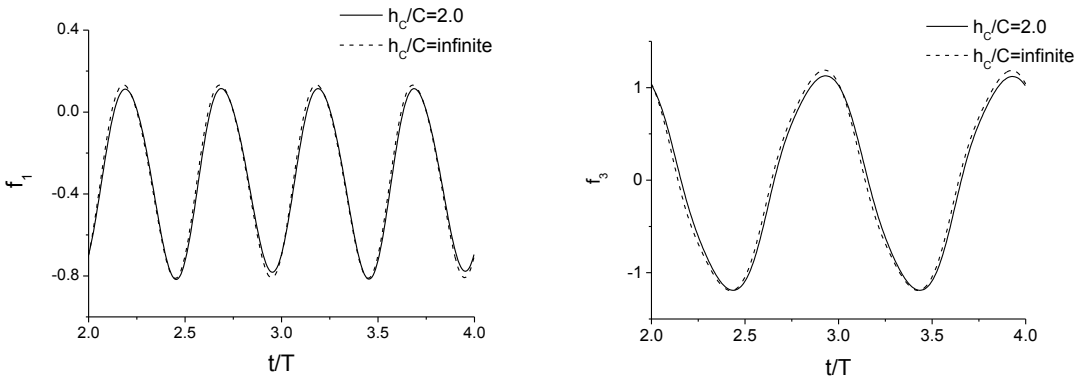

(a) (b)

Figure 5.12 To be continued on next page

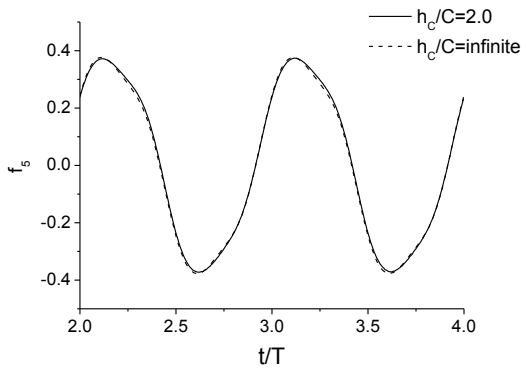

(c)

Figure 5.12 Force history under $Fn = 0.4$, $h_C / C = 2.0$, $h_0 / C = 1.0$, $St = 0.2$, $\alpha_0 = -10^0$, $\varepsilon = 90^0$, $\beta = 0$

Table 5.5 The performance of the foil with $Fn = 0.4$, under $h_C / C = 2.0$, $h_0 / C = 1.0$, $St = 0.2$, $\alpha_0 = -10^0$, $\varepsilon = 90^0$, $\beta = 0$

	c_D	c_{PL}	c_{PO}
$h_C / C = 2.0$	0.326	0.316	0.279
$h_C / C = \infty$	0.319	0.305	0.269

The energy harvesting mode under the free surface is simulated next. Computation is carried out at $h_C / C = 2.0$ under $h_0 / C = 1.0$, $St = 0.2$ $\alpha_0 = -10^0$, $\varepsilon = 90^0$, $\beta = 0$. Figure 5.12 shows the time history of the foil, which is very close to that when $h_C / C = \infty$. However, there is a visible difference when the foil is moving away from the mean position and approaching the water surface in figures 5.12(a) & (b). Table 5.5 shows the resistance coefficient c_D, power coefficient from lifting force c_{PL} and the total power coefficient c_{PO}. The free surface effect makes very small difference as shown in the table.

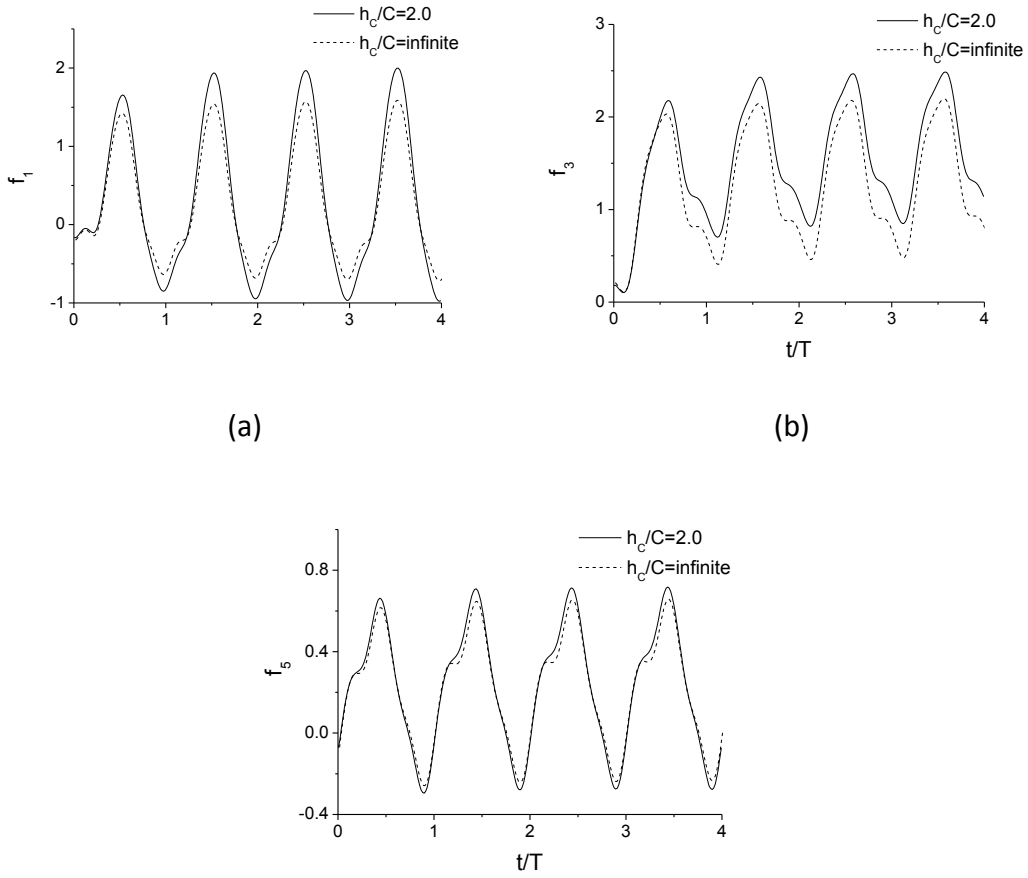

Figure 5.13 Force history with $Fn = 0.4$, $h_C / C = 2.0$, under $h_0 / C = 1.0$, $St = 0.3$, $\alpha_0 = 10^0$, $\beta = 10^0$, $\varepsilon = 75^0$, $\beta = 0$.

We further simulate the flying mode. The Froude number Fn is found to have important effect on the hydrodynamic force as the foil is in steady motion, especially when $Fn = 0.4$. Then simulation for the flying mode is carried out with $Fn = 0.4$, $h_C / C = 2.0$ under $h_0 / C = 1.0$, $St = 0.3$, $\beta = 5^0$, $\alpha_0 = 10^0$, $\varepsilon = 75^0$. Figure 5.13 presents the force histories. Compared with the results in the unbounded flow, the amplitude of the horizontal force is larger; and the overall lifting force is larger, the amplitude of the moment is slightly higher too. It is expected that the increase of lifting force is mainly due to the free surface wave of certain wavelength, similar to that in section 5.3.1. The overall performance for propulsion, which is measured from $t = 3T$

till $t = 4T$, is presented in table 5.6. Compared with that in the unbounded flow, the thrust coefficient is higher; however the input power coefficients are similar. The propulsive efficiency, therefore, is higher than that in unbounded flow. The reason would be very complicated since the free surface flow, vortex wake are involved. Although only one case of flying mode is studied here, we can expect that the propulsive efficiency will vary due to the wave effect when different forward speed and submergence are considered.

Table 5.6 The performance of the foil with $Fn = 0.4$, $h_C / C = 2.0$, under $h_0 / C = 1.0$, $St = 0.3, \beta = 10^0, \alpha_0 = 10^0, \varepsilon = 75^0, \beta = 5^0$

	c_T	c_P	η_T
$h_C / C = 2.0$	0.3164	0.3932	0.805
$h_C / C = \infty$	0.2625	0.4083	0.643

Chapter 6 The vortex shedding at the orifice of a floating compartment

6.1 Introduction

Ships can be damaged by an accident (collision, grounding, structural failure, fire). In most cases, the orifice caused by damage is either at the bottom or on the side of the ship. If the damage is below the waterline, the compartment is then flooded. The static and dynamic stabilities will be very different from those of the intact ship, because the meta-centre and the floating centre will change. An understanding of the hydrodynamics of the damaged ship will be highly important to the emergency response system (ERS) and salvage, as well as in the assessment of its capability of remaining operation. Guidelines for design and ERS planning and decision support systems, which will avoid risky operation and help the survival of the passengers, crew and ship will be based on the study of hydrodynamic loads. The present study focuses on the wave radiation of a flooded compartment with a bottom orifice. The hydrodynamic force and ingress/egress flow will be investigated.

Vortices shed at the orifice of a flooded compartment can be expected and have been observed (Smith 2009). The vortices move in and out along with the ingress and egress flow when the compartment is in forced heave motion. The vortex shedding at the orifice in the unbounded flow has been studied in chapter 4, as an example of using the developed methodology. The shed vortices significantly affect the local flow near the orifice. Damping effect due to vortices has been documented. Pure potential flow, which does not include the vortex shedding, cannot capture the characteristics of the flow with vortices. Discrepancy between the experimental data and the simulation results from pure potential flow theory for a flooded damaged compartment at lower

frequency has been reported by Smith (2009). The typical inviscid flow around a plate is inaccurate without vortex shedding (Lamb, 1932). When the flow around an orifice of a floating body is considered, besides the tracking of free surface, the shed vortices shall be incorporated properly.

We focus on the vortex shedding at the orifice of a floating oscillatory compartment in this chapter. A compartment with bottom orifice in initially calm water, which is to model a section of a damaged ship, is simulated. Harmonic vertical (heave) motion is prescribed. The free surface deformation together with vortex shedding at the orifice is tracked using the time stepping method. The numerical vortex shedding scheme, which has been used in the last two chapters, is applied. As the radiated wave propagates towards the control surface, a damping zone the same as that in chapter 5 is used to absorb the wave; the velocity and wave elevation are reduced through artificial damping parameters. The hydrodynamic force and the flow through the orifice will be analysed and discussed.

6.2 Description of the simulation for a flooded compartment

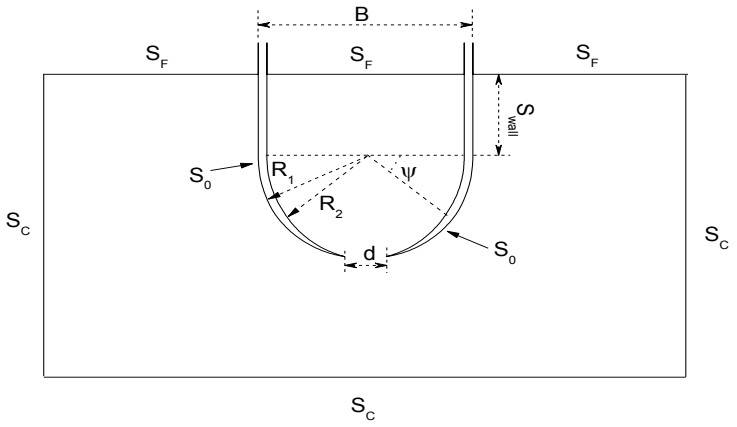

Figure 6.1 The sketch of a damaged compartment

The governing equation and the boundary conditions are the same as those in chapter 2 and chapter 5, when the forward speed is taken as zero. To simulate the vortex shedding of a flooded compartment, a few numerical treatments are required, such as the geometrical modelling of the compartment and damping of vortices.

Following the successful simulations on the vortex shedding of the submerged foil near the free surface in chapter 5, the continuous vortex shedding procedures from the sharp edge will be again applied to the problem of an oscillatory surface piercing floating structure here. Figure 6.1 shows the sketch of the problem of a damaged compartment with a bottom orifice. The thickness of the structure is included in the model. As shown in the figure, the geometry of the compartment in this example is constructed by a semi-circular cylinder and vertical side walls. The thickness of the side wall is the difference between the outer surface with radius R_1 and inner surface with radius R_2 of the circular column. To adapt to the vortex shedding scheme, we shall make the edge of the orifice a thin sharp corner. A linear function is introduced to let the inner and outer surface of the compartment join to form a sharp angle. Thus the thickness of the structure decreases gradually and becomes zero at the orifice edge. Mathematically, we can write the modified radius as

$$\tilde{R}_1(\psi)=\begin{cases} R_1, \ \psi \notin (\psi_{start},\psi_{end}) \\ \dfrac{\Delta\psi}{\psi_0}R_1+\dfrac{1}{2}(1-\dfrac{\Delta\psi}{\psi_0})(R_1+R_2), \ \psi \in (\psi_{start},\psi_{end}) \end{cases} \tag{6-1}$$

$$\tilde{R}_2(\psi)=\begin{cases} R_2, \ \psi \notin (\psi_{start},\psi_{end}) \\ \dfrac{\Delta\psi}{\psi_0}R_2+\dfrac{1}{2}(1-\dfrac{\Delta\psi}{\psi_0})(R_1+R_2), \ \psi \in (\psi_{start},\psi_{end}) \end{cases} \tag{6-2}$$

where $\psi_0=\psi_{end}-\psi_{start}$, $\Delta\psi=\psi-\psi_{start}$ and ψ_{end} is the angle at the orifice edge.

We choose $\dfrac{\pi}{6}<\psi_0<\dfrac{\pi}{3}$; if it is not specified, $\psi_0=\dfrac{\pi}{4}$ is used.

The size of the element is chosen at $0.02B$ on the free surface; it increases with the distance to the compartment, and the maximum element shall be less than $0.05\lambda_w$. Eq.(5-1) is used and C in the equation is replaced by the breadth of the compartment B. As the radiated wave propagates to the far field, the damping zone is adopted; Eqs.(5-2) & (5-3) are used and the control surface is chosen at $x = \max(10B,\ 10\lambda_w)$.

6.3 Numerical results and discussions

6.3.1 Comparison with experiment data

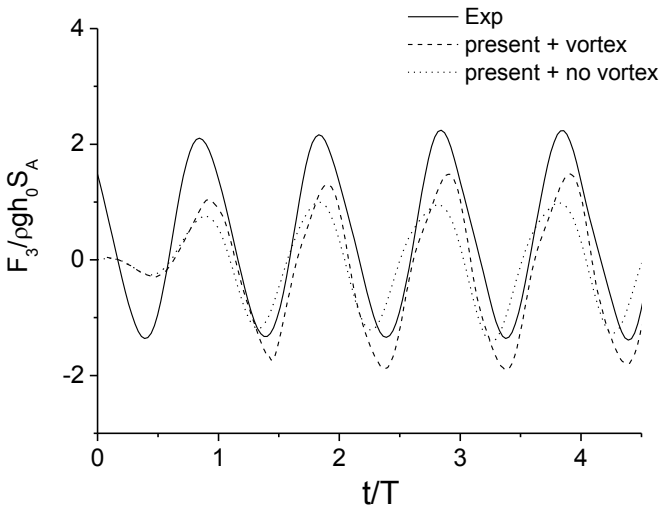

Figure 6.2 Vertical force on the compartment, $f = 1.333Hz$, $R_1 = 0.1575m$, $R_2 = 0.1495m$, $d = 0.07m$, $s_{wall}/B = 0$, $h_0 = 0.04m$

We simulate a compartment with bottom orifice with $d/B = 0.27$, $f = 1.333Hz$. Eq.(4-31) is used to prescribe the motion of the compartment and $i = 2$ is used. To damp the vortices, Eq.(4-32) is adopted. The force history is compared with the experimental data provided by Daniel Fone through personal communication. The model is the same one used by Smith (2009), as shown in Fig. 2. Compared with the experimental data, the peak value and the trough value of present simulation are lower than that of the experimental data, as shown in figure 6.2. However the elevation from

the trough to peak is close. The present numerical simulation results ignore the gravity of the fluid. In the experimental data, the mean hydrostatic force has been excluded while the effect due to the change of the free surface inside and outside the compartment is not excluded from the original data; we also notice that the thickness of the sidewall above the mean free surface is 20 millimetre, which is much larger than the circular column part. Considering this fact, the simulation result is acceptable. The simulation result without vortex shedding is shown in the figure as well. The force amplitude is smaller than the results including vortex shedding. We will adopt the numerical scheme to study the characteristic of the damaged compartment.

6.3.2 Characteristics of vortex shedding at the orifice

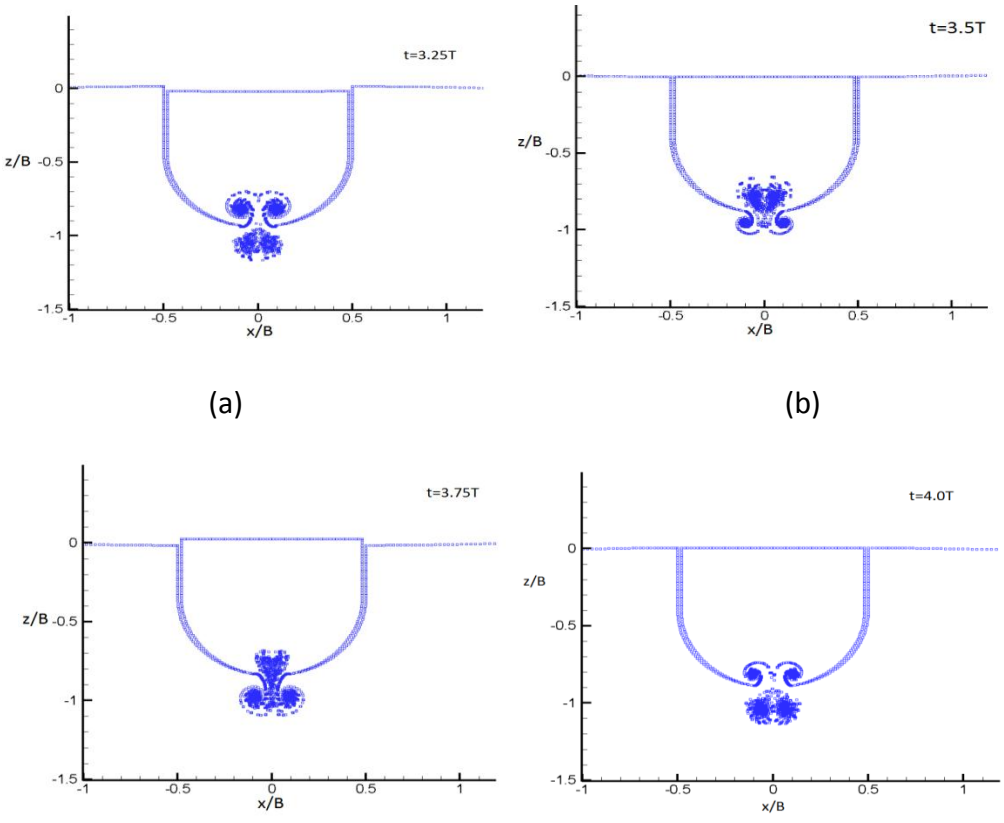

(a) (b)

(c) (d)

Figure 6.3 The vortices under $d/B=0.2$, $s_{wall}/B=0.4$, $f=1.0Hz$, and $h_0/B=0.05$ (a) $t/T=3.25$, (b) $t/T=3.5$,(c) $t/T=3.75$,(d) $t/T=4.0$

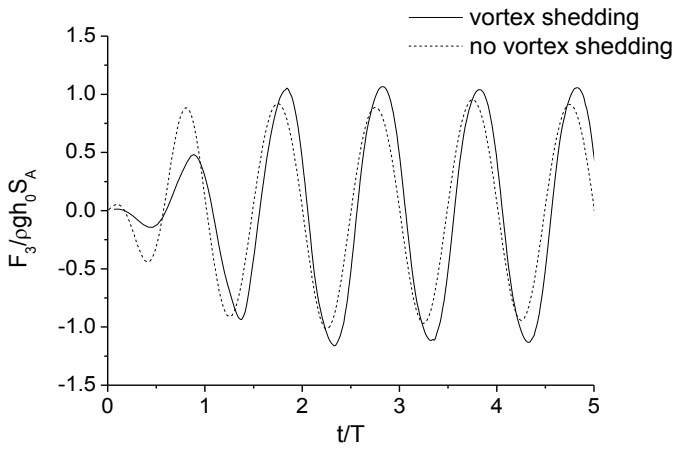

Figure 6.4 The vertical force on the compartment under $d/B=0.2$, $s_{wall}/B=0.4$, $f=1.0Hz$, and $h_0/B=0.05$

Table 6.1 The coefficient of decomposed force of figure 6.4

	b_0	a_1	b_1	a_2	b_2	a_3	b_3	a_4	b_4
Vortex	-0.0330	-1.0314	0.4430	0.0088	0.0012	-0.0351	0.0348	0.0010	-0.0005
No vortex	0.0037	-0.9473	0.0069	0.0007	0.0299	0.0003	-0.0005	0.0001	-0.0003

To study the vortex shedding effect, simulations are carried out in sinusoidal motion with heave amplitude $h_0/B=0.05$ and frequency $f=1.0Hz$. Here we choose the orifice size $d/B=0.2$, side wall $s_{wall}/B=0.4$. Figure 6.3 shows the vortices at different times with a step of $T/4$ from $t=3.25T$ to $t=4T$. The vortices pairs move up / down along with the ingress / egress flow can be observed. The mean free surface inside the compartment is lower than that outside when the compartment passes its mean position and moves down; and the internal free surface is higher when the compartment moves upwards after passing its mean position, corresponding to the typical moment at $t/T=3.25$ and $t/T=3.75$, as shown in figures 6.3(a) & (c). The strength of the vortices and the flow through the orifice would not be as strong as those in unbounded flow when there is free surface; however, it is expected that the

vortex structure is quite similar although the orifice size, motion frequency and frequency are different. The time history of the vertical force, as shown in figure 6.4, is periodical after two cycles since $i = 2$ has been used in Eq.(4-31). The amplitude of the force predicted by the present vortex shedding scheme is larger than that of the pure potential theory, and phase difference between them can be observed. We further decomposed the force using Eq.(4-17) and the coefficients are given in table 6.1. The leading term is the first order force; the values of a_1 from these two curves, which are related to the acceleration or the added mass, are similar. However the value of b_1, which is related to the velocity of the compartment or the damping coefficient, from vortex shedding model is larger than that from pure potential flow. This is consistent with the fact that vortex shedding mainly affects the velocity or damping term.

The ingress/egress flow is the concern of the present study. The volume of the flow and the flow rate through the orifice are shown in figure 6.5. The non-dimensional flow rate is defined as

$$q_e = \frac{dV_e}{dt}\frac{B}{\omega h_0 d},\ V_e = \frac{V_{in}}{B} \tag{6-3}$$

where V_{in} is the volume of ingress water.

The ingress/egress volume V_e predicted by models with/without vortex shedding has an obvious discrepancy at the starting period, when the compartment starts to move with smaller amplitude motion as described in Eq.(4-31). During the following periods, the flow rates q_e predicted by these two models are close although an obvious difference at the starting period can be seen. Generally, their phases are close to the phase of the motion; the variations of volume V_e and flow rate q_e follow the variation of acceleration and velocity of the compartment respectively.

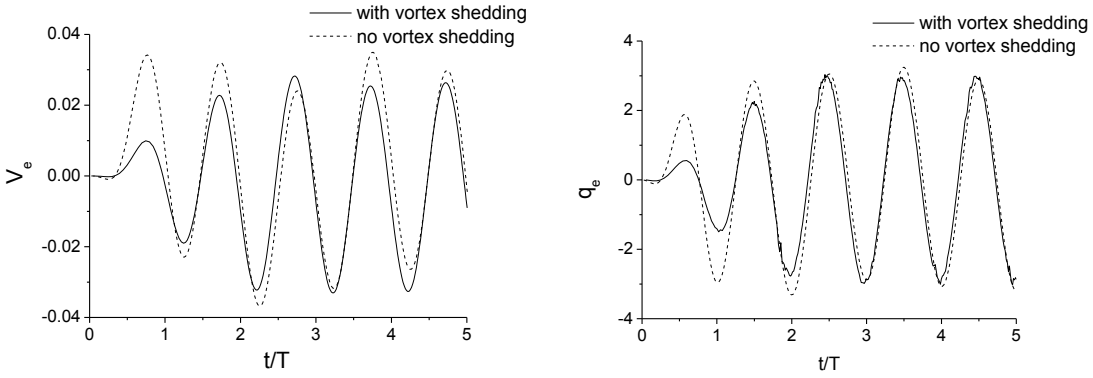

(a) (b)

Figure 6.5 The ingress/egress volume and the flow rate at the orifice with $d/B=0.2$, $s_{wall}/B=0.4$, $f=1.0Hz$, and $h_0/B=0.05$

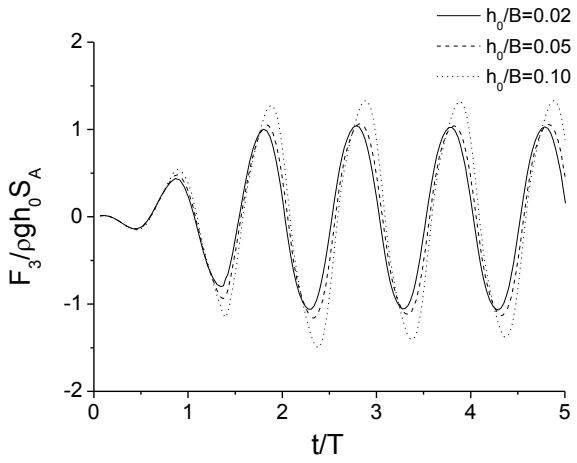

Figure 6.6 The effect of the heave amplitude on the vertical force with $d/B=0.2$, $s_{wall}/B=0.4$, $f=1.0Hz$

Table 6.2 The decomposed force for various h_0/B with $d/B=0.2$, $s_{wall}/B=0.4$, $f=1.0$

	b_0	a_1	b_1	a_2	b_2	a_3	b_3	a_4	b_4
$\frac{h_0}{B}=0.02$	-0.013	-1.057	0.196	0.003	0.007	-0.032	0.007	0.003	0.002
$\frac{h_0}{B}=0.05$	-0.033	-1.031	0.443	0.009	0.001	-0.035	0.035	0.001	-0.001
$\frac{h_0}{B}=0.1$	-0.028	-1.096	0.794	0.018	0.031	-0.079	0.057	0.004	0.004

The heave amplitude, size of the orifice, and the frequency would have a significant effect on the vortex shedding and the hydrodynamic force. Simulations are carried out by varying one parameter and others are fixed. The heave amplitude is considered first. We simulate the same compartment with different heave amplitudes $h_0 / B = 0.02$, $h_0 / B = 0.05$ and $h_0 / B = 0.1$ under $d / B = 0.2$, $s_{wall} / B = 0.4$, $f = 1.0Hz$. The vertical force histories are shown in figure 6.6. The non-dimensionalized force amplitude increases slightly as the heave amplitude. As these curves are decomposed using Eq.(4-17), the coefficients in table 6.2 show that the leading term is the first order components. The value of a_1 does not change much, while b_1 increases as the heave amplitude. b_1 is nearly proportional to the heave amplitude, which is different to that in the unbounded flow in section 4.3.2. It is expected that the increase of the heave amplitude results in larger relative motion of the fluid inside and outside of the compartment, therefore inducing stronger vortices and damping effect. The damping effect is the cross effect of wave radiation and vortex shedding.

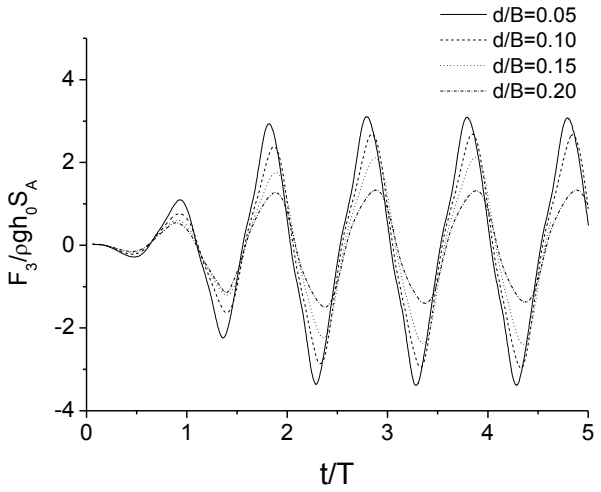

Figure 6.7 The force history on the compartment of various orifice size d / B with $f = 1.0Hz$, $h_0 / B = 0.1$, $s_{wall} / B = 0.4$.

Table 6.3 Decomposition of force of various orifice size in figure 6.7

	b_0	a_1	b_1	a_2	b_2	a_3	b_3	a_4	b_4
$\frac{d}{B}=0.05$	-0.063	-2.839	0.703	-0.058	0.102	0.138	-0.243	-0.026	-0.000
$\frac{d}{B}=0.1$	-0.065	-2.396	1.013	-0.023	0.154	-0.141	-0.220	-0.021	0.015
$\frac{d}{B}=0.15$	-0.050	-1.829	1.139	0.056	0.130	-0.170	-0.039	-0.001	0.020
$\frac{d}{B}=0.2$	-0.003	-1.095	0.794	0.017	0.031	-0.079	0.056	0.004	0.004

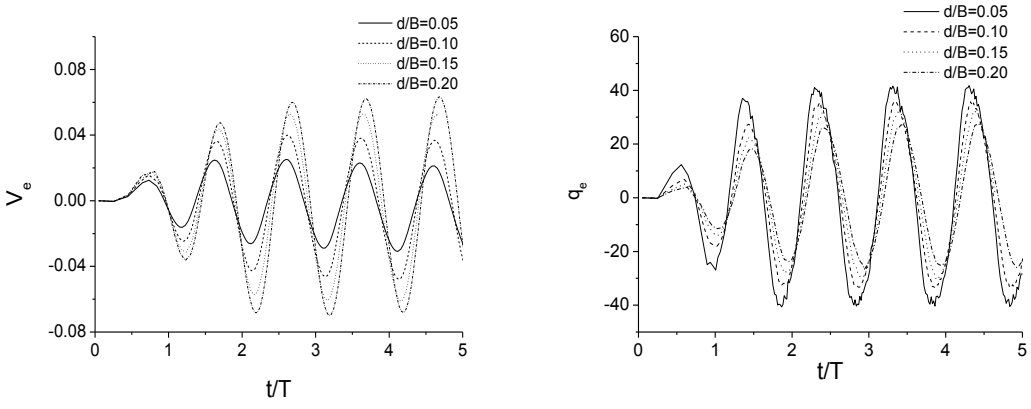

(a) (b)

Figure 6.8 (a) the ingress/egress volume and (b) the flow rate across the orifice

$$f=1.0Hz,\ h_0/B=0.1, s_{wall}/B=0.4$$

Simulations with different sizes of the orifice are carried out under $f=1.0Hz$, $h_0/B=0.1, s_{wall}/B=0.4$. As shown in figure 6.7, the non-dimensionalized vertical force decreases when the orifice size increases. The decomposed component coefficients of the vertical force are shown in table 6.3. The term b_0, which refers to the mean force, and term a_1 decrease as d/B increases. As expected, a larger orifice

means that the fluid can ingress/egress more easily. Consequently, there would be less fluid moving along with the compartment and the 'added mass' of the compartment decreases. b_1 , which refers to the damping term, increases with d/B and then decreases when the orifice size becomes larger. The damping effect due to vortex shedding becomes more significant with medium orifice size, which is consistent with that in section 4.3.2. In the table, we also notice the value of a_2 , b_2 , a_3 , b_3 appears as a secondary important component, especially at smaller d/B . Figure 6.8 gives the volume of the ingress/egress fluid and the flow rate across the orifice. As expected, the amplitude of V_e becomes larger when d/B increases. However, the amplitude of the flow rate q_e decreases. This indicates that the pressure difference of the inner and outer flow decreases when the orifice becomes larger. The equations to predict the flow rate based on the hydraulic model would be inaccurate based on the present simulation.

Table 6.4 The decomposed force for various frequency under $d/B=0.1$, $h_0/B=0.1$.

	b_0/f^2	a_1/f^2	b_1/f^2	a_2/f^2	b_2/f^2	a_3/f^2	b_3/f^2	a_4/f^2	b_4/f^2
$f=0.5$	-0.083	-0.161	0.463	0.014	0.022	-0.032	0.026	0.006	0.001
$f=0.75$	-0.096	-1.793	0.803	0.019	0.124	-0.140	-0.154	-0.015	0.018
$f=1.0$	-0.051	-2.268	1.161	0.041	0.084	-0.213	-0.211	-0.009	0.023
$f=1.5$	-0.044	-2.673	1.318	0.015	0.168	-0.171	-0.284	-0.022	0.014
$f=2.0$	-0.040	-2.872	1.304	-0.043	0.174	-0.164	-0.271	-0.021	0.016

We further study the effect of frequency under $d/B=0.1$, $h_0/B=0.1, s_{wall}/B=0.4$. It is expected that the vertical force would increase with the frequency like that in

section 4.3.2. The force history is not plotted here. The decomposed coefficients of the force are divided by the square of the frequency. As shown in table 6.4, the value of a_1 / f^2 increases rapidly as the frequency; b_1 / f^2 increases at lower frequencies and remains the same level when $f = 1.5$ and $f = 2.0$. Compared with those of higher frequencies, the value of a_1 / f^2 and b_1 / f^2 at $f = 0.5$ are very small. The underlying reason could be the flow due to gravity and the free surface. When the compartment moves up and down slowly, the ingress and egress flow is driven by the hydrostatic force at lower frequencies. Therefore the damping force is dominated by the flow due to free surface and the gravity at low frequency; it is quadratic at higher frequencies. We notice that the terms a_i / f^2, b_i / f^2 $(i \geq 2)$ are very small when compared with the first order terms.

Chapter 7 Concluding remarks

7.1 Conclusions

The present study focuses on the simulation of vortex shedding from the sharp edge of marine structures. The potential flow theory and boundary element method are adopted to describe the inviscid flow around the marine structures.

For the linear vortex shedding problem, a flat dipole vortex sheet stretching from the trailing edge of the foil is used to impose the circulation. To study a foil advancing in waves, the linear free surface boundary conditions are satisfied through the free surface Green function. The wave radiation and diffraction of a foil have been investigated. The theory adopted is quite similar to the work of Grue et al (1988); however the thickness and the initial attack angle would result the second order derivative problem of m_j terms. An effective finite difference method has been proposed to calculate the value of these terms. The attack angle, forward speed, submergence and the oscillation frequency are analyzed. The free surface affects the steady and unsteady hydrodynamic force significantly. There is a sudden variation of the radiation and diffraction wave force near the critical frequency when $\tau = \frac{1}{4}$. The linear theory is applicable for a foil with smaller attack angle with small amplitude motions.

A numerical vortex shedding scheme has been developed to simulate the nonlinear continuous vortex shedding of a foil when the attack angle or oscillatory motion amplitude become large. An unsteady Kutta condition for numerical simulation is proposed and imposed on the vortex sheet element connecting with the trailing edge. The Kelvin theorem is used to determine the strength of the shed vortices. The shed

vortex sheet is replaced by point vortex to avoid bundle of vortex. The vortex sheet element connecting to the trailing edge is like the tail of the foil; and the vortex shedding scheme is an 'egg-laying' like procedure (see Fig. 4.18). The simulation goes well for an oscillatory foil with large amplitude motions. The results for propulsion have been verified by the experimental data by Triantafyllou et al (2005). The propulsion, energy harvesting and flying modes are investigated extensively. The effect of parameters such as St, h_0/C, α_0 and ε on the performance of an oscillatory foil are investigated. A reversed Karman vortex street has been observed as shown in figures 4.1 and 4.21. Although the friction resistance has been ignored, the developed numerical scheme is a fast tool to find out the performance of different combinations of vertical and rotational motions.

When the thickness of the foil approaches zero, the numerical scheme is applied to a plate with minor changes. Numerical results of a plate at small attack angle with/without small amplitude oscillation agree well with the analytical solution. The numerical scheme of vortex shedding is extended to large amplitude oscillatory motion. When compared with the results of a thin foil, discrepancy has been found. This would be due to the fact of the sharp edge of the plate. Theoretically, the flow near the leading edge of the plate shall be singular; however, the present numerical solution at the leading edge of large value affected by the element size. The numerical scheme is further applied to study the vortex shedding of a compartment consisting of two curved plates. The effect of heave amplitude, orifice size and frequency are studied. The damping effect is more significant with medium orifice size and smaller h_0/B, and it is proportional to the square of the frequency. The damping coefficient can be used to help the prediction of the motion of damaged ship in waves (Gaillard et

al 2011).

The transient nonlinear free surface effect and the coupled motion of shed vortices are studied through the time stepping method. The nonlinear free surface boundary conditions are imposed and the free surface is updated in the framework of Lagrangian. The steady motion of NACA0012 under a free surface with various Froude numbers is investigated. The nonlinear free surface effect and fluctuation of the force curves have been observed, which is mainly due to the free surface wave and fluctuating vortex sheet. For oscillatory foil under a free surface, the performance of the selected vertical and rotational motions for propulsion and energy harvesting modes are not affected significantly. Slight difference can be observed in the force time histories. The thrust force is slightly smaller when the foil is leaving its mean position upwards and slightly larger when it moves downwards. While for the selected oscillatory motion in flying mode, the wave effect becomes significant, the simulated case has a much higher propulsive efficiency when compared with the foil in the unbounded flow.

The vortex shedding of a floating damaged compartment has been modeled by structure with an orifice. The edge of the orifice is modified to fit the time stepping scheme. Compared with the results of pure potential flow, the damping effect due to vortex shedding is significant when the force is decomposed into components of sinusoidal functions. The effects of orifice size, heave amplitude and the frequency are investigated. Larger damping coefficient is found with medium orifice size, which is consistent with the results in the unbounded flow. However, the damping effect increases with the heave amplitude h_0 / B, which is different from that in the unbounded flow. The frequency affects the vortex shedding significantly; the

coefficients of first order components divided by the square of the frequency, which refer to added mass and damping force, increase at higher frequencies. However, the value of these first order components at lower frequency decreases significantly; the fluid flow would be dominated by the gravity.

One of the aims of present study is to develop a fast tool to simulate the inviscid flow around structure with sharp edge. The simulations are run on a laptop with an Intel i5 CPU of 2.3G Hz. The accuracy of the results of present method is acceptable, verifications have been shown in chapter 3, 4 and 6. For linear theory in chapter 3, the hydrodynamics force of a foil at specific conditions (with submergence, Froude number, with or without motion frequency) can be obtained in a few seconds. While for the nonlinear vortex shedding of a foil in unbounded flow, the time stepping scheme would take a few minutes to obtain the hydrodynamic force of 5 oscillatory cycles. When the free surface is concerned, the computation would take a few hours since approximately 2000 meshes on the free surface are used. To my own knowledge, the computation using commercial software (eg. Anysys CFX) would take several days or several weeks. Generally, the objective of the study has been satisfied.

7.2 limitations and suggestions for further development

In general, the developed numerical vortex shedding scheme together with the unsteady Kutta condition is successful. The numerical simulations of the vortex shedding of a foil and the damaged compartment with orifice are carried out continuously. However, the present numerical scheme has its limitation and shortfalls. (a) The proposed Kutta condition is suitable for sharp edges like the trailing edge of a foil. However, the application to a large angle structure could be inaccurate since the method approximates tangential flow leaving a sharp edge. Vortex shedding at the

leading edge or from a smooth surface is beyond the proposed scheme. (b) Long time simulation on the damaged compartment model would be difficult when the free surface is presented. When the vortices nearly contact or penetrate the free surface, the simulation would break down. The shed vortex might also cause instability when updating the free surface. (c) The point vortices do not damp automatically; the introduced artificial damping function is chosen more or less arbitrarily, justification of the damping for non-symmetric vortex shedding would be a problem.

For future development, there are several topics that need intensive investigations: (1) The nonlinear wave diffraction of a foil; (2) the self-propulsion of a foil and (3) the wave effect on the three dimensional foil; (4) the coupled motion of the damaged ship structure and waves; (5) the vortex shedding of a flexible foil (Xiao et al 2012). The present work can be extended to practical engineering problems such as biomimetic study of three dimensional flying bird (Ellington et al 1996) or swimming fish and (6) three dimensional vortex shedding at the orifice of a damaged ship. Some of these problems will be very challenging.

References

Abramowitz M., Stegun I.A. 1965 Handbook of Mathematical Functions. Dover.

Alben S. 2009 Simulating the dynamics of flexible bodies and vortex sheets. Journal of Computational Physics 228, 2587-2603.

Anderson J.M., Streitlien K., Barrett D.S., Triantafyllou M.S. 1998 Oscillating foils of high propulsive efficiency. Journal of Fluid Mechanics 360, 41-72.

Ashraf M.A., Young J., Lai J.C.S. 2011 Reynolds number, thickness and camber effects on flapping airfoil propulsion. Journal of Fluids and Structures 27, 145-160.

Ausman J.S. 1954 Pressure limitation on the upper surface of a hydrofoil. Ph.D. thesis, Mechanical Engineering, University of California, Berkeley, California.

Batchelor G.K. 1967 An Introduction to Fluid Dynamics, Cambridge press.

Bal S. 1999 A potential based panel method for 2-D hydrofoils. Ocean Engineering 26, 343-361.

Bristow D.R. 1980 Development of panel methods for subsonic analysis and design. NASA. CR-3234.

Clements R.R. 1973 An inviscid model of two-dimensional vortex shedding. Journal of Fluid Mechanics 57,321-336.

Cortelezzi L., Chen Y.C., Chang H.L. 1997 Nonlinear feedback control of the wake past a plate: From a low-order model to a high-order model. Physics of Fluids 9, 2009-2021.

Dickinson M.H., Lehmann F.O., Sane S.P. 1999 Wing rotation and the aerodynamic basis insect flight. Science 284, 1954-1960.

Donwin, M.J., Bearman P.W., Graham J.M.R. 1988 Effect of vortex shedding on the coupled roll response of bodies in waves. Journal of Fluid Mechanics 189, 243-264.

Ellington, C.P. 1984 The aerodynamics of hovering insect flight. IV. Aerodynamic mechanisms. Philosophy Transaction of Royal Society London B 305, 79-113.

Ellington C.P., Vanderberg C., Wilmott A., Thomas A. 1996, Leading edge vortices in insect flight. Nature 384, 626-630.

Faltinsen O.M., Semenov Y. 2008 The effect of gravity and cavitation on a hydrofoil near the free surface. Journal of Fluid Mechanics 597, 371–394.

Gaillard A.C., Xu G.D., Wu G.X. 2011 Simulations of motions of a damaged ship with vortex shedding damping at orifice. Proceedings of the Seventh International Workshop on Ship Hydrodynamics, September 16-19, Shanghai, China.

Giesing J.P., Smith A.M.O. 1967 Potential flow about two-dimensional hydrofoils. Journal of Fluid Mechanics 28, 113-129.

Graham J.M.R. 1980 The forces on sharp-edged cylinders in oscillatory flow at low Keulegan-Carpenter numbers. Journal of Fluid Mechanics 97, 331-346.

Grue J., Palm E. 1985 Wave radiation and wave diffraction from a submerged body in a uniform current. Journal of Fluid Mechanics 151, 257-278.

Grue J., Mo A., Palm E. 1988 Propulsion of a foil moving in water waves. Journal of Fluid Mechanics 186, 393-417.

Hess J.L., Smith A.M.O. 1964 Calculation of non-lifting potential flow about arbitrary three-dimensional bodies. Journal of Ship Research 8, 22-44.

Hu P.X., Wu G.X., Ma Q.W. 2002 Numerical simulation of nonlinear wave radiation by a moving vertical cylinder. Ocean Engineering 29, 1733–1750.

Jones M.A. 2003 The separated flow of an inviscid fluid around a moving flat plate. Journal of Fluid Mechanics 496, 405-441.

Jones M.A., Shelley M.J. 2005 Falling cards. Journal of Fluid Mechanics 540, 393-425.

Katz, J. 1981 A discrete vortex method for the non-steady separated flow over an airfoil. Journal of Fluid Mechanics 102, 315-328.

Katz J., Plotkin A. 1991 Low speed aerodynamics, From Wing Theory to Panel Methods. McGraw-Hill, Inc.

Keulegan, G.H., Carpenter L.H. 1958 Forces on cylinders and plates in an oscillating fluid. Journal of Research of the National Bureau of Standards 60, 423–440.

Kristiansen T., Faltinsen O.M. 2008 Application of a vortex tracking method to the piston-like behaviour in a semi-entrained vertical gap. Applied Ocean Research 30, 1-16.

Kristiansen T., Faltinsen O.M. 2010 A two-dimensional numerical and experimental study of resonant coupled ship and piston-mode motion. Applied Ocean Research 32 158-176.

Kuwahara K. 1973 Numerical study of flow past an inclined flat plate by an inviscid model. Journal of Physics Society of Japan 35, 1545-1551.

Lai J.C.S., Yue J., Platzer M.F. 2002 Control of backward-facing step flow using a flapping foil. Experiments in Fluids 32, 44-54.

Lamb H. 1932 Hydrodynamics, New York: Dover.

Landrini, M., Lugni, C., Bertram, V. 1999 Numerical simulation of the unsteady flow past a hydrofoil. Ship Technology Research 46, 14-30.

Liao Z.P., Wong H.L., Yang B.P., Yuan Y.F. 1984 A transmitting boundary for transient wave analysis. Scientia Sinica A 27, 1063-1076.

Lighthill M.J. 1960 Note on the swimming of slender fish. Journal of Fluid Mechanics 9, 305-317.

Lighthill M.J. 1970a Note on the swimming of slender fish. Journal of Fluid Mechanics 44, 265-301.

Lighthill M.J. 1970b Aquatic animal propulsion of high hydrodynamic efficiency, Journal of Fluid Mechanics 44, 265-301.

Lighthill M.J. 1971 Large-amplitude elongated-body theory of fish locomotion. Proceeding of Royal Society of London B 179, 125-138.

Lighthill, J. 1975 Mathematical Bio-fluid dynamics, SIAM, Philadelphia.

Longuet-Higgins, M.S., Cokelet. E.D. 1976 The deformation of steep surface waves on water: A numerical method of computation. Proceedings of Royal Society London A 350, 1-26.

Mantia M.L., Dabnichki P. 2011 Influence of the wake model on the thrust of oscillating

foil. Engineering Analysis with Boundary Elements 35, 404-414.

Maresca C., Favier D., Rebont J. 1979 Experiments on an airfoil at high angle of incidence in longitudinal oscillations. Journal of Fluid Mechanics 92, 671-690.

Maruo, H., Song, W. 1994 Nonlinear analysis of bow wave breaking and deck wetness of a high speed ship by the parabolic approximation. Proceeding of 20th symposium on naval hydrodynamics, University of California, Santa Barbara, California.

Maskell E.C. 1972 On the Kutta-Joukowski condition in two-dimensional unsteady flow. Technical Memo Aero-1451, Royal Aircraft Establishment, Farnborough, UK.

Newman J.N. 1977 Marine hydrodynamics. MIT press.

Newman J.N. 1978 The theory of ship motions. Advance in Applied Mechanics 18, 221-283.

Nitsche M., Krasny R. 1994 A numerical study of vortex ring formation at the edge of a circular tube. Journal of Fluid Mechanics 97, 239-255.

Pan Y.L., Dong X.X, Zhu Q., Yue D.K.P. 2012 Boundary-element method for the prediction of performance of flapping foils with leading-edge separation. Journal of Fluid Mechanics 698, 446-467.

Pullin D.I., Perry A.E. 1980 Some flow visualization experiments on the starting vortex. Journal of Fluid Mechanics 97, 239-255.

Read D.A., Hover F.S., Triantafyllou M.S. 2003 Forces on oscillating foils for propulsion and maneuvering. Journal of Fluids and Structures 17, 163-183.

Sarpkaya, T. 1975 An inviscid model of two-dimensional vortex shedding for transient and asymptotically steady separated flow over an inclined plate. Journal of Fluid Mechanics 68, 109-128.

Sarpkaya, T. 1989 Computational methods with vortices - The 1988 Freeman Scholar lecture. Trans. ASME: Journal of Fluids Engineering-Transaction of ASME 111, 5-52.

Sheldahl R.E., Klimas P.C. 1981 Aerodynamic characteristics of seven airfoil sections through 180 Degrees angle of attack for use in aerodynamic analysis of vertical axis wind turbines, SAND80-2114, March, Sandia national laboratories, Albuquerque, New Mexico.

Smith A.M.O., Pierce J. 1958 Exact solution of the Neumann problem. Calculation of non-circulatory plane and axially symmetric flow about or within arbitrary boundaries. Douglas Aircraft Company Rept. ES 26988.

Smith T.W.P. 2009 Wave loading on damaged ships, Ph.D. thesis, University College London.

Sommerfeld A. 1949 Partial Differential Equations in Physics, Academic Press, New York.

Tanizawa, K., Swada, H. 1996 A numerical method for nonlinear simulation of 2-D body motion in waves by means of BEM. Journal of the Society of Naval Architecture of Japan 166, 311-319.

Timman R., Newman J.N. 1962 The coupled damping coefficients of a symmetric ship. Journal of Ship Research 5, 1-7.

Triantafyllou M.S., Triantafyllou G.S., Yue D.K.P. 2000 Hydrodynamics of fishlike swimming. Annual Review of Fluid Mechanics 32, 33-53.

Triantafyllou M.S., Hover F.S., Techet A.H., Yue D.K.P. 2005 Review of hydrodynamic scaling laws in aquatic locomotion and fishlike swimming. Journal of American Society of Mechanical Engineers 58, 226-237.

Wang C.Z., Wu G.X. 2006 An unstructured-mesh-based finite element simulation of wave interactions with non-wall-sided bodies. Journal of Fluids and Structures 22, 441-461.

Wehausen J.V., Laitone E.V., 1960 Surface Waves, Handbuch der Physik 9, 446-778, Springer.

Wu G.X. 1986 Hydrodynamic forces on oscillating submerged bodies at forward speed. Ph.D. thesis, Faculty of Engineering, University College London.

Wu G.X., Eatock Taylor R. 1987 Hydrodynamic forces on submerged oscillating cylinders at forward speed. Proceedings of the Royal Society of London Series A; 414, 149-170.

Wu G.X., Eatock Taylor R. 1988 Reciprocity relations for hydrodynamic coefficients of bodies with forward speed. International Shipbuilding Progress 35, 145-153.

Wu G.X., Eatock Taylor R. 1990 The hydrodynamic force on an oscillating ship with low forward speed. Journal of Fluid Mechanics 211, 333-353.

Wu G.X. 1991a A numerical scheme for calculating the m_j terms in wave-current-body interaction problem. Applied Ocean Research 13, 317-319.

Wu G.X. 1991b Hydrodynamic force on a submerge cylinder advancing in water waves

of finite depth. Journal of Fluid Mechanics 224, 645-659.

Wu G.X. 1993 A relationship between wave reflection and transmission by a submerged body at forward speed. Applied Ocean Research 15, 311-313.

Wu G.X. 1994a Wave radiation by an oscillating surface-piercing plate at forward speed. International Shipbuilding Progress 41, 179-190.

Wu G.X. 1994b A note on non-linear hydrodynamic forces on a body submerged below a free surface. Applied Ocean Research 15, 371-372.

Wu G.X. 2000 A note on non-linear hydrodynamic force on a floating body, Applied Ocean Research 22, 315-316.

Wu T.Y. 1961 Swimming of a waving plate. Journal of Fluid Mechanics 10, 321-344.

Wu T.Y. 1971a Hydrodynamics of swimming propulsion, Part1: Swimming of a two-dimensional flexible plate at various forward speeds in an inviscid fluid. Journal of Fluid Mechanics 46, 337-355.

Wu T.Y. 1971b Hydrodynamics of swimming propulsion, Part2: Some optimum shape problems. Journal of Fluid Mechanics 46, 521-544.

Wu T.Y. 1972 Extraction of flow energy by a wing oscillating in waves. Journal of Ship Research 16, 66-78.

Xiao Q., Liao W., Yang S.C., Peng Y. 2012 How motion trajectory affects energy extraction performance of a biomimic energy generator with an oscillating foil? Renewable Energy 37, 61-75.

Xie N., Vassalos D. 2007 Performance analysis of 3D hydrofoil under free surface. Ocean Engineering 34, 1257-1264.

Xu G.D., Duan W.Y., Wu G. X. 2010 Simulation of water entry of a wedge through free fall in three degrees of freedom. Proceeding of Royal Society A 466, 2219-2239.

Yeung R.W., Bouger Y.C. 1979 A hybrid-integral equation method for steady two-dimensional ship waves. International Journal of Numerical Method of Engineering 14, 317-336.

Zhao, R., Faltinsen, O.M. 1989 A discussion on the mj terms in the wave-current body interaction problem, 4th Workshop on water waves and floating bodies, Norway.

Zhu Q, Liu Y, Yue D.K.P. 2006 Dynamics of a three-dimensional oscillating foil near the free surface AIAA Journal 44, 2997-3009.